International Journal of Heat and Mass Transfer 205 (2023) 123854

Contents lists available at ScienceDirect

International Journal of Heat and Mass Transfer

journal homepage: www.elsevier.com/locate/hmt

An improved cavitation model with thermodynamic effect and multiple cavitation regimes ☆

Wenguang Li, Zhibin Yu*, Sambhaji Kadam

School of Engineering, University of Glasgow, Glasgow G12 8QQ, UK

ARTICLE INFO

Article history:
Received 22 September 2022
Revised 23 December 2022
Accepted 7 January 2023

Keywords:
Cavitation model
Thermodynamic effect
Cavitation regime
Organic fluid
Temperature depression
Rayleigh-Plesset equation

ABSTRACT

Mechanical feed pumps in organic Rankine cycle (ORC) power plants can suffer from cavitation to lose their normal feeding performance or even damage. Cavitation models for organic fluids in ORC systems are lacking presently. Hence, a new cavitation model with thermodynamic effect was proposed. Surface tension-controlled, inertia-controlled, intermediate and heat transfer-controlled cavitation regimes, and two key elements: vapour bubble growth rate and vapour bubble number density are included in the model. A known air or non-condensable gas concentration in the liquid was employed to determine cavitation nuclei number density. The model was coded in ANSYS CFX as user defined model and validated with cavitating flows of organic fluid R114 in a venturi, liquid nitrogen and liquid hydrogen on a tapered hydrofoil and warm water around a hydrofoil NACA 0015 in cavitation tunnels based on visualised cavity length. Two model constants, temperature depression, and minimal cavitation number were correlated to bulk liquid temperature, Reynolds number, and Jakob number. The temperature and pressure profiles of liquid nitrogen and hydrogen on hydrofoil surface were examined against the experimental data. The model was applied to simulate unsteady cavitating flows of organic fluid R245fa in a diaphragm pump. It was shown that the temperature depression and minimal cavitation number cannot be correlated to bulk liquid temperature, Reynolds number and Jakob number. Two model constants can be correlated fairly to Reynolds number. The model underestimates the thermodynamic effect by 43% for R114, 18.6% for liquid nitrogen and 32.6% for liquid hydrogen based on temperature depression. The predicted temperature and pressure profiles on hydrofoil surface agree with the experimental data for liquid nitrogen. The model can produce an expected curve of mean pump flow rate against net positive suction head available.

1. Introduction

In the quest of finding ways to maximise the utilisation of low-grade energy and minimise or nullify detrimental deterioration of the environment from the system, the organic Rankine cycle (ORC) is a topic of intensive research. An ORC has intense potential to produce electric power by using organic working fluid in conjunction with low-temperature heat sources such as biomass combustion, industrial waste heat, or geothermal heat [1,2]. The feed pump, delivering liquid medium to the evaporator, is one of the crucial equipment of ORC system amongst others (evaporator, condenser, turbine). The mechanical feed pumps [3,4] and thermofluidic feed pump [5,6] can be employed in an ORC system, however, the mechanical feed pump is more popular because of its simple structure and easy operation. The mechanical feed pump is further classified as rotodynamic pump and positive displacement pump. The rotodynamic pumps (multistage centrifugal pump [7,8], single-stage centrifugal pump [9], roto-jet pump [7], regenerative pump [10]) and the positive displacement pumps (axial piston pump [11,18], sliding vane pump [12,13], plunger pump [9], piston pump [14,15], diaphragm pump [7,16–18], and external gear pump [17]) have been tested in ORC systems by using the organic fluids R11, R113, R123, R134a, R404, R245fa, HEF-7100, and inorganic mixture NH_3/H_2O, respectively. However, all these different types of pumps can be victim of damaging phenomena of cavitation.

Cavitation can occur in a mechanical feed pump if the net positive suction head available (NPSHa) or subcooling is insufficient. Cavitation can lead to pump performance degradation, noise, vibration and even mechanical damage. NPSHa is the total energy of fluid at the pump inlet minus the saturated vapour pressure at the pump operating temperature. Subcooling ΔT_{sub} is defined as the difference of the saturated vapour temperature at a far field pressure from the far field temperature. To avoid cavitation in a me-

☆ Date: 10 January 2023

* Corresponding author.
E-mail address: Zhibin.yu@glasgow.ac.uk (Z. Yu).

https://doi.org/10.1016/j.ijheatmasstransfer.2023.123854

Nomenclature

A	constant associated with NPSHa and defined in Eq. (13)
B	constant associated with ΔT_{sub} and defined in Eq. (15)
c_{pl}	specific heat capacity of liquid, J/(kg K)
c_{pv}	specific heat capacity of vapour, J/(kg K)
C_p	pressure coefficient defined in Eq. (23)
d_h	diameter of the seat in Fig. 19, mm
d_{v1}	the smallest diameter of the valve in Fig. 19, mm
d_{v2}	the largest diameter of the valve in Fig. 19, mm
D	diameter of the approach section of a venturi, mm
D_{ref}	characteristic or reference length of a fluid flow system, m
$\mathscr{D}$	thermal diffusivity of liquid ($=\lambda_l/\rho_l c_{pl}$), m^2/s
h	valve opening in Fig. 19, mm
h_0	pre-compressed displacement of the spring in Fig. 19, mm
h_{max}	valve maximum opening in Fig. 19, mm
$\mathscr{h}$	enthalpy of mixture, J/kg
f	force acting on the valve, N
F_{vap}	empirical constant for evaporation in Eq. (1)
F_{con}	empirical constant for condensation in Eq. (1)
J	Jakob number defined in Eq. (15)
k	turbulent kinetic energy, m^2/s^2
K	conventional cavitation number defined in Eq. (21)
K_{min}	minimal cavitation number defined in Eq. (24)
L	chord of the hydrofoil, mm
L_{cav}	cavity length, mm
$\mathscr{L}$	latent heat of liquid, J/kg
n	rotating speed of the crank in Fig. 18, rpm
N	vapour bubble number density, $1/m^3$
N_{air}	air bubble number density, $1/m^3$
m_{con}	mass transfer rate per unit volume for vapour condensation, kg/(s m^3)
m_f	mass flow rate in Eq. (22), kg/s
m_{vap}	mass transfer rate per unit volume for vapour growth, kg/(s m^3)
M_v	mass of the valve body, kg
p	liquid/mixture static pressure, Pa
p_1	liquid pressure at pump inlet, kPa
p_g	partial pressure of air/non-condensable gas in a bubble, Pa
p_{min}	minimal pressure, Pa
p_{real}	fluid real pressure expressed as Eq. (26), Pa
p_{turb}	pressure fluctuation due to turbulence, Pa
p_v	vapour pressure, Pa
p_w	fluid pressure on the venturi wall, Pa
p_∞	liquid pressure in far field, kPa
P_k	production rate of turbulence, W
Pr_t	turbulent Prandtl number, Pr_t=0.9
q	instant pump flow rate, L/min
Q	mean pump flow rate, L/min
Q_N	mean pump flow rate without cavitation, L/min
r	radial coordinate of the spherical coordinate system, m
R	vapour bubble radius, m
R_1	radius of flat cap of the diaphragm in Fig. 18, mm
R_2	radius of the diaphragm in Fig. 18, mm
Re	Reynolds number
R_∞	vapour bubble radius at p_∞ and T_∞, m
s	stroke of the diaphragm listed in Table 8, mm
t	time, s
t_{ref}	reference or characteristic time of a fluid flow system, s
T	liquid/mixture temperature, K
T_v	vapour temperature, K
T_{sat}	saturated vapour temperature at p_∞, K
T_∞	temperature of liquid in far field, K
u	mixture velocity vector, m/s
u_{ref}	characteristic or reference velocity of a fluid flow system, m/s
u_∞	liquid/mixture velocity in far field, m/s
U	interface heat transfer coefficient of vapour bubble, W/(m^2 K)
V	velocity of the diaphragm in Fig. 18 or velocity of the valve in Fig. 19, m/s
w	width of the fluid domain in Fig. 7, w=12.7 mm
x	displacement of the diaphragm Fig. 18, m

Greek

α	vapour volume fraction
α_{max}	maximal vapour volume fraction
β_1, β_2, β_3	constants of the Wilcox k-ω turbulence model in Eqs. (A5) and (A6), β_1=0.09, β_2=5/9 and β_3=0.075
γ	liquid surface tension, N/m
δ	thickness of the fluid domain in Fig. 7, δ=0.1 mm
Δp	pressure depression due to thermodynamic effect in cavitation, see Fig. 1, Pa
ΔT	temperature depression due to thermodynamic effect in cavitation, see Fig. 1, K
ΔT_{max}	maximal temperature depression, K
ΔT_{sub}	subcooling, see Fig. 1, K
$\Delta\phi$	central angle of the fluid domain in Fig. 2, $\Delta\phi$=5°
θ	cone angle of the valve in Fig. 19, °
κ	stiffness of the spring, N/m
λ	mixture thermal conductivity, W/(m K)
λ_l	liquid thermal conductivity, W/(m K)
λ_v	vapour thermal conductivity, W/(m K)
μ	mixture dynamic viscosity, Pa s
μ_l	liquid dynamic viscosity, Pa s
μ_t	turbulent eddy viscosity, Pa s
μ_v	vapour dynamic viscosity, Pa s
ρ	mixture density, kg/m^3
ρ_{air}	air density at T_∞ and $p_v(T_\infty)$, kg/m^3
ρ_l	liquid density, kg/m^3
ρ_v	vapour liquid, kg/m^3
σ_1, σ_2	constants of the Wilcox k-ω turbulence model in Eqs. (A5) and (A6), σ_1=σ_2=2
τ	mixture shear stress tensor, Pa
φ	rotating angle of the crank in Fig. 18, °
ω	rate of dissipation per unit turbulent kinetic energy, 1/s
Ω	rotating angular speed of the crank in Fig. 18, rad/s

Abbreviation

1D	one-dimensional
2D	two-dimensional
3D	three-dimensional
AOA	angle of attack
CEL	CFX Expression Language
CFD	computational fluid dynamics
LH2	liquid hydrogen
LN2	liquid nitrogen
NPSHa	net positive suction head available

NPSHr	net positive suction head required
ORC	organic Rankine cycle
ppm	parts per million
PS	pressure side
SS	suction side
ZGB	Zwart-Gerber-Belamri

chanical pump, NPSHa or subcooling must be higher than the net positive suction head required (NPSHr) or the subcooling required with a safety margin.

To prevent an occurrence of cavitation of organic fluid in a mechanical feed pump used in ORC systems, NPSHr or subcooling of the pump needs to predict accurately by thermodynamic effect. Currently, studies on cavitation in mechanical feed pumps handling organic fluids are rare. Bollina [11] established the mean flow rate versus NPSHa curves for a variable-stroke axial piston swash-plate pump operated with organic fluids R11 and R113 at rotating speeds of (1750–3000) rpm and temperatures of (20–80) °C. Bala et al. [12] investigated the hydraulic performance of a positive displacement pump having sliding vanes with R11 and R113 and their blended mixtures at different rotating speeds and pressures, and observed that the quantity of vapour in the pump with R11 was greater than R113. Because the cavitation performance of the pump for water was not tested, the difference in cavitation performance between the organic fluids and water could not be figured out.

Positive displacement pumps could experience a NPSHr of 24 kPa [16] or severer subcooling (4.4–20) °C [14,16]. Li et al. [19] studied the cavitation performance of the diaphragm pump (Wanner^{TM} G20-E model) analytically when the pump delivering organic fluid R245fa. A NPSHr correction method for thermodynamic effect in cavitation was proposed and the one-dimensional (1D) motion of the suction valve of the pump was simulated numerically by using two mechanical models to predict the NPSHr at 100 kPa and 141 kPa pump inlet pressures along with preliminary experiments. The NPSHa at those inlet pressures was calculated and the cavitation safety margin was addressed, the subcooling for the NPSHr, NPSHa and safety margin were then decided. Casari et al. [20] studied the transient behaviour of the pumping system of a regenerative micro-ORC system including the liquid receiver, entire flow path, and inlet section of the evaporator was analysed by using computational fluid dynamics (CFD) approach and shown that the accuracy of mass flow rate measurement could be affected by the feed pump operation and the cavitation phenomenon could influence the operation of pump and ORC system. Recently, Li and Yu [21] simulated three-dimensional (3D), unsteady cavitating flows of organic fluid R245fa in a diaphragm pump with ANSYS 2019R2 CFX in suction stroke based on the k-ω turbulence model, the Zwart-Gerber-Belamri (ZGB) cavitation model, rigid body motion model for 1D motion of valve and moving mesh technique. The thermodynamic effect in cavitation was considered in the cavitation model. However, the cavitation model crashed when the pump inlet pressure was lower than 85.2 kPa and failed to capture the important characteristic that the mean pump flow rate declined with decreasing NPSHa observed in [11]. This clearly indicates the need of generalised cavitation model which rigorously incorporates the thermodynamic effect and adapts a wide range of operating conditions.

In this context, this article presents a new cavitation model with thermodynamic effect based on the Schnerr-Sauer model [22] and analytical vapour bubble growth rate under superheat conditions [23]. The model takes surface tension-controlled, inertia-controlled, intermediate and heat transfer-controlled cavitation regimes into account. The model is implemented in ANSYS CFX as user defined model by using CFX Expression Language (CEL). The feasibility of the model has been validated by employing cavitating flows of R114 in a venturi [24], LN2 and LH2 over the tapered hydrofoil [25] and warm water around the hydrofoil NACA 0015 [26] in cavitation tunnels. The validated model is applied to simulate unsteady cavitating flows of organic fluid R245fa in the diaphragm pump [21].

The proposed cavitation model can predict the declination of mean pump flow rate with decreasing NPSHa, thus the NPSHr of the pump can be determined. The model can serve as a framework for cavitation modelling with thermodynamic effect and help a design engineer to identify the operating range under available operating circumstances to avoid the existence of cavitation. This will help in mitigating or early detection of an occurrence of cavitation and reducing corresponding harmful effects such as performance degradation, noise and vibration and even mechanical damage under certain circumstances. Hence, the operational flexibility of the feed pump used in ORC can be improved without sacrificing the performance of the whole ORC system.

2. Thermodynamic effect and cavitation model

2.1. Thermodynamic effect of organic fluids

Cavitation is a phenomenon whereby a proportion of liquid undergoes vapour phase when the absolute pressure of a local fluid flow field falls below the saturated vapour pressure corresponding to the local temperature. This kind of cavitation is driven by the reduction in static pressure in a fluid flow field, as shown the process 1→3 in Fig. 1. Since cavitation is a phase change of liquid to vapour, latent heat is needed, and there is heat transfer to the cavity from its surrounding liquid, exhibiting a thermodynamic effect where temperature depression and saturated vapour pressure depression emerge against the far field temperature T_∞ and pressure p_∞, as indicated by the process 1→4 in Fig. 1. For a given temperature depression ΔT, the larger the saturated vapour pressure depression Δp, the stronger the thermodynamic effect, and the more significantly the cavitation is suppressed.

The magnitude of saturated vapour pressure depression depends on the slope of the saturation line of liquid, i.e., dp/dT. The steeper the slope, the stronger the thermodynamic effect. The dp/dT curves of water, liquid hydrogen (LH2), liquid nitrogen (LN2), organic fluids R114, R123, R134a, R1234yf, and R245fa are illustrated in Fig. 1. According to dp/dT values, LH2 experiences the strongest thermodynamic effect in cavitation, then LN2 follows, while water possesses the weakest thermodynamic effect, and the other five organic fluids are in-between LN2 and water in thermodynamic effect. In hydrodynamics, cavitation develops along path 1→3 and does not exhibit the thermodynamic effect at all. The cavitation along path 1→2 is driven by superheat, essentially this cavitation is evaporation or boiling.

2.2. New cavitation model

CFD software ANSYS CFX was employed to solve cavitating flow of organic fluids with thermodynamic effect. The cavitating flow, which is considered as an incompressible homogeneous multiphase flow of a mixture of continuous liquid and its continuous vapour is described in the Eulerian-Eulerian coordinate system. In the homogeneous multiphase flow, all fluids have the same velocity, pressure, temperature and turbulence. The governing equations of the homogeneous multiphase flow including the Wilcox k-ω turbulence model are adapted from [27] and listed in Appendix A.

The cavitation process is modelled with source term m_{vap} for vaporisation and m_{con} for condensation in the continuity equations of vapour and liquid expressed by Eqs. (A1) and (A2), respectively. The source terms m_{vap} and m_{con} are expressed analyt-

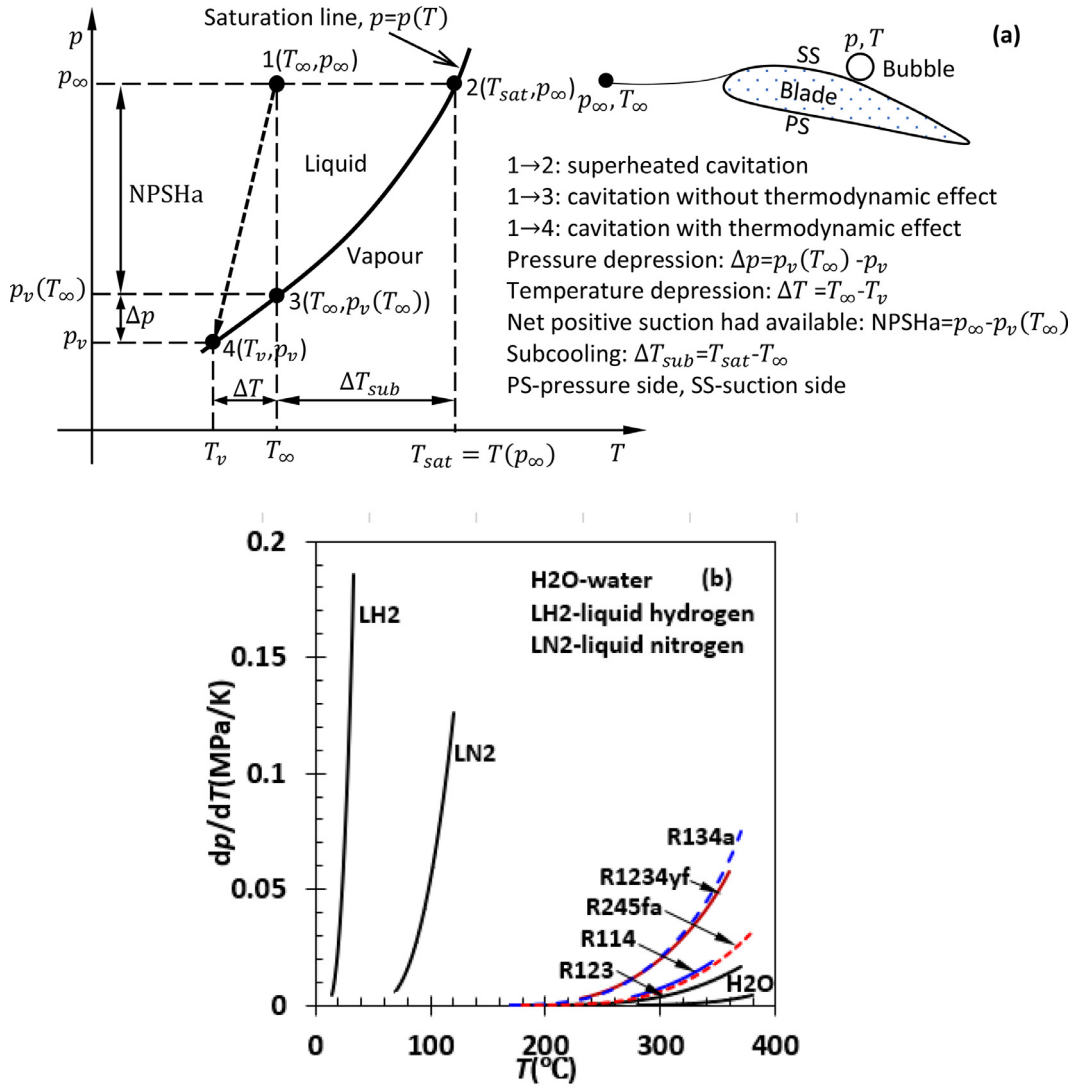

Fig. 1. Three processes of cavitation of a liquid flowing around a blade, and definition of pressure depression, temperature depression, NPSHa and subcooling(a), and the slopes of saturation line of water(H2O), liquid hydrogen(LH2), liquid nitrogen(LN2), organic fluids R114, R123, R1234yf, R134a and R245fa plotted as a function of liquid temperature, dp/dT (b).

ically by Eq. (A19). Introducing two empirical constants, F_{vap} and F_{con}, into Eq. (A19) to compromise the assumptions made to determine vapour bubble number density N, vapour volumetric fraction α and bubble growth or collapse rate dR/dt, the source terms m_{vap} and m_{con} are in the final forms:

$$\begin{cases} m_{vap} = F_{vap}(4\pi N)^{1/3}(3\alpha)^{2/3}(1-\alpha)^{4/3}\frac{\rho_l\rho_v}{\rho}\frac{dR}{dt} \\ m_{con} = -F_{con}(4\pi N)^{1/3}(3\alpha)^{2/3}(1-\alpha)^{4/3}\frac{\rho_l\rho_v}{\rho}\frac{dR}{dt} \end{cases} \quad (1)$$

where the positive constants F_{vap} and F_{con} need to be determined by using experimental data of cavitation available, such as cavity length, pressure profile etc. Constants F_{vap} and F_{con} depend on the thermophysical property of fluid, and cavitation number, Reynolds number, vapour bubble number density and bubble growth or collapse rate in flowing systems.

In this paper, we try to propose one Rayleigh-Plesset equation-based cavitation model to determine the source terms m_{vap} and m_{con} in Eq. (1). The vapour bubble number density N and vapour bubble growth or collapse rate dR/dt are the key parameters in the model.

2.2.1. Vapour bubble number density

The vapour bubble number density N must be modelled analytically. Gas pockets trapped in pits and crevices on a solid wall and stabilised free gas/air bubbles dissolved in a liquid ($\leq$1 μm in mean diameter) can serve as nuclei to initiate cavitation inception as the static pressure is below a critical value, i.e., the saturated vapour pressure of the liquid [28]. Usually, the vapour bubble number density of the gas pockets trapped in the wall is hardly estimated, but the vapour bubble number density of free air bubbles in the liquid could be predicted based on an estimated bubble radius and a known air concentration expressed by parts per million (ppm) or mg/L, which is the mass of a chemical or contaminate per unit volume of liquid.

The air bubbles are spherical in the far field of a liquid (see Fig. 1) and experience equilibrium state with its surrounding liquid. The bubble number density distribution function in water yields a power law against bubble radius, i.e., the function value decreases rapidly from a smaller radius to a larger radius. The peak bubble number density distribution function value occurs at 2.5 μm in water tunnels [29,30] at 1atm pressure, and (2.5–5) μm in water chamber with bubbles generated by a micro-nano bubble generator at (5–100) kPa [31]. The nuclei size and number density

will be determined based on the Rayleigh-Plesset equation and gas state equation. The full Rayleigh-Plesset equation, which governs the dynamics of a spherical vapour bubble in an infinite body of incompressible fluid, is written as [32]:

$$R\frac{d^2R}{dt^2}+\frac{3}{2}\left(\frac{dR}{dt}\right)^2=\frac{p_v(T)+p_g-p}{\rho_l}-\frac{4\nu}{R}\frac{dR}{dt}-\frac{2\gamma}{\rho_l R} \tag{2}$$

where p_g is pressure of non-condensable gas/air, ν is kinematic viscosity of liquid, γ is surface tension of liquid. The nuclei are compressed but in equilibrium between surface tension and pressure difference across the bubble surface in the far filed, thus $\frac{d^2R}{dt^2}=\frac{dR}{dt}=0$. Ignoring the pressure of non-condensable gas/air, Eq. (2) is simplified in the far field as:

$$\frac{p_\infty-p_v(T_\infty)}{\rho_l}-\frac{2\gamma}{\rho_l R_\infty}=0 \tag{3}$$

Obviously, the nuclei radius in the far field is calculated by:

$$R_\infty=\frac{2\gamma}{p_\infty-p_v(T_\infty)} \tag{4}$$

The air mass concentration in the liquid expressed by the air bubble number density N_{air} and volume of individual bubble should be equal to the concentration measured in terms of ppm. This means that the following equation is held:

$$N_{air}\frac{4}{3}\pi R_\infty^3\rho_{air}=\text{ppm}\times 10^{-3},\ \rho_{air}=\frac{p_v(T_\infty)}{287T_\infty} \tag{5}$$

where ρ_{air} is the air density at T_∞ and $p_v(T_\infty)$.

Since the air bubbles serve as cavitation nuclei of the liquid, the vapour bubble number density N should be identical to N_{air}, and is calculated by the following expression based on Eq. (5):

$$N=N_{air}=\frac{\text{ppm}\times 10^{-3}}{\frac{4}{3}\pi R_\infty^3\rho_{air}} \tag{6}$$

The air concentration is 22 ppm in water at 25 °C and 1atm pressure, giving a nuclei number density of 2.744×10^{14} m^{-3} and a volume fraction of 0.018 when ρ_{air}=1.225 kg/m^3, and R_∞=2.5 μm. The air-saturated R114 liquid has around 140 ppm air concentration at 0 °C, and about 1000 ppm at −32 °C [24]. In the present cavitation model, air concentration is assumed 140 ppm for organic fluids, and results in a nuclei number density of 1.746×10^{15} m^{-3} and a volume fraction of 0.103.

2.2.2. Existing vapour bubble growth rates in three cavitation regimes

Determining the bubble growth rate or collapse/condensation rate dR/dt is the key issue in modelling the cavitation with thermodynamic effect. The effect of superheat on vapour bubble growth rate has been studied since 1930 based on the simplified Rayleigh-Plesset equation, heat conduction equation and Clausius-Clapeyron relation or saturated pressure-temperature relation. In those studies, the simplified Rayleigh-Plesset equation of spherical vapour bubbles was updated with temperature-dependant vapour pressure and solved analytically [33,23,34] or semi-analytically [35–39] by coupling with the 1D heat conduction equation in the radial direction of a vapour bubble to obtain the growth rate of vapour bubble radius at various superheat or heat diffusion-controlled conditions. Additionally, the full Rayleigh-Plesset equation and 1D conductive heat transfer equation have been solved numerically to cover a wide range of Jakob numbers for bubble growth [40–46] and for bubble collapse [47,48] and for the both [49]. The semi-analytically solved simplified Rayleigh-Plesset equation and 1D heat conduction equation, and numerically solved full Rayleigh-Plesset equation and 1D heat conduction equation have little interest to the cavitation model in terms of methodology due to the complicated algorithm and considerable time-consumption, thus they are no longer detailed.

The analytically solved simplified Rayleigh-Plesset equation and coupled 1D heat conduction equation of spherical vapour bubbles are most suitable for the cavitation model with thermodynamic effect because of the straightforward algorithm and negligible time-consumption. There are three cavitation regimes, namely inertia-controlled regime, intermediate regime, and heat diffusion-controlled regime [50]. In the inertia-controlled regime, the vapour bubble growth rate is decided solely by the simplified Rayleigh-Plesset equation.

When non-condensable gas, liquid viscosity, surface tension, and dynamic term $\frac{d^2R}{dt^2}$ are ignored, the full Rayleigh-Plesset equation, i.e. Eq. (2), is reduced to the simplified equation with temperature-dependant vapour pressure:

$$\frac{3}{2}\left(\frac{dR}{dt}\right)^2=\frac{p_v(T)-p}{\rho_l} \tag{7}$$

From Eq. (7), the vapour bubble growth rate in inertia-controlled regime is calculated by:

$$\frac{dR}{dt}=\sqrt{\frac{2}{3}\frac{p_v(T)-p}{\rho_l}} \tag{8}$$

In heat diffusion-controlled regime the vapour bubble growth depends on uniform superheat only. There are two approaches to deal with that issue, one is interface heat transfer balance method, and one is unsteady heat conduction method. The interface heat transfer balance method was attributed to Bosnjakovic who proposed a model of vaporization process at uniform superheat in 1930 [33]. In the method, a temperature drop between liquid and vapour occurs at the interface between a vapour bubble and its surrounding liquid, which resembles a thin boundary layer. Based on the energy balance across the interface, a relationship between bubble growth rate $\frac{dR}{dt}$, temperature drop $T_\infty-T_v$, and interface heat transfer coefficient U yields [33]

$$\mathscr{L}\rho_v\frac{dR}{dt}=U(T_\infty-T_v) \tag{9}$$

where $\mathscr{L}$ is latent heat of liquid, U is heat transfer coefficient across the bubble boundary. Unfortunately, how to specify U value is difficult and still is challenging.

In the unsteady heat conduction method, it is considered that unsteady spherically symmetric heat conduction takes place in the semi-infinite liquid field outside a vapour bubble. The unsteady heat conduction equation without vapour bubble surface movement in a spherical coordinate system is written as:

$$\rho_l c_{pl}\frac{\partial T}{\partial t}=\lambda_l\frac{1}{r^2}\frac{\partial}{\partial r}\left(r^2\frac{\partial T}{\partial r}\right) \tag{10}$$

where λ_l is liquid thermal conductivity, r is the radial coordinate of the spherical coordinate system, c_{pl} is specific heat of liquid. Eq. (10) is solved with a proper initial condition and the boundary conditions on the vapour bubble surface and in far field. However, the solution of Eq. (10) is an integral of Green's function. When the solution was involved in the Rayleigh-Plesset equation, a transcendental equation for the vapour bubble growth rate was resulted, thus, the growth rate could not be expressed analytically and explicitly [35].

Eq. (10) was transformed into to the Lagrange coordinates $\{\frac{1}{3}[r^2-R^3(t)],t\}$ from the Eulerian coordinates (r,t). The transformed equation was solved by using the perturbation method. The zero-order solution was expressed by an integral of R and $\frac{\partial T}{\partial r}$ on the bubble surface [51]. That zero-order solution was coupled with the Rayleigh-Plesset equation, and an integral-differential equation for vapour bubble radius was gained. The special solutions in the initial (inertia-controlled) and final (heat diffusion-controlled)

growth stages were estimated and the leading term of the asymptotic growth rate in the heat diffusion-controlled growth stage was derived [36]:

$$\mathscr{L}\rho_v\frac{dR}{dt}=\sqrt{\frac{3}{\pi}}\frac{\lambda_l}{\sqrt{\mathscr{D}_l t}}(T_\infty-T_v) \tag{11}$$

where $\mathscr{D}_l$ is thermal diffusivity of liquid, $\mathscr{D}_l=\lambda_l/\rho_l c_{pl}$. The zero-order solution was also adopted in [42] to investigate vapour bubble growth rate in superheated liquids numerically. Another transform method was proposed to solve Eq. (10) [38], however, an analytical growth rate could not be achieved, thus, the method was no longer discussed. Compared with Eq. (9), Eq. (10) does not require an interface heat transfer coefficient that is quite difficult to be determined, thus it can be easily used in a cavitation model when the time t is chosen to be the characteristic or reference time of a flowing system.

Eq. (9) or (11) has been used to correct the vapour bubble growth rate in inertia-controlled regime estimated by means of Eq. (8) to handle thermodynamic effect in cavitation. That correction in vapour bubble growth rate appears questionable because Eqs. (9) and (11) represent the bubble growth rate in heat diffusion-controlled regime. Various methods for implementing thermodynamic effect in cavitation models are demonstrated briefly with Table B2 in Appendix B. There exists the multiple cavitation regime model in the table. For example, the vapour bubble growth in cavitation with thermodynamic effect experiences initially inertia-controlled growth rate determined by Eq. (8), then follows the superheat-controlled growth rate given by Eq. (11) [52] or Eq. (9) [53]. However, it was considered that the minimum one in the growth rates given by Eqs. (8) and (11) should be the growth rate in the cavitation ranging from inertia-controlled to heat diffusion-controlled regimes [54]. Obviously, the intermediate regime between the inertia-controlled and heat diffusion-controlled regimes are not taken into account in the existing multiple cavitation regime models. Here a new multiple cavitation regime model will be addressed.

2.2.3. New bubble growth rate

As stated in Section 2.2.2, there are no analytical vapour growth bubble rates by solving the Rayleigh-Plesset equation together with Eq. (9) or (10) or (11) to cover inertia-controlled, intermediate and heat diffusion-controlled cavitation regimes. Therefore, the other way has to be sought to establish a vapour bubble growth rate for multiple cavitation regimes. Fortunately, an approach was proposed in [23] by putting Eqs. (7) and (11) as well as the Clausius-Clapeyron equation together to find the vapour bubble rate in multiple cavitation regimes under superheat conditions. This work was improved by replacing the Clausius-Clapeyron equation with linear interpolation on the saturated pressure-temperature line [34]. These two pieces of study have shed light on the derivation of a new bubble growth rate in cavitation with thermodynamic effect.

The cavitation with thermodynamic effect driven by hydrodynamic pressure in a flowing system is different in nature from the cavitation driven by superheat. The pressure effect on cavitation in the former, is more dominant than the thermodynamic effect in the latter, as shown in Fig. 1. The liquid pressure and vapour pressure terms in the simplified Rayleigh-Plesset equation do not need to be replaced with liquid temperature and vapour temperature by using the Clausius-Clapeyron equation or linear interpolation on the saturated pressure-temperature line. In this context, the analytical vapour bubble growth rate must be updated and reformulated to make it suitable for cavitation with thermodynamic effect.

First, Eq. (7) is nondimensionalised by employing a constant A and the parameter NPSHa as follows:

$$\frac{1}{A^2}\left(\frac{dR}{dt}\right)^2-\frac{p_v(T)-p}{\text{NPSHa}}=0 \tag{12}$$

where the constant A and NPSHa are expressed as:

$$A=\sqrt{\frac{2}{3}\frac{NPSHa}{\rho_l}},\ \text{NPSHa}=p_\infty-p_v(T_\infty) \tag{13}$$

Second, Eq. (11) is written as the following dimensionless form by using a constant B and the subcooling ΔT_{sub}:

$$\frac{2\sqrt{t}}{B}\frac{dR}{dt}-\frac{T_\infty-T_v}{\Delta T_{sub}}=0 \tag{14}$$

where the constant B and subcooling ΔT_{sub} are defined as:

$$B=\sqrt{\frac{12}{\pi}\mathscr{D}_l}\text{J},\ \text{J}=\frac{\rho_l c_{pl}\Delta T_{sub}}{\rho_v\mathscr{L}},\ \Delta T_{sub}=T_{sat}-T_\infty \tag{15}$$

where J is Jakob number, and $T_{sat}=T_v(p_\infty)$.

Third, coupling Eqs. (12) and (14) and a quadratic equation in dR/dt reaches and reads as:

$$\frac{1}{A^2}\left(\frac{dR}{dt}\right)^2+\frac{2\sqrt{t}}{B}\frac{dR}{dt}-\left(\frac{p_v(T)-p}{\text{NPSHa}}+\frac{T_\infty-T_v}{\Delta T_{sub}}\right)=0 \tag{16}$$

The positive root of Eq. (16) gives the vapour bubble growth rate. Based on the quadratic formula, the growth rate is written as:

$$\frac{dR}{dt}=A\left(\sqrt{\left(\frac{p_v(T)-p}{\text{NPSHa}}+\frac{T_\infty-T_v}{\Delta T_{sub}}\right)+\frac{A^2}{B^2}t}-\sqrt{\frac{A^2}{B^2}t}\right),\ p_v(T)\geq p \tag{17}$$

where t is time scale of bubble growth and approximated with the characteristic or reference of a flowing system, $t\approx D_{ref}/u_{ref}$, D_{ref} and u_{ref} are characteristic/reference length and velocity of the flowing system, respectively. The negative value of dR/dt in Eq. (17) serves as the vapour bubble collapse/condensation rate at $p_v(T)<p$, i.e.

$$-\frac{dR}{dt}=-A\left(\sqrt{\left(\frac{p-p_v(T)}{\text{NPSHa}}+\frac{T_\infty-T_v}{\Delta T_{sub}}\right)+\frac{A^2}{B^2}t}-\sqrt{\frac{A^2}{B^2}t}\right),\ p_v(T)<p \tag{18}$$

Substituting dR/dt and $-dR/dt$ in Eq. (1) with Eqs. (17) and (18), respectively, the source terms m_{vap} and m_{con} are updated as follows:

$$\begin{cases} m_{vap}=F_{vap}(4\pi N)^{1/3}(3\alpha)^{2/3}(1-\alpha)^{4/3}\frac{\rho_l\rho_v}{\rho}A \\ \qquad\times\left(\sqrt{\left(\frac{p_v(T)-p}{\text{NPSHa}}+\frac{T_\infty-T_v}{\Delta T_{sub}}\right)+\frac{A^2}{B^2}t}-\sqrt{\frac{A^2}{B^2}t}\right) \\ m_{con}=-F_{con}(4\pi N)^{1/3}(3\alpha)^{2/3}(1-\alpha)^{4/3}\frac{\rho_l\rho_v}{\rho}A \\ \qquad\times\left(\sqrt{\left(\frac{p-p_v(T)}{\text{NPSHa}}+\frac{T_\infty-T_v}{\Delta T_{sub}}\right)+\frac{A^2}{B^2}t}-\sqrt{\frac{A^2}{B^2}t}\right) \end{cases} \tag{19}$$

Eq. (19) reflects effects of both hydrodynamic pressure difference and temperature difference on cavitation simultaneously. The equation has covered the multiple cavitation regimes. The cavitation model proposed in the section has been coded in CEL and implemented in ANSYS CFX as user cavitation model.

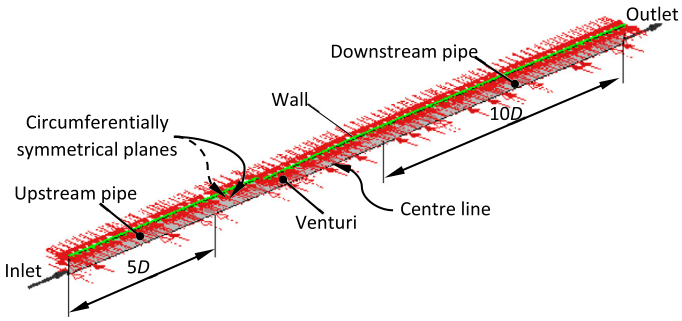

Fig. 2. Computational domain of the venturi test section in [24], the red arrows in opposite directions indicate symmetrical boundary condition, D is diameter of the approach section.

3. Validation

The tested cavitating flows of organic fluid R114 in a venturi [24], LN2 and LH2 over a tapered hydrofoil [25], and warm water around the NACA 0015 hydrofoil [26] were employed to validate the cavitation model in Section 2.2. The model constants F_{vap} and F_{con} are alternated to match measured cavity lengths by using the bisection method. Subsequently, the validated model constants F_{vap} and F_{con} were applied to predict the cavitating flow of organic fluid R245fa in a diaphragm pump.

3.1. Cavitation of R114 in a venturi

Cavitation of liquid R114 on the wall of a venturi was measured and visualised in a closed-loop hydrodynamic tunnel by reducing far field pressure [24]. The approach velocity to the venturi varied in (5.8–13.4) m/s, and the bulk liquid temperature in (−5–26.7) °C. The venturi has 44.3 mm diameter approach section and 35 mm diameter throat section, and the geometrical details are referred to [24] and omitted here because the drawing of the venturi is unclear after scaled down.

R114 is clear, colourless liquid with a normal boiling point of 3.8 °C. The reference state of R114 is specified at −6.7 °C temperature and 66.82 kPa pressure, the vapour reference specific enthalpy and Molar mass are 143,859.98 J kg^{-1} and 170.9 g mol^{-1}. The liquid reference specific enthalpy and entropy and the vapour reference specific entropy are set to be zero.

Based on the software REFPROP, the liquid and vapour densities ρ_l, ρ_v, specific heat capacities c_{pl}, c_{pv}, dynamic viscosities μ_l, μ_v, thermal conductivities λ_l, λ_v, saturated vapour pressure p_v and saturated vapour temperature T_v, latent heat $\mathscr{L}$, thermal diffusivity $\mathscr{D}$, and maximal liquid-vapour-density-ratio $(\rho_l/\rho_v)_{max}$ and surface tension γ of R114 are extracted in a range of temperature of 240–350 K and best fitted by mathematical expressions in terms of far field liquid temperature T_∞ or local temperature T. The corresponding mathematical expressions of these properties are listed in Appendix C. The expressions were implemented in CFX-Pre with CEL.

The circular cross-section of the tested venturi allows to assume flow to be circumferentially symmetrical, hence the venturi with a sector in central angle $\Delta\phi$=5° was adopted in CFD simulations. To assure a uniform boundary condition, the fluid domain was expanded into 5D upstream and 10D downstream, respectively, as illustrated in Fig. 2. Inlet boundary condition, no-slip smooth wall condition, symmetrical condition, and outlet boundary condition were used as the boundary conditions. A known static pressure, bulk liquid temperature and zero gradients are given to the fluid velocities and turbulence variables at the inlet, while a known mass flow rate is specified at the outlet.

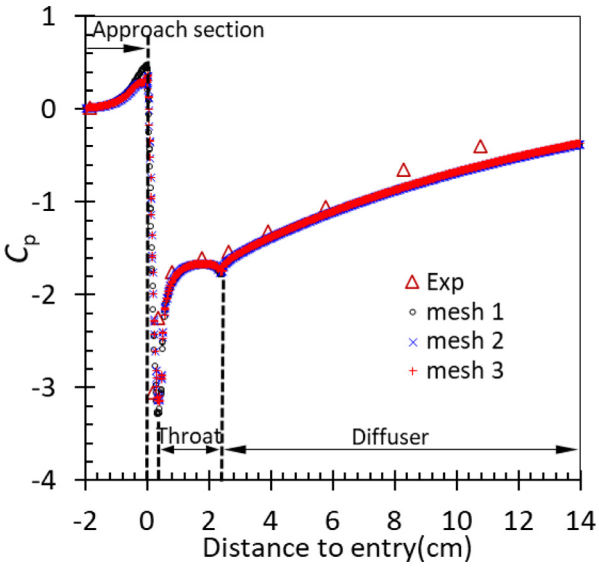

Fig. 3. Experimental pressure coefficient profiles along the venturi wall compared with those predicted with mesh 1, 2 and 3 under non-cavitation condition in Case 1, Exp-experimental data from [24].

The flow models are composed of the Reynolds time-averaged Navier-Stokes equations, $k-\omega$ two-equation turbulence model and energy equation presented by Eqs. (A1)–(A6) as well as the cavitation model Eq. (19). High resolution scheme and 2nd-order scheme are selected for the advection terms and diffusion terms in the governing equations and turbulence model. Residual tolerance error of numerical solutions is set to be 10^{-6}.

The conventional cavitation number K, approach or far field liquid velocity u_∞ and temperature T_∞ are known [24]. The conventional cavitation number K for dynamic similarity of cavitating flows is calculated with the vapour pressure in far field liquid temperature as [24]:

$$K = \frac{p_\infty - p_v(T_\infty)}{\rho_l(T_\infty)\frac{u_\infty^2}{2}} \tag{20}$$

Because T_∞ has been known in experiment, the liquid density $\rho_l(T_\infty)$ and vapour pressure $p_v(T_\infty)$ can be calculated with Eq. (C1), then the far field static pressure p_∞ and mass flow rate m_f are determined by:

$$\begin{cases} p_\infty = K\rho_l(T_\infty)\frac{u_\infty^2}{2} + p_v(T_\infty) \\ m_f = (\Delta\phi\pi/360)\left(D^2/4\right)u_\infty \end{cases} \tag{21}$$

where $\Delta\phi$ is the central angle of the fluid domain, $\Delta\phi$=5°, D=44.3 mm, and p_∞ is applied to the inlet but m_f to the outlet. The experimental conditions in [24] and the counterparts in CFD simulations are listed in Table 1 for 11 cases in total.

The wedge cell-dominated mesh with a small number of tetrahedral cells was created in ANSYS CFX. An inflation mesh is placed near the venturi wall to resolve the boundary layer. Three sets of mesh were generated, i.e., mesh 1 (104,985 cells, 8 layer inflation near wall), 2 (212,184 cells, 22 layer inflation) and 3 (291,889 cells, 32 layer inflation) in an averaged element quality of 0.378. The mesh size independency was examined by employing mesh 1 to mesh 3 in Case 1 under non-cavitation condition. The pressure coefficient profiles along the venturi wall are compared with experimental data in Fig. 3. The pressure coefficient C_p is defined as [24]:

$$C_p = \frac{p_w - p_0}{\rho_l(T_{lb})\frac{u_0^2}{2}} \tag{22}$$

where p_w is fluid pressure on the venturi wall.

Table 1
Experimental and CFD conditions for R114 cavitation flow in the venturi.

Case	Experimental condition [24]					Condition in CFD simulation	
	u_∞ (m/s)	K	T_∞ (°C)	ρ_l (kg/m^3)	$p_v(T_\infty)$ (Pa)	p_∞ (Pa)	m_f (kg/s)
1	5.83	2.30	−13.50	1565.78	50,173.94	111,349.88	0.1929
2	5.80	2.14	−2.72	1535.85	78,672.18	133,915.26	0.1882
3	5.83	1.79	15.94	1481.99	157,840.83	202,903.81	0.1825
4	9.56	2.34	−14.61	1568.82	47,789.46	215,557.73	0.3169
5	9.68	2.29	−2.50	1535.23	79,374.14	244,215.50	0.3142
6	9.81	2.04	15.06	1484.61	153,031.58	298,676.64	0.3077
7	13.32	2.36	−1.28	1531.78	83,326.29	404,155.44	0.4312
8	13.54	2.18	16.94	1479.03	163,390.48	458,892.80	0.4231
9	10.21	2.27	15.06	1484.61	153,031.58	328,618.92	0.3202
10	10.12	2.13	15.06	1484.61	153,031.58	314,816.73	0.3173
11	9.31	2.01	15.06	1484.61	153,031.58	282,457.51	0.2922

Table 2
Experimental data and CFD simulation results for R114 cavitating flow in a venturi.

Case	Experimental data [24]						CFD simulation				
	K_{min}	Re	J	t_{ref} (ms)	ΔT (K)	L_{cav} (mm)	ΔT (K)	K_{min}	F_{vap}	F_{con}	L_{cav} (mm)
1	2.39	652,970.3	3.90	7.69	1.50	69.9	1.51	2.59	4.4315	4.4315	72.0
2	2.42	732,520.1	1.78	7.73	1.83	69.9	1.65	2.63	8.8500	8.8500	70.0
3	2.43	971,157.8	0.48	7.69	2.78	69.9	0.39	3.17	4.3000	4.3000	70.0
4	2.40	1044,928.7	8.14	4.69	2.83	69.9	2.39	2.71	0.9260	0.9260	70.0
5	2.40	1241,528.3	3.95	4.63	3.00	69.9	2.26	2.70	2.2400	2.2400	70.0
6	2.37	1576,873.9	1.36	4.57	4.06	69.9	1.04	3.12	1.0000	1.0000	70.5
7	2.43	1746,998.6	5.62	3.36	4.06	69.9	2.72	2.75	0.9600	0.9600	69.5
8	2.41	2129,513.8	2.09	3.31	5.06	69.9	2.32	2.74	2.8000	2.8000	70.0
9	2.49	1685,838.5	1.57	4.39	2.17	12.7	0.87	3.14	0.8500	0.8500	13.0
10	2.39	1663,325.7	1.47	4.43	3.50	31.8	0.91	3.14	0.8300	0.8300	31.8
11	2.39	1483,762.4	1.23	4.81	4.44	101.6	4.00	2.80	2.8000	2.8000	100.5

The predicted pressure coefficient is in good agreement with the experimental data at the throat and in the diffuser inlet region but gets slightly worse in the downstream portion of the diffuser wall. A sharp drop in the coefficient exists at the inlet to the diffuser because a jump in the curvature between the throat and the diffuser has emerged. The pressure coefficient profiles predicted in mesh 2 and mesh 3 overlaps, and the mesh size independence reaches in the two meshes. Therefore, mesh 3 is used in CFD simulations of R114 cavitating flows in the venturi.

The observed cavity lengths L_{cav} in Case 1 to Case 8 were $2\frac{3}{4}$ inch(69.9 mm), but $\frac{1}{2}$inch (12.7 mm), $1\frac{1}{4}$ inch(31.8 mm) and 4 inch(101.6 mm) in Case 9 to Case 11 [24], respectively. The bisection method is used in the validation of the cavitation model. The procedure employed to look for a pair of model constants F_{vap} and F_{con} for those cavity lengths in experimental cases in Table 1 was detailed in [21] and omitted here.

The determined F_{vap} and F_{con}, minimal cavitation number K_{min}, Reynolds number Re, Jakob number J, reference time t_{ref}, temperature depression ΔT, and cavity length L_{cav} for 11 cases are tabulated in Table 2. The typical appearance of cavitated R114 predicted in Case 6 and 10 is compared with the observation in Fig. 4. Since the visualization pictures of cavity fail to present cavity thickness information, just the cavity length was employed to judge the reasonability of the determined F_{vap} and F_{con}.

The determined model constants F_{vap} and F_{con} are plotted as a function of liquid bulk temperature T_∞, Reynolds number Re ($=u_\infty D\rho_l/\mu_l$), and Jakob number J in Fig. 5, respectively. Both F_{vap} and F_{con} decrease with increasing T_∞ and Re as well as J. However, the two constants exhibit the strongest correlation to Re in comparison with the others.

The predicted temperature depression ΔT and minimal cavitation number K_{min} are plotted as a function of bulk liquid temperature T_∞ and Reynolds number Re as well as Jakob number J in Fig. 6. The predicted mean temperature depression of 11 cases is 1.82 K compared with 3.20 K in the experiment. The predicted temperature depression ΔT rises with Reynolds number Re as the experimental ΔT does but with a gentle slope. The predicted tendency of temperature depression with liquid temperature T_∞ and Jakob number J is opposite to the tendency of the experimental temperature depression.

The minimal cavitation number K_{min} is defined based on the local minimal vapour pressure in the cavity as [24]:

$$K_{min} = \frac{p_0 - p_v(T)}{\rho_l(T_\infty)\frac{u_\infty^2}{2}} = K + \frac{p_v(T_\infty) - p_v(T)}{\rho_l(T_\infty)\frac{u_\infty^2}{2}} = K + \frac{\Delta p}{\rho_l(T_\infty)\frac{u_\infty^2}{2}} \quad (23)$$

where $\Delta p = p_v(T_\infty) - p_v(T)$ is vapour pressure depression, K_{min} is an index of cavitation similarity. If cavitation of the same liquid is similar in two flowing systems at a Reynolds number, then K_{min} is constant, or vice versa.

The experimental K_{min} is nearly constant when bulk liquid temperature T_∞ and Reynolds numbers Re as well as Jakob number J vary as shown Fig. 6, too. The predicted K_{min} varies significantly with T_∞ and Re as well as J. The predicted mean K_{min} is 2.86 compared with 2.41 in the experiment. Clearly, the cavitation model has underestimated the thermodynamic effect by 43% based on the mean ΔT or 18% based on mean K_{min}.

3.2. Cavitation of LN2 and LH2 over a tapered hydrofoil

Incipient, desinent and developed cavitation of LN2 and LH2 around a 0.5-calibre tapered hydrofoil was investigated experimentally in a water tunnel with a squared transparent test section (25.4 × 25.4 mm), both desinent and developed cavity data were acquired [25]. Those developed cavity data were chosen to validate the cavitation model in a stronger thermodynamic effect than R114. The hydrofoil used in the experiment was a two-dimensional (2D), hollow, symmetrical, tapered (1.817° taper) plate with a cylindrical leading edge (0.5 calibre) in the length-to-thickness ratio 8:1, where the length and maximum plate thickness are 63.5 mm and

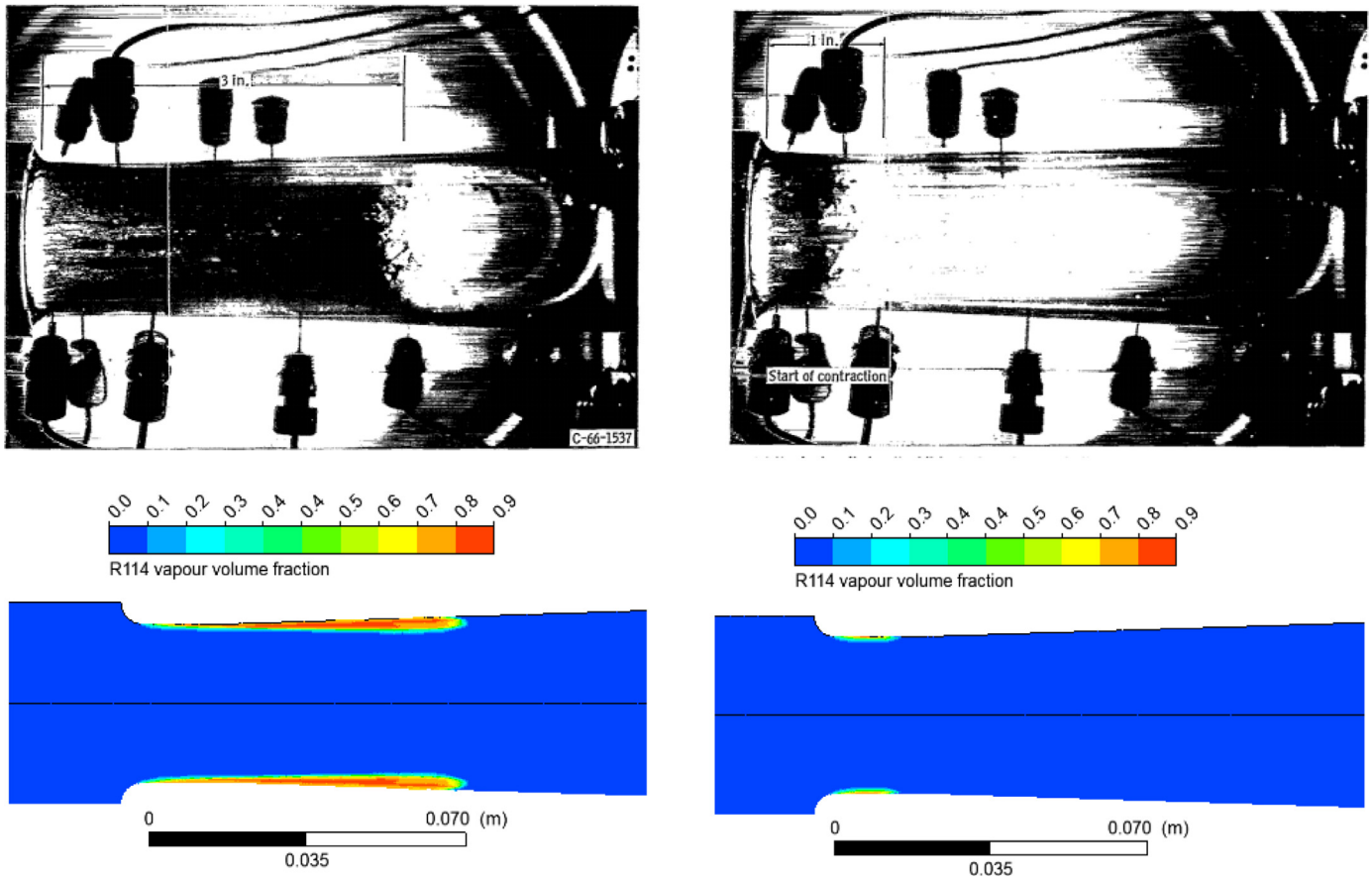

Fig. 4. Comparison of cavitation appearance of R114 in experiment and CFD simulation at the same cavitation number and approach velocity, the left pictures are for Case 6, the right for Case 10, the white and black pictures are cavitation visualisation in the venturi [24], the colourful pictures are CFD simulation in the present paper.

7.92 mm, respectively. Configuration of the hydrofoil installed in the transparent test section with a rigid metallic sting-mount assembly, and geometrical details of the hydrofoil can be found in [25], and not shown here because their drawing is unclear after scaled down.

Similarly, the liquid and vapour densities ρ_l, ρ_v, specific heat capacities c_{pl}, c_{pv}, dynamic viscosities μ_l, μ_v, thermal conductivities λ_l, λ_v, saturated vapour pressure p_v and saturated vapour temperature T_v latent heat $\mathscr{L}$, thermal diffusivity $\mathscr{D}$ and maximal liquid-vapour-density-ratio $(\rho_l/\rho_v)_{max}$ and surface tension γ of LN2 and LH2 and their vapour were extracted by using the software REFPROP were fitted in terms of far field liquid temperature T_∞ or local temperature T. Their mathematical expressions can be found in Appendix C.

Since the test section is squared and symmetrical in shape, the 0.1 mm thick, 133.5 mm long fluid domain in the section was specified and shown in Fig. 7. Inlet boundary condition, no-slip smooth wall condition, symmetrical condition, and outlet boundary condition were applied. A known static pressure, bulk liquid temperature and zero gradients are given to the fluid velocities and turbulence variables at the inlet, and a known mass flow rate is specified at the outlet. The static pressure at the inlet is calculated with the first expression in Eq. (21), while the mass flow rate is determined alternatively with the following expression:

$$m_f = \delta w u_\infty \tag{24}$$

where δ is thickness of the fluid domain, δ=0.1 mm, w is width of the domain, w=12.7 mm. The determined far field static pressure p_∞ and mass flow rate m_f are listed in Table 3 and Table 4 for LN2 and LH2, respectively.

The flow models, energy equation, cavitation model, numerical schemes and residual tolerance error adopted in this section are identical to those in Section 3.1, and no longer repeated.

Three sets of tetrahedral cell-dominated mesh with a small number of wedge cells, namely mesh 1, mesh 2 and mesh 3, where the percentage of tetrahedral cells was 73%, 80% and 83%, respectively, were created in ANSYS CFX. Two inflation meshes (15 layers with 0.01 mm thick first layer) was generated near walls of the test section and hydrofoil to resolve the boundary layer. The size and number of elements are 0.75 mm and 60,343, 0.5 mm and 123,384, 0.2 mm and 178,331 for mesh 1, mesh 2 and mesh 3, and the corresponding averaged element quality is 0.269, 0.396 and 0.479.

The mesh size independency was checked by using mesh 1 to mesh 3 for Case 51(299C) in Table 3 under non-cavitation condition of LN2. The pressure coefficient profiles on the hydrofoil surface are demonstrated in Fig. 8. It is seen that the pressure coefficient profiles predicted with three meshes are overlapped but also show particularly good agreement with the experimental data in [25]. Therefore, the mesh size independency in the three meshes reaches. The pressure coefficient profiles predicted with mesh 2 under non-cavitation condition are compared between LN2 for Case 51(299C) (Re$\approx$6.5 $\times$ 10^6) in Table 3 and LH2 for Case 19(247B) (Re$\approx$2.2 $\times$ 10^7) in Table 4. Obviously, the predicted two pressure coefficient profile curves of LN2 and LH2 are in good agreement each other. Thus, mesh 2 is adopted in the simulation of both LN2 and LH2.

Cavitating flows of LN2 and LH2 over the tapered hydrofoil were simulated based on the cavitation model proposed in Section 2.2 by alternating F_{vap} and F_{con} with the procedure de-

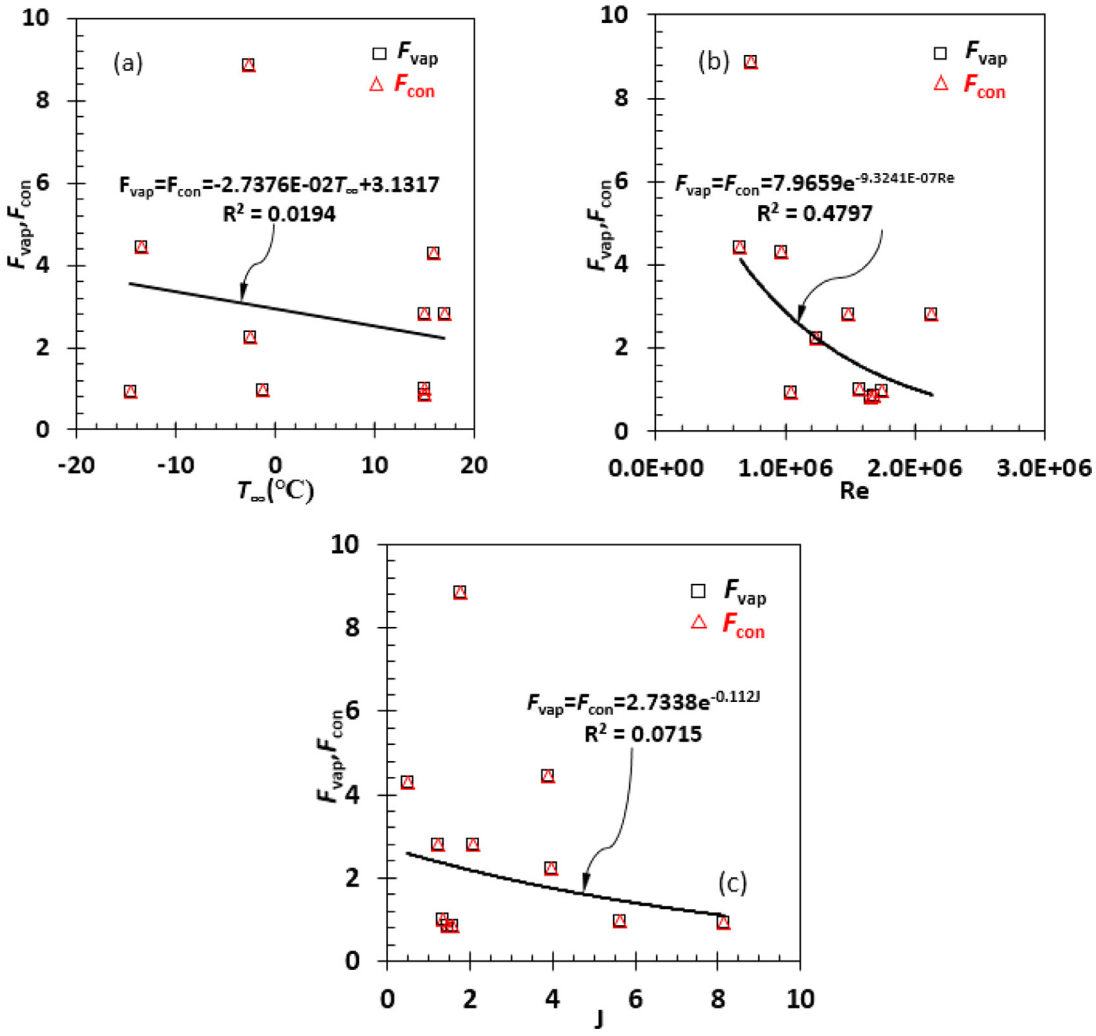

Fig. 5. Determined model constants F_{vap} and F_{con} are plotted as a function of bulk liquid temperature T_∞, Reynolds number Re and Jakob number J, respectively.

scribed in Section 3.1 to match a cavity length observed in the experiment. 73 cases with visualised cavity lengths in the experiment for LN2, but 66 cases for LH2 have been simulated. The determined F_{vap} and F_{con}, minimal cavitation number K_{min}, Reynolds number Re, Jakob number J, reference time t_{ref}, temperature depression ΔT, and cavity length L_{cav} of 54 cases for LN2 are tabulated in Table 5, and those of 55 cases for LH2 are listed in Table 6, respectively.

The determined model constants F_{vap} and F_{con} are plotted as a function of liquid bulk temperature T_∞, Reynolds number Re ($=u_\infty L\rho_l/\mu_l$, where L is chord of the hydrofoil, L=63.5 mm), Jakob number J and cavity length L_{cav} in Fig. 9 for LN2 and in Fig. 10 for LH2. In case of LN2, both F_{vap} and F_{con} decrease with increasing T_∞, Re and J but rise with increasing L_{cav}. According to R-squared (R^2) value, the two constants show the strongest correlation to Re compared with the other parameters. In case of LH2, F_{vap} declines with increasing T_∞, Re, J and L_{cav}. F_{con} rises with increasing T_∞ but reduces with increasing Re, J and L_{cav}. Based on R^2 value, the two constants demonstrate the strongest correlation to Re compared with the others once again. Generally, the mean values of constants F_{vap} and F_{con} for LN2 are larger than the mean values of F_{vap} and F_{con} for LH2. For example, the mean values of F_{vap} and F_{con} for LN2 are 0.355 and 0.134, respectively, compared with the values of 0.165 and 0.0578 for LH2.

The dependency of predicted temperature depression ΔT and minimal cavitation number K_{min} with respect to bulk liquid temperature T_∞, Reynolds number Re and Jakob number J is illustrated in Fig. 11 for LN2. The predicted ΔT trend agrees well with the experimental data for Re. However, when ΔT is plotted as a function of T_∞ or J, the predicted ΔT values show an opposite trend to the experimental ΔT. The predicted mean temperature depression of 54 cases is 1.30 K compared with 1.60 K in the experiment.

The experimental K_{min} is sightly dependant on bulk liquid temperature T_∞, Reynolds number Re and Jakob number J. The predicted K_{min} shows mere variation with Re, but exhibits a different trend in case of T_∞ and J compared with the experimental K_{min}. The predicted mean K_{min} is 1.82 compared with 1.77 in the experiment. The cavitation model underestimates the thermodynamic effect by 18.6% based on the mean ΔT or 2.5% based on the mean K_{min}.

Similarly, the variation of predicted temperature depression ΔT and minimal cavitation number K_{min} for LH2 are presented in Fig. 12. The predicted ΔT trend is similar to that of the experimental data but with a steeper slope with respect to Re. However, when the predicted ΔT is plotted with respect to T_∞ or J, the predicted ΔT values are in an opposite trend to the experimental ΔT. The predicted mean temperature depression of 55 cases is 2.31 K compared with 1.74 K in the experiment.

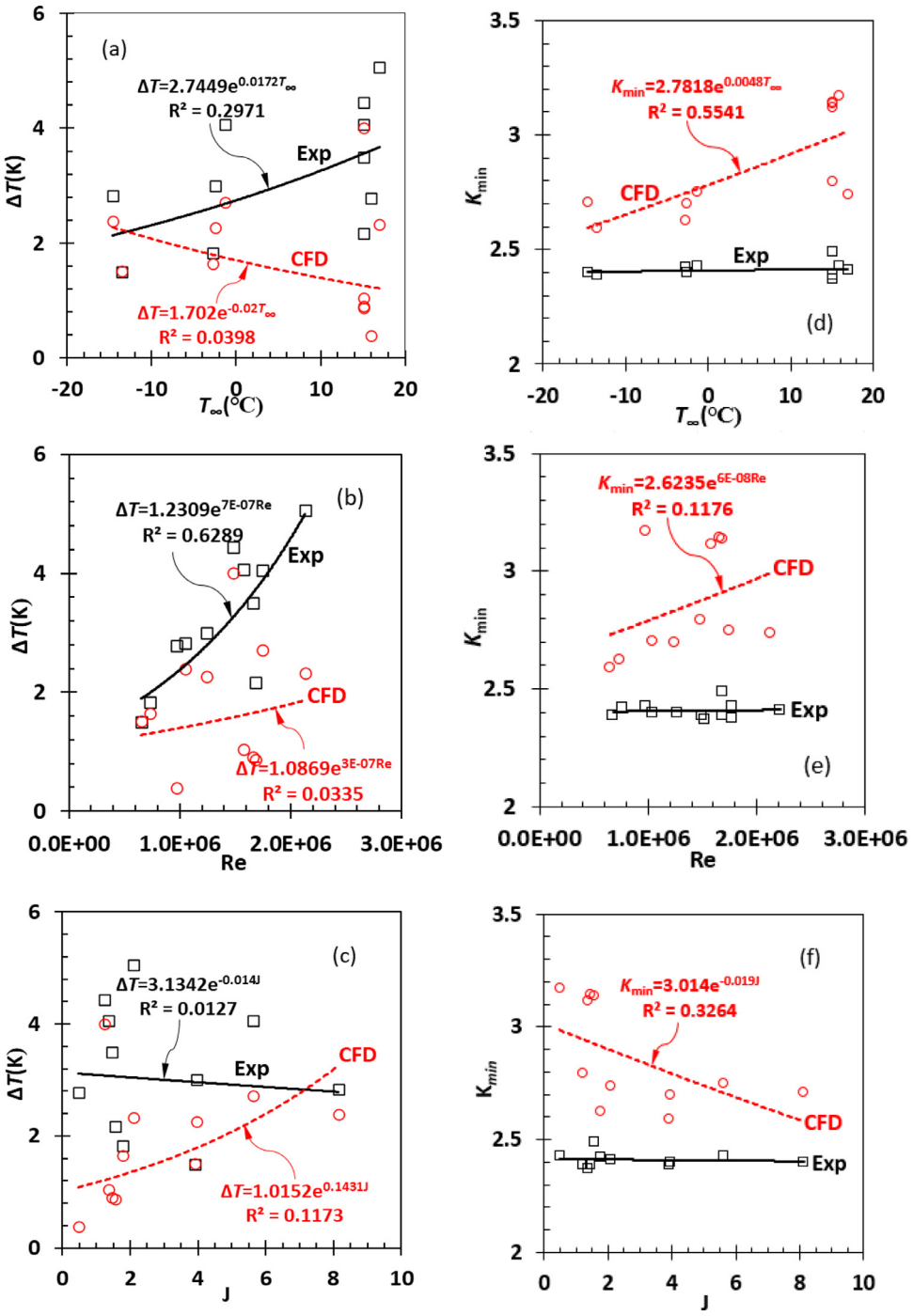

Fig. 6. Comparison of temperature depression ΔT and minimal cavitation number K_{min} between experiment and CFD prediction, the two parameters are plotted as a function of bulk temperature T_∞, Reynolds number Re and Jakob number J.

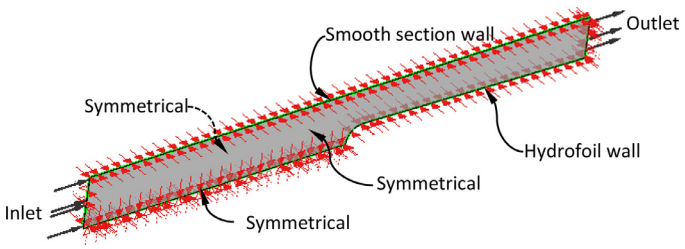

Fig. 7. Fluid domain of the hydrofoil and test section in the experiment used in [25], the short arrows represent symmetrical boundary condition, the long arrows stand for the inlet and outlet.

The experimental K_{min} is nearly constant with respect to T_∞, Re and J. The predicted K_{min} changes a little as the experimental K_{min} does with T_∞, but shows an opposite trend with Re and J compared with the experimental K_{min}. The predicted mean K_{min} is 1.82 compared with 1.77 in the experiment. The cavitation model underestimates the thermodynamic effect by 32.6% based on the mean ΔT or 0.5% based on the mean K_{min}.

Four cases, i.e., Case 20(290c) and 30 (293A) in Table 5, Case 19(247B) and 25(249D) in Table 6, have been studied numerically by a few groups [54–58] with their own developed cavitation models. The pressure difference p-$p_v(T_\infty)$ and liquid temperature T profiles of LN2 or LH2 on the tapered hydrofoil wall in these stud-

Table 3
Experimental and CFD conditions for LN2 cavitating flow over the tapered hydrofoil.

Case	Code in [25]	Experimental condition [25]			Condition in CFD simulation			
		u_∞ (m/s)	K	T_∞ (K)	ρ_l (kg/m^3)	$p_v(T_\infty)$ (Pa)	p_∞ (Pa)	m_f (kg/s)
1	282B	8.2	1.44	76.34	809.88	89,172.2	128,380	8.4341×10^{-3}
2	282E	8.1	1.47	76.35	809.84	89,278.8	128,330	8.3308×10^{-3}
3	283B	14.7	1.73	77.65	803.78	103,992	254,231	1.5006×10^{-2}
4	283C	14.5	1.80	77.71	803.50	104,716	254,231	1.4796×10^{-2}
5	284B	23.7	1.67	77.56	804.20	102,916	480,092	2.4206×10^{-2}
6	284C	23.6	1.67	77.61	803.96	102,916	477,405	2.4096×10^{-2}
7	284D	23.5	1.69	77.60	804.01	103,393	478,583	2.3996×10^{-2}
8	284E	23.6	1.71	77.73	803.41	104,956	487,535	2.4080×10^{-2}
9	285B	17.7	1.47	82.77	780.06	181,486	361,110	1.7535×10^{-2}
10	285C	17.4	1.52	83.03	778.85	186,366	365,578	1.7211×10^{-2}
11	285D	17.3	1.48	83.26	777.78	190,765	363,023	1.7089×10^{-2}
12	285E	17.2	1.50	83.57	776.33	196,823	369,075	1.6958×10^{-2}
13	285G	16.7	1.50	84.07	774.00	206,902	369,075	1.6416×10^{-2}
14	286B	16.8	1.20	88.58	752.44	316,692	444,113	1.6054×10^{-2}
15	288A	12.3	1.47	83.79	775.31	201,210	287,422	1.2111×10^{-2}
16	288D	12.5	1.33	83.79	775.31	201,210	277,804	1.2308×10^{-2}
17	289A	23.7	1.51	88.58	752.44	316,692	635,795	2.2648×10^{-2}
18	289B	23.7	1.51	88.58	752.20	318,117	638,618	2.2545×10^{-2}
19	289C	23.5	1.55	88.64	752.15	318,402	640,327	2.2448×10^{-2}
20	290C	23.9	1.70	83.06	778.71	186,933	565,032	2.3636×10^{-2}
21	290D	24.0	1.65	83.16	778.25	188,841	558,677	2.3721×10^{-2}
22	290E	23.8	1.79	83.22	777.97	189,994	564,576	2.3515×10^{-2}
23	291A	9.9	1.62	77.92	802.52	107,275	170,990	1.0090×10^{-2}
24	292C	9.8	1.31	76.48	809.23	90,885	141,576	1.0072×10^{-2}
25	292D	9.7	1.36	76.50	809.13	90,885	142,653	9.9677×10^{-3}
26	292E	9.8	1.33	76.50	809.13	90,885	142,560	1.0071×10^{-2}
27	292F	9.6	1.40	76.53	808.99	91,211.3	143,399	9.8633×10^{-3}
28	292H	9.6	1.33	76.57	808.81	91,211.3	141,211	9.8610×10^{-3}
29	292J	9.8	1.32	76.53	808.99	91,211.3	142,489	1.0069×10^{-2}
30	293A	24.0	1.75	77.64	803.82	103,871	508,998	2.4501×10^{-2}
31	293B	23.9	1.75	77.67	803.69	104,232	505,920	2.4394×10^{-2}
32	293C	23.9	1.71	77.71	803.50	104,716	497,133	2.4389×10^{-2}
33	293D	23.7	1.74	77.79	803.13	105,685	498,149	2.4173×10^{-2}
34	293F	23.9	1.70	77.90	802.62	107,029	496,723	2.4362×10^{-2}
35	294C	10.7	1.55	77.94	802.43	107,521	178,721	1.0904×10^{-2}
36	294D	10.5	1.60	77.95	802.39	107,647	178,417	1.0710×10^{-2}
37	294E	9.9	1.75	77.95	802.39	107,647	176,458	1.0088×10^{-2}
38	294F	9.8	1.78	77.94	802.43	107,521	176,110	9.9871×10^{-3}
39	294H	10.0	1.61	78.15	801.46	110,138	174,656	1.0179×10^{-2}
40	295B	24.4	1.64	83.16	778.25	188,841	568,791	2.4116×10^{-2}
41	295C	24.4	1.64	83.22	777.97	189,994	569,805	2.4108×10^{-2}
42	295D	24.3	1.68	83.20	778.06	189,607	575,545	2.4012×10^{-2}
43	295E	24.4	1.63	83.19	778.11	189,419	566,984	2.4112×10^{-2}
44	295F	24.4	1.64	83.23	777.92	190,186	569,975	2.4106×10^{-2}
45	295G	24.3	1.68	83.20	778.06	189,607	575,545	2.4012×10^{-2}
46	296C	23.7	1.48	88.58	752.44	316,692	629,444	2.2648×10^{-2}
47	296D	23.4	1.54	88.62	752.25	317,829	634,990	2.2355×10^{-2}
48	296E	23.4	1.50	88.64	752.15	318,402	627,285	2.2352×10^{-2}
49	296F	23.3	1.56	88.6	752.34	317,263	635,846	2.2263×10^{-2}
50	299B	17.8	1.40	83.36	777.32	192,702	365,101	1.7572×10^{-2}
51	299C	17.6	1.38	83.40	777.13	193,482	359,581	1.7370×10^{-2}
52	299D	17.6	1.40	83.34	777.41	193,482	360,879	1.7377×10^{-2}
53	301B	15.0	1.67	77.85	802.85	106,416	257,251	1.5294×10^{-2}
54	301C	14.9	1.64	77.86	802.80	106,539	252,686	1.5191×10^{-2}

ies were extracted and compared with the profiles predicted by using the cavitation model here to validate the model.

The pressure difference p-$p_v(T_\infty)$ and liquid temperature T profiles of LN2 on the tapered hydrofoil wall in Case 20(290C) and Case 30 (293A) are illustrated in Fig. 13. Obviously, all the predicted p-$p_v(T_\infty)$ and T curves cannot exactly match the corresponding experimental data. For Case 290C, the cavity length seems to be underestimated by the models in [54,55] based on the predicted p-$p_v(T_\infty)$ profiles. The T curve predicted by using the present cavitation model is the closest to the experimental data amongst the other models. For Case 293A, the cavity length is underestimated by the model in [55] and a sharper drop in the predicted T curves than the experimental data is observed for the models in [54,55] compared with the present cavitation model.

Likewise, the comparison between the present model and the previous models for the pressure difference p-$p_v(T_\infty)$ and liquid temperature T profiles of LH2 on the tapered hydrofoil wall in Case 19(247B) and Case 25(249D) is shown in Fig. 14. The predicted p-$p_v(T_\infty)$ and T curves are unable to match the experimental data accurately. For Case 247B, the cavity length estimated by the models in [54,55] is shorter than the experimental cavity length based on the predicted p-$p_v(T_\infty)$ profiles. The T curve predicted by using the present cavitation model is far too lower than the experimental data. For Case 249D, the cavity length predicted by the model in [55] is shorter than the experimental cavity length. Compared with the cavitation models in [54,55,58], the present cavitation model leads to a significant drop in the T curve. This matter of fact suggests that the present

Table 4
Experimental and CFD conditions for LH2 cavitating flow over the tapered hydrofoil.

Case	Code in [25]	Experimental condition [25]			Condition in CFD simulation			
		u_∞ (m/s)	K	T_∞ (K)	ρ_l (kg/m^3)	$p_v(T_\infty)$ (Pa)	p_∞ (Pa)	m_f (kg/s)
1	231B	51.8	1.30	20.57	70.29	106,594	229,192	4.6243×10^{-3}
2	231C	51.4	1.34	20.63	70.22	108,497	232,796	4.5839×10^{-3}
3	231D	50.4	1.47	20.61	70.23	107,860	238,987	4.4955×10^{-3}
4	232B	64.9	1.59	20.96	69.83	119,412	353,251	5.7559×10^{-3}
5	233B	52.4	1.31	20.59	70.26	107,226	233,583	4.6755×10^{-3}
6	233C	52.1	1.38	20.56	70.30	106,279	237,945	4.6515×10^{-3}
7	235B	59.0	1.41	20.88	69.92	116,696	288,294	5.2393×10^{-3}
8	235C	58.3	1.47	20.88	69.92	116,696	291,376	5.1772×10^{-3}
9	239B	54.7	1.09	22.55	67.72	183,442	293,880	4.7048×10^{-3}
10	239C	55.0	1.13	22.52	67.76	182,047	297,865	4.7334×10^{-3}
11	240B	66.6	1.50	21.25	69.47	129,646	360,765	5.8763×10^{-3}
12	240C	66.5	1.48	21.45	69.22	129,646	363,590	5.8461×10^{-3}
13	241B	55.3	1.25	21.27	69.46	130,375	263,125	4.8779×10^{-3}
14	242B	59.4	1.47	20.70	70.14	110,749	292,653	5.2914×10^{-3}
15	243B	58.7	1.54	20.70	70.14	110,749	296,850	5.2291×10^{-3}
16	245B	39.6	1.03	20.43	70.44	102,249	159,138	3.5427×10^{-3}
17	245D	39.2	1.10	20.50	70.36	104,405	163,874	3.5030×10^{-3}
18	246A	64.0	1.64	20.84	69.98	115,355	350,399	5.6880×10^{-3}
19	247B	65.2	1.68	20.69	70.15	110,425	360,916	5.8086×10^{-3}
20	247C	66.4	1.56	20.79	70.04	113,694	354,550	5.9061×10^{-3}
21	248B	52.1	1.46	20.49	70.39	104,095	243,566	4.6572×10^{-3}
22	248C	51.2	1.60	20.46	70.41	103,169	250,824	4.5782×10^{-3}
23	249B	58.4	1.49	20.60	70.26	107,543	286,061	5.2110×10^{-3}
24	249C	57.8	1.65	20.63	70.22	108,497	302,039	5.1546×10^{-3}
25	249D	58.1	1.57	20.70	70.14	110,749	296,617	5.1756×10^{-3}
26	251B	56.5	1.23	22.09	68.38	162,868	297,118	4.9068×10^{-3}
27	251C	55.3	1.40	22.09	68.38	162,868	309,250	4.8025×10^{-3}
28	252B	60.6	1.43	21.30	69.42	131,473	313,741	5.3424×10^{-3}
29	252C	60.4	1.46	21.43	69.28	135,557	320,051	5.3141×10^{-3}
30	254B	50.8	1.50	20.44	70.44	102,555	238,881	4.5442×10^{-3}
31	254C	51.0	1.44	20.53	70.33	105,339	237,042	4.5551×10^{-3}
32	254D	50.9	1.41	20.45	70.42	102,861	231,481	4.5520×10^{-3}
33	255B	66.8	1.39	22.15	68.30	165,453	377,265	5.7942×10^{-3}
34	255C	66.4	1.49	22.20	68.22	167,629	391,725	5.7533×10^{-3}
35	256A	59.2	1.63	21.08	69.75	121,480	320,714	5.2443×10^{-3}
36	257B	66.6	1.58	21.08	69.64	121,480	368,996	5.8900×10^{-3}
37	258B	66.7	1.56	21.27	69.46	130,375	371,392	5.8835×10^{-3}
38	258C	65.3	1.70	21.35	69.37	133,318	384,731	5.7526×10^{-3}
39	260B	52.1	1.37	20.72	70.11	111,398	241,761	4.6391×10^{-3}
40	260C	51.1	1.44	20.72	70.11	111,398	243,213	4.5500×10^{-3}
41	260D	50.2	1.57	20.81	70.01	114,356	252,848	4.4633×10^{-3}
42	261B	39.1	1.09	20.46	70.41	108,497	161,832	3.4962×10^{-3}
43	261C	38.8	1.13	20.45	70.42	102,861	162,757	3.4699×10^{-3}
44	261D	38.8	1.21	20.45	70.42	102,861	166,998	3.4699×10^{-3}
45	262B	39.8	1.09	20.57	70.29	106,594	167,278	3.5530×10^{-3}
46	262C	39.2	1.16	20.57	70.29	106,594	169,243	3.4995×10^{-3}
47	262D	38.8	1.25	20.61	70.23	107,860	173,942	3.4608×10^{-3}
48	263B	52.6	1.40	21.24	69.50	129,283	263,878	4.6425×10^{-3}
49	263C	51.8	1.52	21.20	69.54	127,838	269,653	4.5749×10^{-3}
50	264B	57.3	1.20	22.31	68.07	172,490	306,593	4.9538×10^{-3}
51	264C	56.2	1.35	22.32	68.056	172,936	318,027	4.8574×10^{-3}
52	265D	45.7	1.20	22.25	68.15	169,827	255,224	3.9553×10^{-3}
53	269A	64.1	1.18	23.02	67.029	206,303	368,792	5.4566×10^{-3}
54	273B	52.5	1.10	22.23	68.18	208,848	272,309	4.5462×10^{-3}
55	281A	65.5	1.22	23.07	66.93	208,848	384,001	5.5674×10^{-3}

cavitation model overpredicts thermodynamic effect for these cases.

3.3. Cavitation of water around NACA 0015 hydrofoil

The current cavitation model is validated further by using the experimental data of water in [26]. In that study, the cavity length and unsteady pressure spectra of developed cavitation of water around a NACA 0015 hydrofoil installed in a thermal cavitation tunnel were measured at angles of attack AOA=0, 2, 4, 5, 6, 8, 10°, water far field temperature T_∞=25, 50, 70 °C, cavitation number K=1.2–3.0 and a fixed water far field velocity u_∞=8 m/s. The hydrofoil with 115 mm chord and 80 mm span was mounted on a rotatable panel at the bottom of the rectangular test section in dimensions 120(width) × 80(heigh) × 500mm(length). The cavitating flows around the NACA 0015 hydrofoil are similar to the cavitating flows in a rotodynamic pump. Since the hydrofoil and test section are symmetrical about the middle span plane, a δ=0.5 mm thick fluid domain as shown in Fig. 15 is specified.

The thermophysical and transport properties of water and its vapour in 280–380 K were given in Appendix C.

The cavitating flows of water at three far field temperatures T_∞=25, 50, 70 °C were simulated based on the present cavitation model at a fixed AOA=5°, cavitation number K=1.5 and far field velocity u_∞=8 m/s. Inlet boundary condition, no-slip smooth wall condition, symmetrical condition, and outlet boundary condition are demonstrated in Fig. 15. A known static pressure, bulk liquid temperature and zero gradients are prescribed to the fluid veloci-

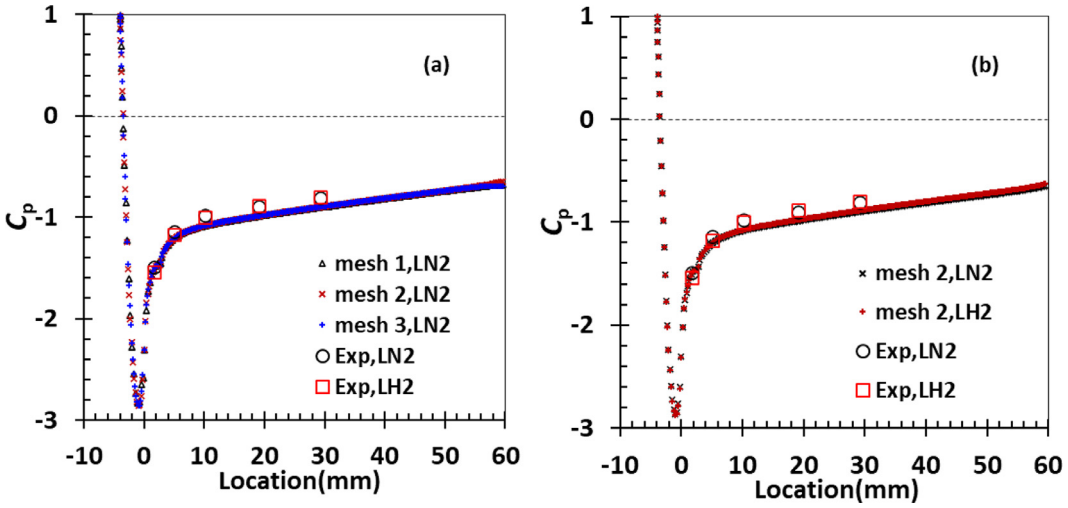

Fig. 8. Comparison of pressure coefficient C_p profiles between CFD prediction and experimental data under non-cavitation condition of LN2 at mesh 1, 2 and 3 by using Case 51 (299C) Table 3, the experimental data after [25], LH2 is for Case 19 (247B) in Table 4 under non-cavitation condition.

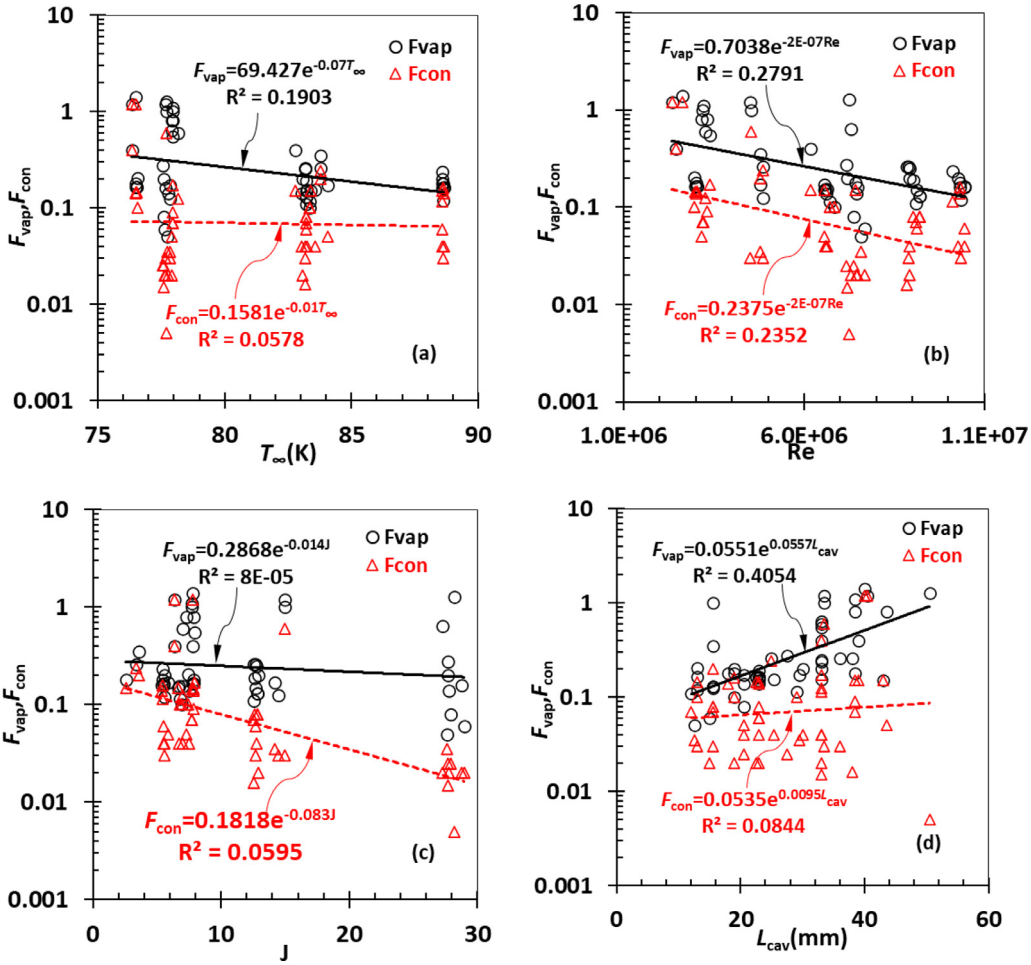

Fig. 9. Determined model constants F_{vap} and F_{con} for LN2 are plotted as a function of bulk liquid temperature T_∞, Reynolds number Re, Jakob number J and cavity length L_{cav}, respectively.

ties and turbulence variables at the inlet, and a known mass flow rate is given at the outlet. The static pressure at the inlet is calculated with the first expression in Eq. (21), while the mass flow rate is determined by using Eq. (24), δ=0.5 mm, w=120 mm and u_∞=8 m/s. The determined static pressure p_∞ and mass flow rate m_f are listed in Table 7.

The flow models, energy equation, cavitation model, numerical schemes and residual tolerance error used in this section are the same as those in Section 3.1.

Three kinds of 4-node tetrahedral element-dominated mesh with a smaller number of 6-node wedge elements, i.e., mesh 1, mesh 2 and mesh 3, where the percentage of tetrahedral elements

Table 5
Experimental data and CFD simulation results for LN2 cavitating flow over the tapered hydrofoil.

Case	Code in [25]	Experimental data [25]						CFD simulation				
		K_{min}	Re	J	t_{ref} (ms)	ΔT (K)	L_{cav} (mm)	ΔT (K)	K_{min}	F_{vap}	F_{con}	L_{cav} (mm)
1	282B	1.67	2342,089	6.36	7.74	0.59	40.6	0.78	2.01	1.200	1.200	40.5
2	282E	1.66	2453,747	6.34	7.84	0.54	33.0	0.57	1.74	0.400	0.400	33.0
3	283B	1.88	4498,375	14.97	4.32	1.16	33.0	1.63	2.14	0.030	1.200	33.5
4	283C	1.94	4539,324	14.96	4.38	0.86	17.8	1.53	2.09	0.600	1.000	33.5
5	284B	1.76	7164,106	27.68	2.69	1.36	27.9	2.42	2.04	0.025	0.275	27.5
6	284C	1.77	7192,934	27.68	2.69	1.48	33.0	2.11	2.07	0.015	0.200	33.0
7	284D	1.79	7384,351	27.95	2.70	1.28	20.3	2.03	2.19	0.025	0.080	20.5
8	284E	1.79	7586,879	27.63	2.69	1.04	12.7	1.85	2.19	0.035	0.050	12.5
9	285B	1.78	6179,891	7.77	3.59	2.29	38.1	1.67	2.00	0.150	0.400	39.0
10	285C	1.80	6624,669	7.50	3.65	1.79	20.3	0.89	1.66	0.040	0.140	20.5
11	285D	1.83	6580,665	6.97	3.67	2.38	33.0	0.97	1.66	0.040	0.155	33.0
12	285E	1.83	6648,002	6.71	3.69	2.03	25.4	0.91	1.65	0.040	0.155	25.4
13	285G	1.87	6553,297	5.89	3.80	1.63	20.3	0.78	1.65	0.050	0.170	20.5
14	286B	1.84	7432,928	2.56	3.78	2.16	38.1	0.47	1.33	0.150	0.180	38.5
15	288A	1.88	4787,484	3.60	5.16	1.17	15.2	0.51	1.64	0.200	0.350	15.5
16	288D	1.81	4866,100	3.39	5.08	1.37	25.4	0.43	1.40	0.240	0.260	25.0
17	289A	1.84	10,278,768	5.55	2.68	2.98	30.5	1.39	1.77	0.040	0.200	30.0
18	289B	1.83	10,458,741	5.52	2.69	2.98	22.9	1.35	1.72	0.060	0.160	23.0
19	289C	1.86	10,442,541	5.54	2.70	2.74	30.5	1.40	1.73	0.040	0.165	23.0
20	290C	1.81	8936,583	12.91	2.66	1.93	19.0	2.36	1.96	0.020	0.200	19.0
21	290D	1.80	8841,445	12.55	2.65	2.56	38.1	2.29	1.97	0.016	0.260	38.0
22	290E	1.82	9098,871	12.56	2.67	1.91	11.4	1.87	1.86	0.070	0.110	12.0
23	291A	1.82	3155,474	7.26	6.41	0.94	43.2	0.92	1.96	0.050	0.800	43.5
24	292C	1.57	2619,405	7.77	6.48	0.81	40.6	0.98	2.09	1.200	1.400	40.0
25	292D	1.58	2998,643	7.83	6.55	0.54	17.8	0.40	1.47	0.140	0.180	18.0
26	292E	1.55	3030,022	7.81	6.48	0.63	22.9	0.38	1.43	0.145	0.165	22.5
27	292F	1.61	2970,106	7.87	6.61	0.47	12.7	0.20	1.46	0.145	0.165	13.0
28	292H	1.65	2950,561	7.46	6.61	0.71	38.1	0.50	1.50	0.100	0.205	13.0
29	292J	1.53	3031,891	7.75	6.48	0.63	22.9	0.39	1.43	0.145	0.165	23.0
30	293A	1.83	7689,825	28.97	2.65	1.29	15.2	1.91	1.85	0.020	0.060	15.0
31	293B	1.84	7479,506	28.78	2.66	1.75	22.9	2.20	1.96	0.020	0.160	22.5
32	293C	1.82	7245,109	28.23	2.66	2.33	50.8	2.01	2.04	0.005	1.280	50.5
33	293D	1.83	7463,267	27.73	2.68	1.59	22.9	2.18	1.94	0.020	0.140	23.0
34	293F	1.78	7299,232	27.25	2.66	1.37	33.0	2.18	2.03	0.020	0.640	33.0
35	294C	1.66	3375,386	7.93	5.93	0.95	33.0	0.98	1.91	0.170	0.550	33.0
36	294D	1.73	3303,408	7.88	6.05	0.97	38.1	1.05	2.00	0.090	0.800	38.5
37	294E	1.86	3206,004	7.70	6.41	0.83	22.9	1.08	2.08	0.070	1.100	38.5
38	294F	1.86	3180,614	7.68	6.48	0.77	22.9	1.00	2.09	0.070	1.000	15.5
39	294H	1.79	3253,126	7.03	6.35	0.79	22.9	0.92	1.91	0.125	0.600	33.0
40	295B	1.81	8928,710	12.79	2.60	2.23	33.0	2.03	1.96	0.040	0.250	33.0
41	295C	1.78	9115,904	12.68	2.60	2.11	22.9	1.81	1.87	0.060	0.150	23.0
42	295D	1.78	9202,544	12.83	2.61	1.76	15.2	1.70	1.85	0.080	0.130	15.5
43	295E	1.78	8899,760	12.66	2.60	2.54	35.6	1.97	1.96	0.030	0.260	36.0
44	295F	1.78	9029,482	12.65	2.60	2.19	22.9	1.82	1.91	0.080	0.190	23.0
45	295G	1.79	9202,544	12.83	2.61	1.85	15.2	1.70	1.85	0.080	0.130	15.5
46	296C	1.81	10,111,681	5.46	2.68	3.18	33.0	1.45	1.80	0.115	0.235	33.0
47	296D	1.84	10,308,952	5.47	2.71	2.55	19.0	1.24	1.73	0.160	0.180	19.0
48	296E	1.83	10,314,040	5.36	2.71	2.9	22.9	1.36	1.71	0.140	0.160	23.0
49	296F	1.82	10,346,316	5.56	2.73	2.37	12.7	1.09	1.71	0.030	0.120	13.0
50	299B	1.68	6842,752	6.90	3.57	1.55	19.0	0.60	1.49	0.100	0.100	19.0
51	299C	1.72	6555,426	6.62	7.69	1.85	43.2	0.90	1.62	0.150	0.150	43.0
52	299D	1.71	6724,520	6.79	4.69	1.89	29.2	0.74	1.53	0.100	0.115	29.0
53	301B	1.76	4854,283	14.50	4.63	0.72	15.2	1.07	1.81	0.030	0.125	15.5
54	301C	1.76	4771,581	14.18	4.81	0.93	29.2	1.22	1.84	0.035	0.170	29.5

was 75%, 78% and 82%, respectively, were generated in ANSYS CFX. Two inflation meshes (15 layers with 0.1 mm thick first layer) was patched near walls of the test section and hydrofoil. The size and number of elements are 3 mm and 12,660, 2.5 mm and 68,259, 2 mm and 101,632 for mesh 1, mesh 2 and mesh 3, respectively, and the corresponding averaged element quality is 0.212, 0.251 and 0.324.

The mesh size independency was investigated by using mesh 1 to mesh 3 for Case 1(25 °C in Table 7 under non-cavitation condition. The pressure profiles on the hydrofoil surface are demonstrated in Fig. 16. The pressure profiles predicted with mesh2 and mesh 3 overlap, indicating the mesh size independency achieved. Thus, mesh 2 is employed in the simulation of water around the NACA 0015 hydrofoil.

The pressures profiles $-C_p$ on the NACA 0015 hydrofoil surface at T_∞=25, 50, 70 °C, AOA=5° and K=1.5 were predicted by using different F_{vap} and F_{con} and compared with the experimental counterparts in [26]. The results with the minimal error in pressure profiles between prediction and experiment are illustrated in Fig. 17, the responding values of F_{vap} and F_{con} have been declared in the figure, too. The agreement between prediction and experiment gets better with decreasing bulk temperature. It is seen that the higher the bulk temperature, the larger the model constants F_{vap} and F_{con}. For example, F_{vap} =F_{con}=0.0008, 0.003, 0.0075 are obtained when cavitation occurs at T_∞=25, 50, 75 °C, respectively.

Table 6
Experimental data and CFD simulation results for LH2 cavitating flow over the tapered hydrofoil.

Case	Code in [25]	Experimental data [25]						CFD simulation				
		K_{min}	Re	J	t_{ref} (ms)	ΔT (K)	L_{cav} (mm)	ΔT (K)	K_{min}	F_{vap}	F_{con}	L_{cav} (mm)
1	231B	1.86	17,626,847	2.93	1.23	1.35	40.6	2.59	1.96	0.0080	0.1500	41.0
2	231C	1.89	17,611,403	2.90	1.24	1.18	17.7	2.50	1.99	0.0300	0.1500	18.0
3	231D	1.98	17,225,230	3.04	1.26	0.90	10.1	2.12	2.07	0.0400	0.1500	10.5
4	232B	1.95	22,666,256	4.19	0.98	2.13	27.9	2.32	2.01	0.0050	0.1100	28.0
5	233B	1.91	17,711,276	2.98	1.21	2.45	43.1	2.62	1.99	0.0100	0.1500	43.1
6	233C	1.93	17,749,838	3.10	1.22	2.12	25.4	2.59	2.02	0.0110	0.1500	25.5
7	235B	1.97	20,241,432	3.42	1.08	2.40	43.1	4.55	2.23	0.0055	0.1600	43.0
8	235C	1.99	20,260,928	3.47	1.09	2.06	26.1	4.39	2.24	0.0080	0.1600	26.5
9	239B	2.05	20,833,330	1.44	1.16	2.53	30.4	0.78	1.44	0.1000	0.1000	30.0
10	239C	1.98	20,981,011	1.52	1.15	2.07	20.3	1.07	1.57	0.1150	0.1150	20.0
11	240B	1.89	23,523,159	3.81	0.95	1.78	19.0	3.92	2.14	0.0300	0.1600	20.0
12	240C	1.95	23,527,052	3.54	0.95	2.01	35.5	3.44	2.14	0.0090	0.1800	20.0
13	241B	1.84	19,629,501	2.48	1.15	2.11	28.4	1.66	1.74	0.0300	0.1300	29.0
14	242B	1.95	20,205,324	3.78	1.07	1.83	44.4	2.82	2.05	0.0065	0.1600	44.5
15	243B	1.97	20,180,438	3.85	1.08	2.00	20.3	2.73	2.08	0.0150	0.1600	20.0
16	245B	1.84	13,342,133	1.64	1.60	1.98	42.6	0.57	1.33	0.1300	0.1350	42.5
17	245D	1.84	13,298,503	1.66	1.62	1.56	19.0	0.82	1.53	0.1700	0.1800	19.5
18	246A	2.05	22,148,037	4.36	0.99	1.44	31.7	3.30	2.18	0.0060	0.2000	20.0
19	247B	1.96	22,397,313	4.77	0.97	1.20	15.2	5.30	2.32	0.0080	0.1300	15.5
20	247C	1.92	22,740,690	4.50	0.96	1.69	26.6	3.85	2.14	0.0100	0.1700	27.0
21	248B	1.98	17,683,245	3.32	1.22	1.87	31.7	2.02	1.98	0.0110	0.1700	31.5
22	248C	2.02	17,334,641	3.50	1.24	1.01	13.9	1.76	2.08	0.0110	0.1700	31.5
23	249B	1.95	19,675,709	3.85	1.09	1.89	39.8	5.05	2.31	0.0060	0.2000	41.0
24	249C	2.00	19,785,357	4.05	1.10	0.97	11.4	4.94	2.42	0.0250	0.2000	11.5
25	249D	1.98	19,977,016	3.84	1.09	1.26	19.0	4.09	2.28	0.0120	0.2000	19.0
26	251B	1.94	21,059,133	1.95	1.12	2.26	20.3	1.43	1.72	0.0400	0.1300	20.0
27	251C	2.02	20,618,341	2.09	1.15	1.49	10.6	0.98	1.77	0.0600	0.1300	10.5
28	252B	1.96	21,440,020	3.15	1.05	2.24	29.2	2.85	2.07	0.0300	0.1700	29.5
29	252C	1.96	21,666,384	3.07	1.05	1.68	20.3	2.83	2.08	0.0200	0.1700	20.0
30	254B	1.99	17,178,989	3.32	1.25	0.92	12.7	1.44	1.91	0.0400	0.1400	40.5
31	254C	1.97	17,343,217	3.13	1.25	1.05	18.2	1.45	1.86	0.0200	0.1400	40.5
32	254D	1.98	17,186,673	3.16	1.25	1.59	40.1	2.13	1.98	0.0100	0.1900	40.5
33	255B	2.02	24,457,692	2.76	0.95	2.55	40.6	2.83	2.09	0.0100	0.1600	40.5
34	255C	1.96	24,907,016	2.84	0.96	1.69	18.2	3.11	2.16	0.0175	0.1600	40.5
35	256A	2.00	20,749,968	3.66	1.07	1.18	10.1	2.15	2.10	0.0300	0.1400	10.0
36	257B	1.93	23,464,559	4.12	0.95	1.69	23.3	3.42	2.13	0.0100	0.1600	10.0
37	258B	1.93	23,665,340	3.91	0.95	2.01	22.8	3.44	2.14	0.0115	0.1600	10.0
38	258C	2.02	23,347,240	3.94	0.97	1.13	10.6	3.00	2.25	0.0250	0.1600	10.0
39	260B	1.88	17,934,366	2.92	1.22	1.87	28.4	1.94	1.91	0.0180	0.1700	28.5
40	260C	1.95	17,584,904	2.95	1.24	1.39	20.8	1.45	1.88	0.0185	0.1500	21.0
41	260D	2.04	17,372,609	2.97	1.26	0.84	8.8	0.94	1.89	0.0400	0.1500	9.0
42	261B	1.93	13,232,586	1.66	1.62	1.61	27.9	1.07	1.64	0.1700	0.1800	28.0
43	261C	1.94	13,142,338	1.70	1.64	1.54	19.0	0.83	1.57	0.1700	0.1800	19.5
44	261D	1.93	13,133,000	1.80	1.64	1.22	10.1	1.03	1.74	0.2400	0.2500	11.0
45	262B	1.91	13,569,313	1.64	1.60	2.03	29.2	0.93	1.57	0.1800	0.1900	29.5
46	262C	1.95	13,397,060	1.69	1.62	1.62	18.2	1.00	1.68	0.2200	0.2300	18.5
47	262D	1.96	13,269,865	1.74	1.64	1.15	9.6	1.21	1.89	0.2500	0.3000	10.0
48	263B	2.05	18,680,399	2.53	1.21	2.33	39.3	2.04	2.02	0.0090	0.2000	39.5
49	263C	2.05	18,353,858	2.67	1.23	1.61	16.5	1.73	2.08	0.0190	0.1900	16.5
50	264B	1.98	21,510,779	1.82	1.11	2.51	31.7	2.18	1.93	0.0500	0.1900	32.0
51	264C	2.00	21,216,792	1.94	1.13	1.65	17.7	1.72	1.96	0.1600	0.1800	18.0
52	265D	2.09	17,187,540	1.26	1.39	1.49	10.9	0.80	1.66	0.1600	0.1800	11.0
53	269A	1.98	24,984,084	1.75	0.99	3.23	30.2	2.00	1.81	0.1200	0.1230	30.0
54	273B	1.85	19,761,081	1.50	1.21	1.90	19.0	1.02	1.53	0.1200	0.1230	19.5
55	281A	1.92	25,477,505	1.84	0.97	2.38	27.4	2.03	1.86	0.1000	0.1400	28.0

4. Application

Unsteady cavitating flows of the organic fluid R245fa in a diaphragm pump were studied numerically with ANSYS 2019R2 CFX in suction stroke based on the k-ω turbulence model, the ZGB cavitation model, rigid body motion model for the 1D motion of valve and moving mesh technique. The thermodynamic effect in cavitation was included in the ZGB model by calibrating two model constants F_{vap} and F_{con} against cavitating flows of R114 in the venturi [24]. The cavitation inception, cavitation developed states and vortex production and entropy generation rate were clarified. Unfortunately, the ZGB model crashed when the pump inlet pressure was lower than 85.2 kPa and a complete mean pump flow rate-NPSHa curve could not be obtained; consequently, the NPSHr of the pump was not estimated. The present cavitation model will be applied to simulate the cavitating flow of R245fa in the suction stroke of the diaphragm pump in order to remove that drawback.

The diaphragm pump investigated here is the same as that studied in [21] as shown in Fig. 18. CFD simulation of cavitating flows takes place during the suction stroke, and the displacement of the diaphragm during the suction stroke is controlled by the 1D motion of the simplified crank-piston mechanism and idealised deformation of the diaphragm as indicated in Fig. 18. The displacement serves as a moving boundary condition in the CFD simulation.

Further, the suction valve is simplified to the 1D motion of a rigid body with mass, spring and fluid resistance as shown in Fig. 19. The 1D motion yields Newton's second law of motion and

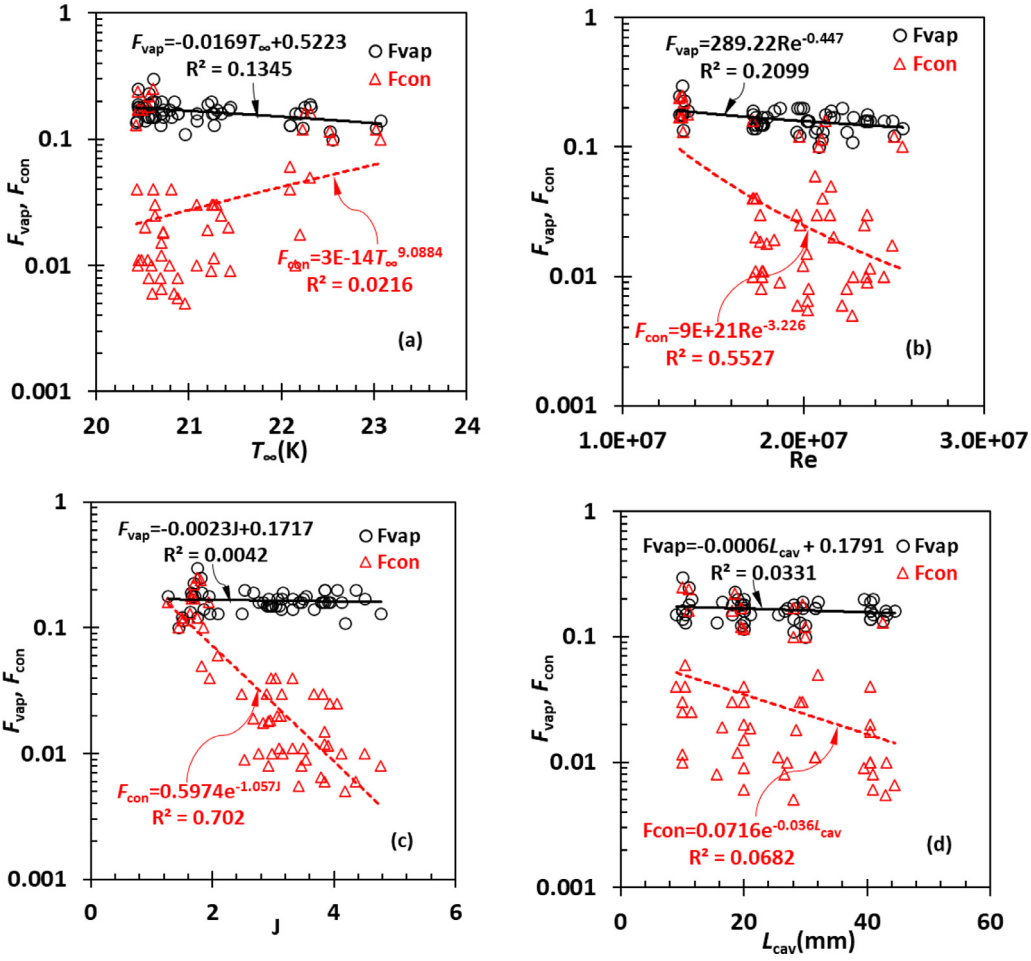

Fig. 10. Determined model constants F_{vap} and F_{con} for LH2 are plotted as a function of bulk liquid temperature T_∞, Reynolds number Re, Jakob number J and cavity length L_{cav}, respectively.

Table 7
Experimental and CFD conditions for water cavitating flow over the NACA 0015 hydrofoil.

Case	Experimental condition [26]									Condition in CFD simulation	
	u_∞ (m/s)	K	T_∞ (°C)	ρ_l (kg/m^3)	$p_v(T_\infty)$ (Pa)	Re	t_{ref} (ms)	J	ppm of air	p_∞ (Pa)	m_f (kg/s)
1	8	1.5	25	996.72	3160.6	1.01887 × 10^6	14.375	4260.6	22	51,003.3	0.478427
2	8	1.5	50	987.92	12,335.5	1.62,446 × 10^6	14.375	748.7	22	59,755.6	0.474201
3	8	1.5	70	977.97	31,252.8	2.15,504 × 10^6	14.375	203.1	22	78,195.1	0.469424

is solved numerically in ANSYS CFX in each time step. The fluid domain without spring explicitly for CFD simulations is illustrated in Fig. 19 after the symmetricity of the pump is considered. The parameters of the diaphragm, valve and spring are listed in Table 8.

The governing equations for cavitating flows of R245fa in the liquid end of the diaphragm pump are expressed by Eqs. (A1)–(A6), which are identical to those in [21], expect the ZGB cavitation model in [21] to be replaced with the present cavitation model. Since the dp/dT-T curves R114 and R245fa almost overlap each other based on Fig. 1, the thermodynamic effect in the cavitation of R245fa should be equivalent to that in the cavitation of R114 in magnitude. The model constants F_{vap} and F_{con} obtained from the cavitating flows of R114 through the venturi in Section 3.1 are adopted. From Fig. 5, the relationship of the constants F_{vap} and F_{con} to Reynolds number Re reads as:

$$F_{vap} = F_{con} = 7.9659e^{-9.3241\times10^{-7}\mathrm{Re}} \tag{25}$$

where Re is the instant Reynolds number of the suction pipe in the diaphragm pump.

Table 8
Parameters of the diaphragm, valve and spring.

Item	Parameter	Value
Diaphragm	R_1(mm)	5.75
	R_2(mm)	15.75
	s(mm)	4.938
	n(rpm)	480
	Ω(rad/s)	50.26
Valve	M_v(kg)	0.0825
	d_h(mm)	14
	d_{v1}(mm)	18
	d_{v2}(mm)	21
	θ(°)	45
Spring	κ(N/m)	900
	h_0(mm)	−0.5

At the suction pipe inlet, a constant static pressure, temperature and turbulence intensity are prescribed, and the gradient of fluid flow variables is zero. A symmetrical boundary condition is

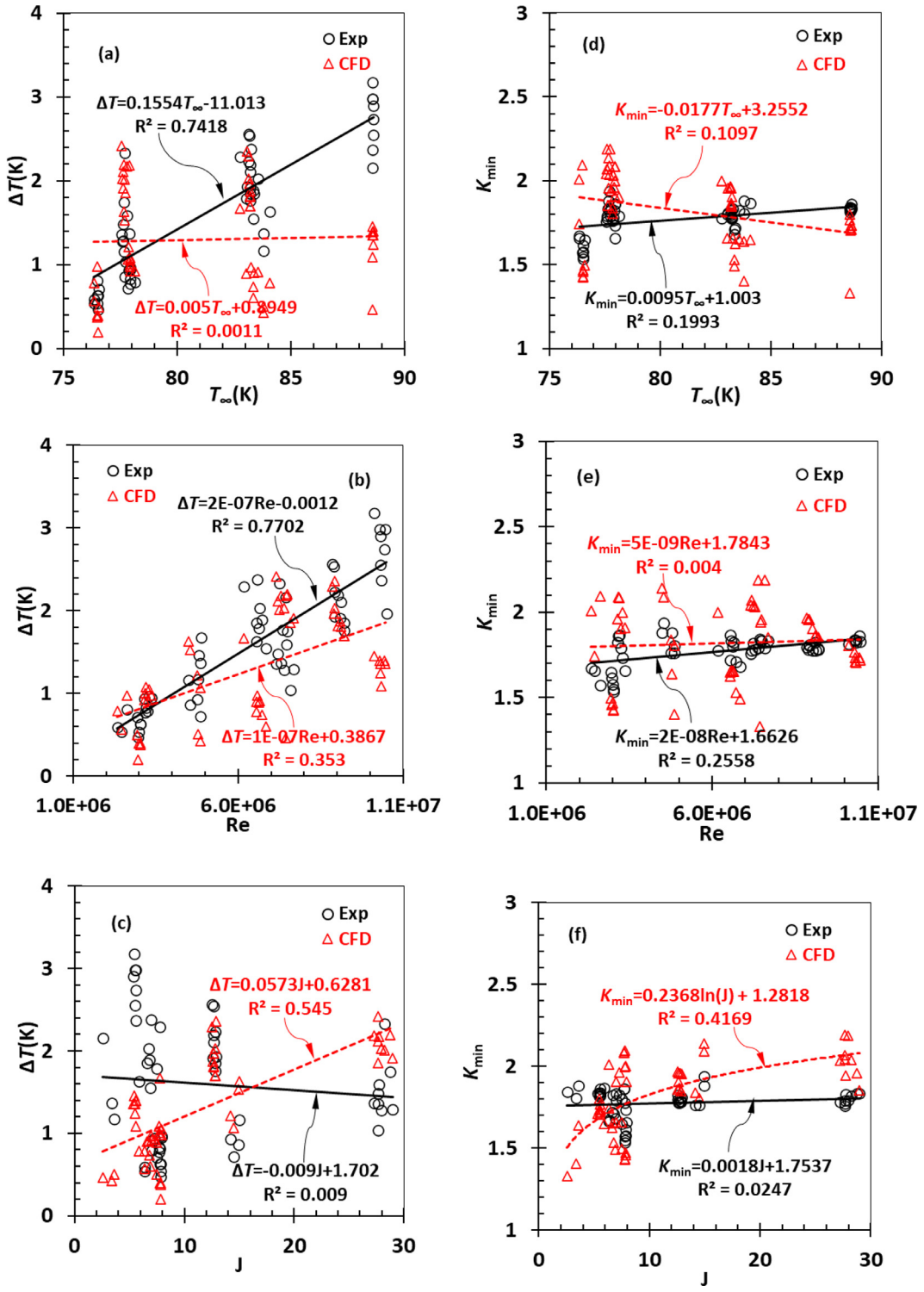

Fig. 11. Comparison of temperature depression ΔT and minimal cavitation number K_{min} between experiment and CFD prediction for LN2, the two parameters are in terms of bulk temperature T_∞, Reynolds number Re and Jakob number J, respectively.

held on the plane of symmetry of the pump. The diaphragm is adiabatic and subject to a moving boundary condition with a known axial displacement. The rest boundaries are adiabatic and no-slip smooth wall, and the scalable wall function is selected. A dynamic mesh is employed in the suction chamber and the pumping chamber fluid domains.

A mesh size independent mesh, which has 1205,436 elements, including 60,602,798(50.0%) wedge elements, 461,037(38.2%) tetrahedrons, 15,050(1.9%) hexahedrons, and 20,365(1.7%) pyramids, was achieved at 6.25 × 10^{-4} s time step [21]. This mesh was employed to simulate the cavitating flows of R245fa in the suction stroke.

A series of CFD simulations was conducted at inlet pressures ranged in 82–141 kPa, the mean flow rate Q was determined, and Q-NPSHa curve was established, and the curve is shown in Fig. 20, where the Q/Q_N-NPSHa curve is compared with those based on

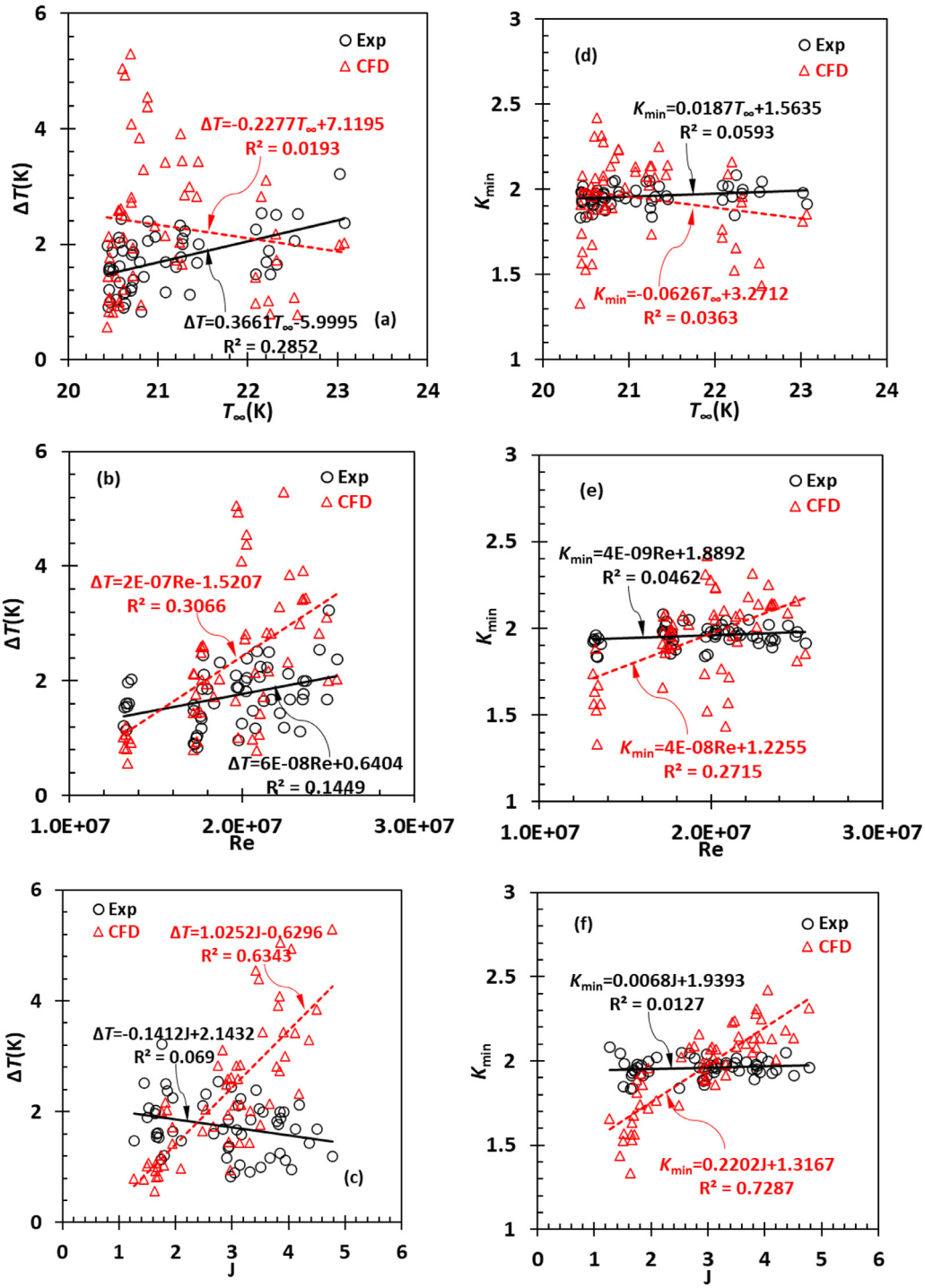

Fig. 12. Comparison of temperature depression ΔT and minimal cavitation number K_{min} between experiment and CFD prediction for LH2, the two parameters are in terms of bulk temperature T_∞, Reynolds number Re and Jakob number J, respectively.

the experimental data of R11 and R113 in the axial piston pump operating at 2000 r/min rotational speed and 60 °C bulk temperature in [11], Q_N is the mean flow rate without cavitation.

According to Fig. 20, the present cavitation model has successfully predicted a Q-NPSHa curve compared with the ZGB model with validated constants F_{vap} and F_{con} by using the cavitating flows in a venturi [21]. Based on a criterion of 1% drop in Q, the NPSHr=0.457 m yields, which is smaller than NPSHr=2.02 m estimated based on the datasheet issued by the manufacturer of the diaphragm pump and the correction of thermodynamic effect reported in [19]. The Q/Q_N-NPSHa curve predicted is similar in shape to those obtained by experiment on the axial piston pump when delivering organic fluids R11 and R113, respectively, but drops quicker than the latter. Hence, further experimental tests are on demand to validate NPSHr predicted and ensure the suitability of the proposed model in more general.

Maximal vapour volume fraction α_{max}, maximal temperature depression $\Delta T_{\max}$, minimal pressure p_{min} on the seat and valve, valve opening h and velocity V, force f on the valve and instant flow rate q through the gap between the seat and the valve are

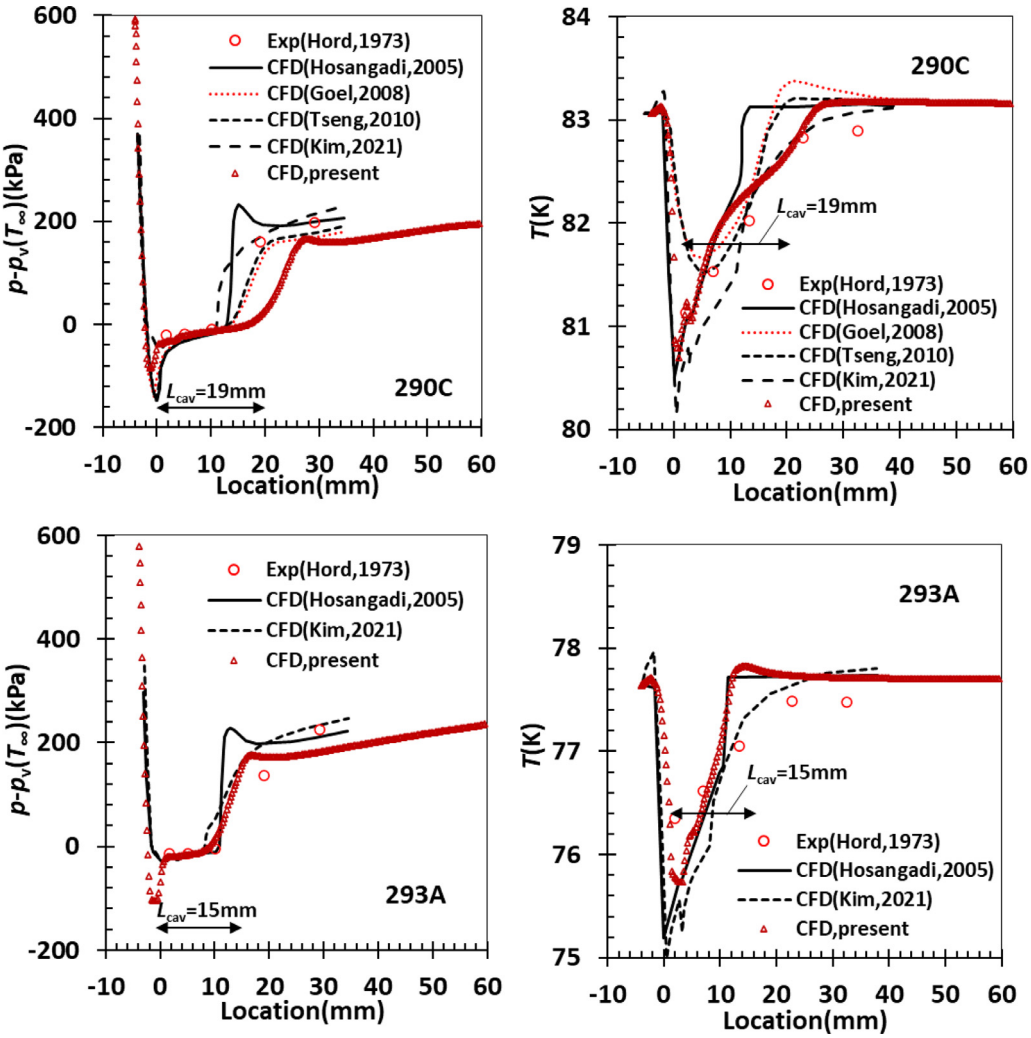

Fig. 13. Pressure difference p-$p_v(T_\infty)$ and liquid temperature T profiles of LN2 on the tapered hydrofoil wall predicted with the present cavitation model and the other models are compared with the experimental data for Case 20(290C) and Case 30(293A) in Table 5, the experimental data after [25], the data of Hosangadi (2005), Goel(2008), Tseng(2010), Kim(2021) after [54–57], respectively.

illustrated as a function of the crank rotating angle φ at the inlet pressures p_1=86, 85.2, 84, 82.25 kPa in Fig. 21. Those pressures correspond to NPSHa=0.734, 0.675, 0.587, 0.457 m. Based on the α_{max} profiles, cavitation emerges at first on the seat only at p_1=86, 85.2 kPa and achieves the peak at φ=102°. Then cavitation develops on both the seat and the valve body at the reduced inlet pressure p_1=84 kPa, and the peaks reach as early as φ=92°. The cavitation is fully developed on both the seat and the valve at p_1=82.25 kPa and α_{max} remains roughly constant at $\varphi \geq 75°$

Since $\Delta T_{\max}$ is proportional to α_{max}, the $\Delta T_{\max}$ profiles resemble the α_{max} profiles in shape. Under the critical cavitation condition (p_1=82.25 kPa), the ΔT_{max} peak value is as high as 0.45 K. The minimal pressures p_{min} on the seat and valve are below the vapour pressure $p_v(T_\infty)$ at far field or bulk temperature in a range of φ, the size of the range depending on p_1. This effect is attributed to pressure depression. The valve opening h, velocity V, force f acting on the valve, and instant flow rate q through the gap between the seat and the valve profiles are not influenced until p_1>84 kPa.

According to the α_{max} and p_{min} curves, expansion cavitation seems to occur at φ=12°, and then flow-induced cavitation happens at φ=60°, depending on p_1, and the lower the pressure the smaller the crank angle.

Cavity shape and location are illustrated in Fig. 22 at p_1=86, 85.2, 84, 82.25 kPa, and φ=106.2° A sheet cavity always exists on the seat at $p_1 \leq$86 kPa, however, another sheet cavity occurs on the valve body as $p_1 \leq$84 kPa. That cavity gets enlarged progressively with decreasing p_1, as a result, the sheet cavity covers the whole valve body and sheds a ring of cavity at p_1=82.25 kPa.

5. Discussion

A cavitation model with thermodynamic effect in the whole cavitation regime is cast in Section 2, the model is validated with three different kinds of cavitating flows, such as organic fluid R114 flowing in a venturi, LN2 and LH2 flowing around a tapered hydrofoil, water over a NACA 0015 hydrofoil in cavitation tunnels, finally the model is applied to simulate cavitating flows of organic fluid R245fa in a diaphragm pump in suction stroke by using calibrated model constants. The model has not been documented in the literature so far and can serve as a framework for cavitation modelling with thermodynamic effect.

The present cavitation model differs from the existing cavitation models proposed in [52–54], respectively, and is suitable for different cavitation regimes such as inertia-controlled, intermediate and superheat-controlled regimes intrinsically. For example, the cavitation model in [52,53] switches the vapour bubble growth rate in inertia-controlled regime to the growth rate in superheat-controlled regime at a time point. The cavitation model

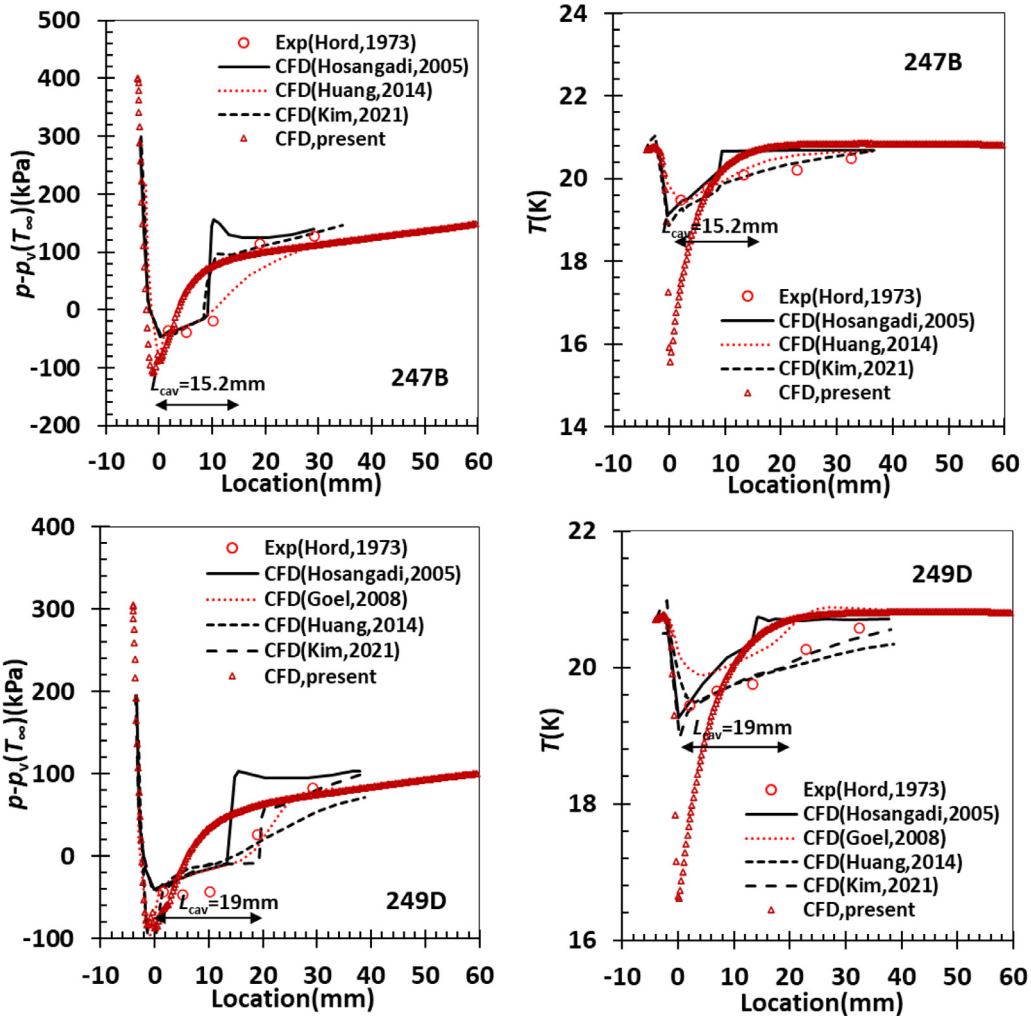

Fig. 14. Pressure difference p-$p_v(T_\infty)$ and liquid temperature T profiles of LH2 on the tapered hydrofoil wall predicted with the present cavitation model and the other models are compared with the experimental data for Case 19(247B) and Case 25(249D) in Table 5, the experimental data after [25], the data of Hosangadi (2005), Goel(2008), Huang(2014), Kim(2021) after [54–56,58], respectively.

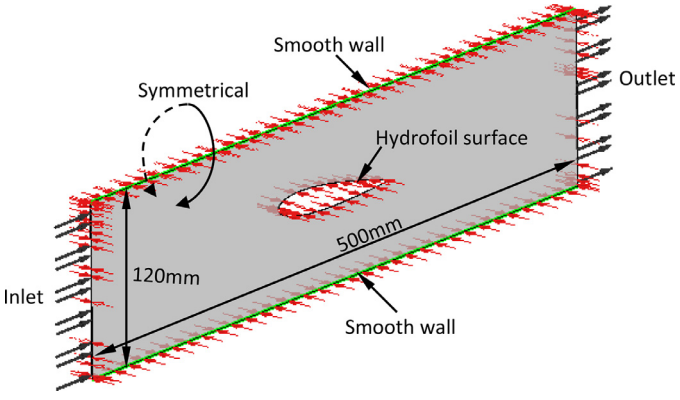

Fig. 15. Fluid domain of the cavitating flow around the NACA 0015 hydrofoil in a cavitation tunnel, the dimensions after [26].

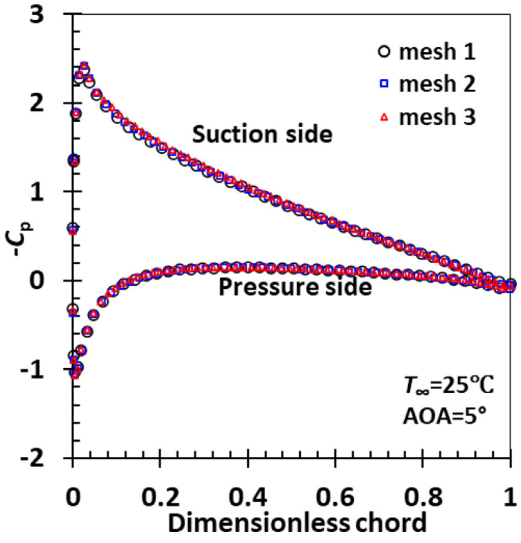

Fig. 16. Predicted pressures profiles $-C_p$ on the NACA 0015 hydrofoil surface at water bulk temperature T_∞=25 °C, and angle of attack AOA=5° under non-cavitation condition by using mesh 1, mesh 2 and mesh 3.

in [54] chooses the smallest rate from the vapour bubble growth rate in inertia-controlled regime and the growth rate in superheat-controlled regime as the bubble growth rate. The cavitation models do not provide the vapour bubble growth rate in intermediate cavitation regime. Additionally, an empirical temperature depression factor, i.e., B-factor, must be given in advance for a liquid with

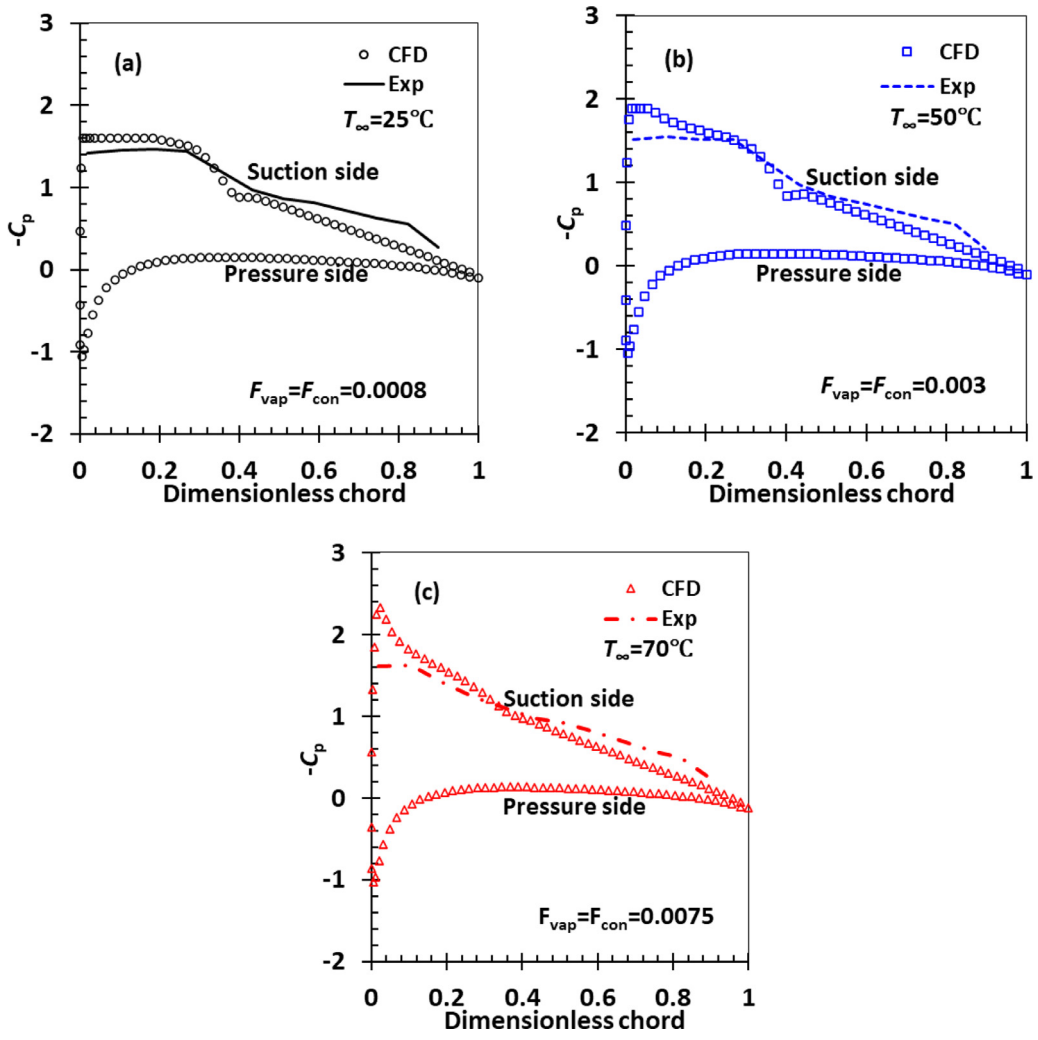

Fig. 17. Predicted pressures profiles $-C_p$ on the NACA 0015 hydrofoil surface are compared with the experimental data in [26] at water bulk temperature T_∞=25, 50, 70 °C, angle of attack AOA=5° and cavitation number K=1.5, (a) T_∞=25 °C, (b) T_∞= 50 °C, and (c) T_∞= 70 °C.

thermodynamic effect in cavitation. The present cavitation model does not need information on the temperature depression of a liquid during cavitation in advance.

Based on Fig. 20, the present cavitation model predicts the Q-NPSHa or Q/Q_N-NPSHa curve properly and the NPSHr of the diaphragm pump is determined by using the criterion of 1% drop in mean flow rate. The vapour bubble number density N is responsible for this result. According to Eqs. (4)–(6) the N depends on the far field pressure p_∞ and liquid surface tension for given a far field temperature and ppm of air. Specially, the higher the p_∞, the larger the N or vice versa. For a given F_{vap} and F_{con}, a smaller N means a lower vapour volume fraction α to prevent the CFX solver from crashing. However, the ZGB cavitation model with updated F_{vap} and F_{con} [21] is subjected to a fixed N, causing a rapid increase in α with decreasing p_∞, and prompting the solver to crash.

The vapour bubble number density or cavitation nuclei number density N profiles are plotted as a function of far field pressure p_∞ or inlet pressure p_1 in Fig. 23, when CFD simulations of cavitating flows were performed for R245fa in the suction stroke of the diaphragm pump, R114 through the venturi, LN2 and LH2 around the tapered hydrofoil and water over the NACA 0015 hydrofoil in cavitation tunnels. These cavitation nuclei number densities are calculated in terms of 140 ppm air concentration for R245a, R114, LN2 and LH2 but 22 ppm for water. Clearly, N depends on p_∞ or p_1. For R245fa, N declines to 2.5 × 10^{14} m $^{-3}$ from 1.9 × 10^{17} m $^{=3}$ with decreasing p_1. N varies in 6 × 10^{18}–4 × 10^{20} m $^{-3}$, 8.2 × 10^{16}–8.7 × 10^{19}m^{-3} and 2 × 10^{18}–3.5 × 10^{19} m $^{-3}$ for LH2, LN2 and R114, respectively. For water, however, N decreases as small as 7.3 × 10^{14}–4.8 × 10^{15}m^{-3}. However, the predicted Q-NPSHa or Q/Q_N-NPSHa curve and cavitation nuclei number density N profiles here need experimental confirmation in the future.

An existence of flow turbulence can lead to a sever fluctuation of fluid static pressure which is prone to cavitation occurrence [59]. The fluid real pressure p_{real} should be written as:

$$p_{real} = p - p_{turb} \tag{26}$$

where p_{turb} is the pressure fluctuation due to turbulence, and related to local turbulent kinetic energy k and density of liquid-vapour mixture ρ, $p_{turb} = 0.39\rho k/2$ for isotropic turbulence [59]. Replacing the static pressure in Eq. (19) with p_{real} in Eq. (26), the source terms m_{vap} and m_{con} are rewritten as:

$$\begin{cases} m_{vap} = F_{vap}(4\pi N)^{1/3}(3\alpha)^{2/3}(1-\alpha)^{4/3}\frac{\rho_l\rho_v}{\rho}A \\ \quad \times\left(\sqrt{\left(\frac{p_v(T)+p_{turb}-p}{NPSHa}+\frac{T_\infty-T_v}{\Delta T_{sub}}\right)+\frac{A^2}{B^2}t}-\sqrt{\frac{A^2}{B^2}t}\right) \\ m_{con} = -F_{con}(4\pi N)^{1/3}(3\alpha)^{2/3}(1-\alpha)^{4/3}\frac{\rho_l\rho_v}{\rho}A \\ \quad \times\left(\sqrt{\left(\frac{p-p_{turb}-p_v(T)}{NPSHa}+\frac{T_\infty-T_v}{\Delta T_{sub}}\right)+\frac{A^2}{B^2}t}-\sqrt{\frac{A^2}{B^2}t}\right) \end{cases} \tag{27}$$

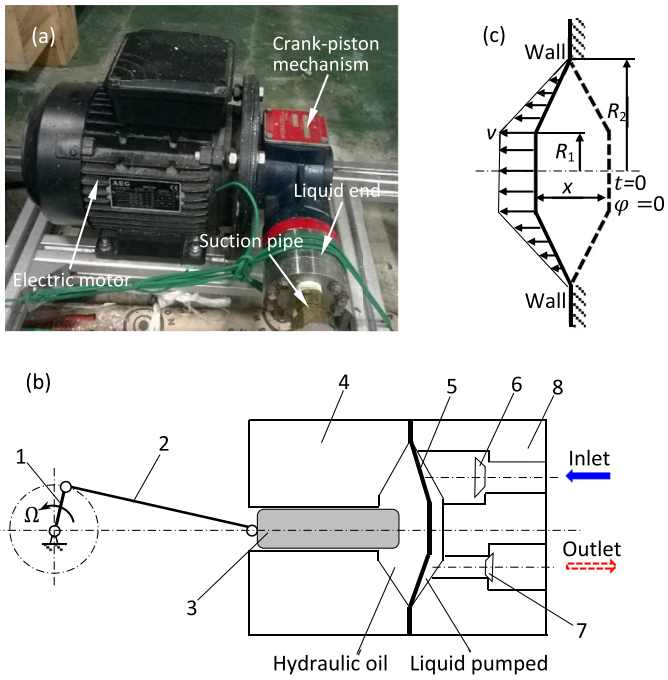

Fig. 18. Picture of the positive displacement diaphragm pump of G20-E model (a), a sketch of its crank-piston mechanism and liquid end in suction stroke (b), and idealised deformation of the diaphragm (c), 1-drive crank, 2-connecting rod, 3-piston, 4-piston casing, 5-diaphragm, 6-inlet valve, 7-discharge valve, 8-valve housing.

where Eq. (27) apparently suggests that the cavitation threshold $p_v(T)$ is increased to $p_{turb}+p_v(T)$. The cavitation model with Eq. (27) as the source terms has been tried, however, the effect of pressure fluctuation due to turbulence on cavity length is negligible because of quite low density ρ of the mixture in the cavity.

The negative root of Eq. (16) potentially can be used as the vapour bubble collapse rate to calculate the mass transfer rate from vapour to liquid m_{con} at $p_v(T) < p$. In that case, the collapse rate is written as:

$$-\frac{dR}{dt} = -A\left(\sqrt{\left(\frac{p-p_v(T)}{\mathrm{NPSHa}}+\frac{T_\infty - T_v}{\Delta T_{sub}}\right)+\frac{A^2}{B^2}t}+\sqrt{\frac{A^2}{B^2}t}\right),\ p_v(T) < p \tag{28}$$

The collapse rate $-dR/dt$ in the expression for m_{con} in Eq. (19) was replaced by Eq. (28), and 11 cases in Section 3.1 were relaunched, the responding results are tabulated in Table 9. Since the growth rate dR/dt remained unchanged when the collapse rate $-dR/dt$ was alternated, the value of constant F_{vap} in the cavitation model was fixed. The values of minimal cavitation number K_{min} and temperature depression ΔT predicted vary little when the collapse rate $-dR/dt$ was changed. The values of constant F_{con}, however, reduce greatly. For example, F_{con} determined with $-dR/dt$ in Eq. (28) is smaller by an order of 10^{-5}–10^{-9} than that determined with $-dR/dt$ in Eq. (18). This fact suggests that the magnitude of the collapse rate given by Eq. (28) is larger by an order of 10^5–10^9 than the growth rate in Eq. (17). Based on the experimental data on vapour bubble growth and collapse with thermodynamic effect in [60], the magnitude of the growth rate is nearly equal the magnitude of the collapse rate. The vapour bubble growth and collapse time-history curve predicted numerically in [61] suggests the magnitude of mean collapse rate is around five times the magnitude of mean growth rate. Obviously, the collapse rate given by Eq. (28), i.e., the negative root of Eq. (16) is too large in magnitude. Any-

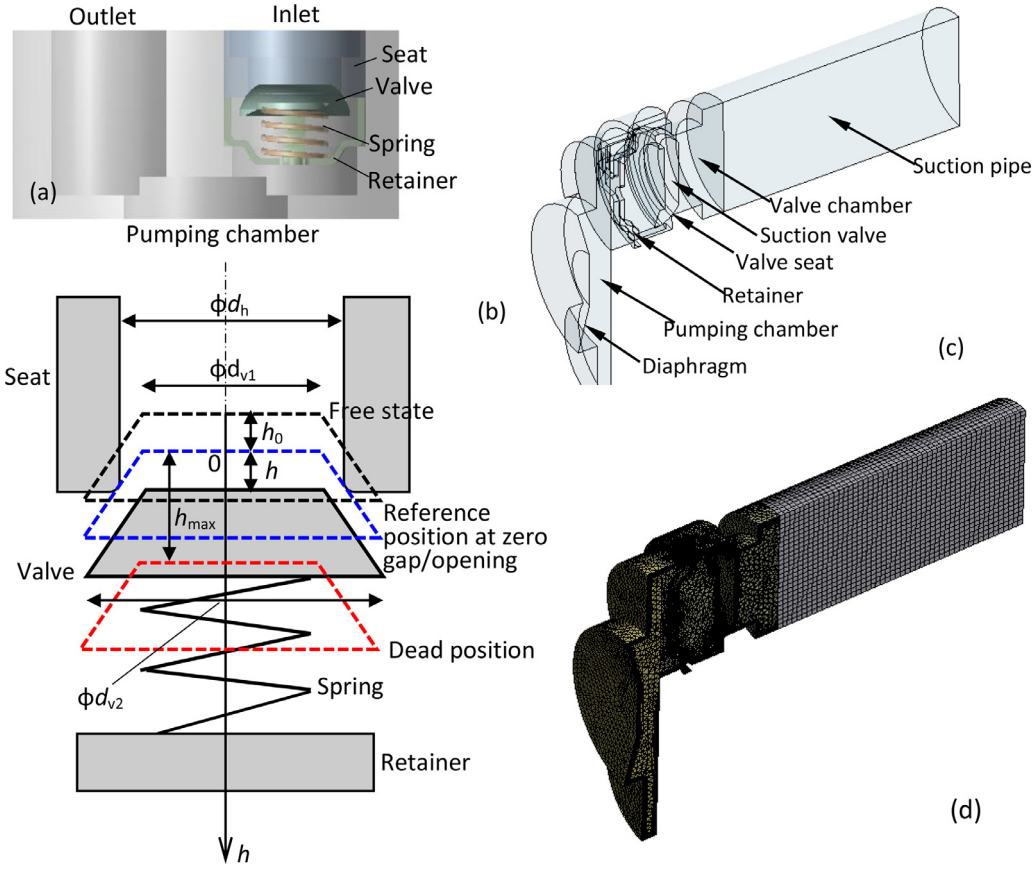

Fig. 19. Suction valve structure (a), the simplified mechanical model of the valve (b), the fluid domain for CFD simulations (c), and mesh in the fluid domains (d).

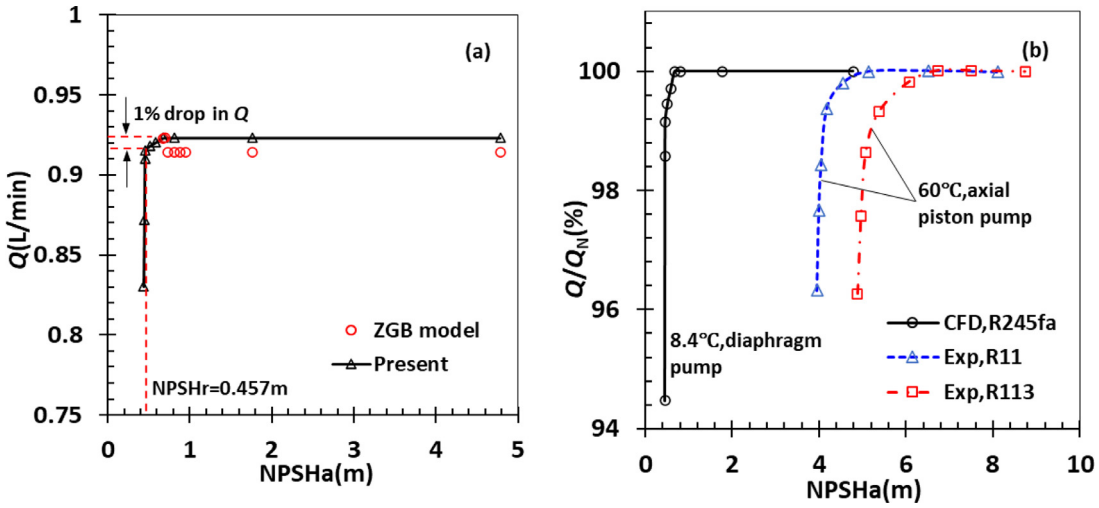

Fig. 20. Predicted Q-NPSHa curve of R245fa in the diaphragm pump (a), and predicted and experimental Q/Q_N-NPSHa curves of the diaphragm pump and axial piston pump, the experimental data from [11], where the axial piston pump at 2000 r/min rotational speed and 60 °C bulk temperature of R11 and R113, Q_N is the mean flow rate of the diaphragm pump under non-cavitation condition.

Table 9
Experimental data and CFD simulation results with different vapour bubble collapse rates for R114 cavitating flow in a venturi.

Case	Experimental data [24]		CFD simulation							
			$-dR/dt$ in Eq. (18)				$-dR/dt$ in Eq. (28)			
	K_{min}	ΔT (K)	F_{vap}	F_{con}	K_{min}	ΔT (K)	F_{vap}	F_{con}	K_{min}	ΔT (K)
1	2.39	1.50	4.4315	4.4315	2.59	1.51	4.4315	5.5000E-8	2.62	1.50
2	2.42	1.83	8.8500	8.8500	2.63	1.65	8.8500	7.5000E-8	2.64	1.63
3	2.43	2.78	4.3000	4.3000	3.17	0.39	4.3000	5.0000E-9	3.06	0.92
4	2.40	2.83	0.9260	0.9260	2.71	2.39	0.9260	4.5000E-8	2.74	2.22
5	2.40	3.00	2.2400	2.2400	2.70	2.26	2.2400	2.0000E-8	2.71	1.97
6	2.37	4.06	1.0000	1.0000	3.12	1.04	1.0000	6.0000E-8	3.09	0.99
7	2.43	4.06	0.9600	0.9600	2.75	2.72	0.9600	1.1500E-8	2.76	2.57
8	2.41	5.06	2.8000	2.8000	2.74	2.32	2.8000	8.1000E-9	2.74	2.25
9	2.49	2.17	0.8500	0.8500	3.14	0.87	0.8500	1.4850E-6	3.11	0.91
10	2.39	3.50	0.8300	0.8300	3.14	0.91	0.8300	9.6000E-8	3.10	0.94
11	2.39	4.44	2.8000	2.8000	2.80	4.00	2.8000	7.5000E-9	2.76	3.91

way, this issue needs to be clarified with more experimental data and analytical results in the future.

The time t in the cavitation model, Eq. (19) is replaced with reference time t_{ref}, which is the characteristic time of a flowing system/device. Usually, the time for cavitation taking place should be shorter than t_{ref}. However, it is challenging to decide that time and its profile when cavitation in a steady flow is simulated. How to validate the model with an unsteady flow model for the steady flow in t_{ref} scale is also important. For an unsteady cavitating flow, whether the instant time of the flow can be used in Eq. (19) as the time for cavitating is unclear. Those issues need to be clarified in the future.

When the vapour bubble number density is being determined, a few assumptions have to be made, namely, the vapour bubble number density is equal to the non-condensable gas/air number density in the liquid, the non-condensable gas/air bubbles are spherical and in uniform size, their partial pressure is ignored, and the non-condensable gas/air bubbles are not included in the cavitation model as an additional phase component. These assumptions require to be dismissed in the future by further understanding the cavitation phenomena occurred in different systems. Additionally, the determination of vapour bubble number density in the paper belongs to the simplest nucleation model, i.e., homogeneous seeding nucleation [62], and more complicated nucleation models are worth being tried in the future.

The model constants F_{vap} and F_{con} were decided by matching the predicted cavity length to the cavity length observed in terms of the bisection method in the present paper. As a result, the predicted wall pressure and temperature profiles may not match the profiles measured exactly. The optimization [63–65] and machine learning [66] methods are worth being attempted based on an objective function composed of experimental and predicted pressures, temperatures and cavity lengths in the future.

Compared with the existing cavitation models without thermodynamic effect, the present cavitation model requests more the thermophysical and transport properties of liquid and vapour, such as liquid and vapour densities ρ_l, ρ_v, specific heat capacities c_{pl}, c_{pv}, dynamic viscosities μ_l, μ_v, thermal conductivities λ_l, λ_v, saturated vapour pressure p_v and saturated vapour temperature T_v, latent heat $\mathscr{L}$, thermal diffusivity $\mathscr{D}$, and maximal liquid-vapour-density-ratio $(\rho_l/\rho_v)_{max}$ and surface tension γ. This implies that the possible impact of the thermophysical and transport properties have been well accounted. However, a longer time and more effort are on demand to set up a proper problem for the solver in ANSYS CFX.

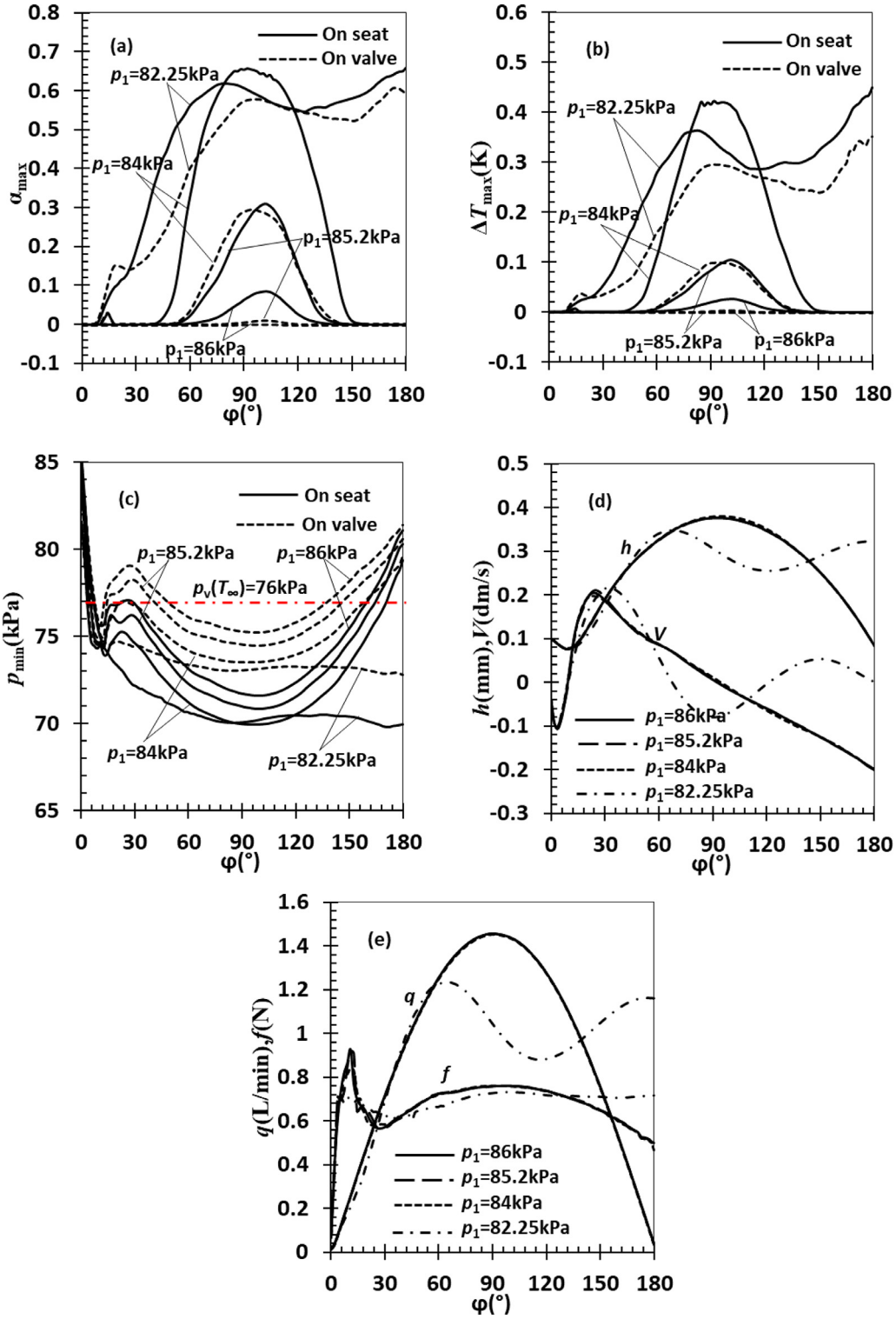

Fig. 21. Maximal vapour volume fraction α_{max} (a), maximal temperature depression ΔT_{max} (b), minimal pressures p_{min} on the seat and valve (c), valve opening h and velocity V (d), force f on the valve and instant flow rate q through the gap between the seat and the valve (e), are plotted as a function of the crank rotating angle φ at the inlet pressures p_1=86, 85.2, 84, 82.25 kPa.

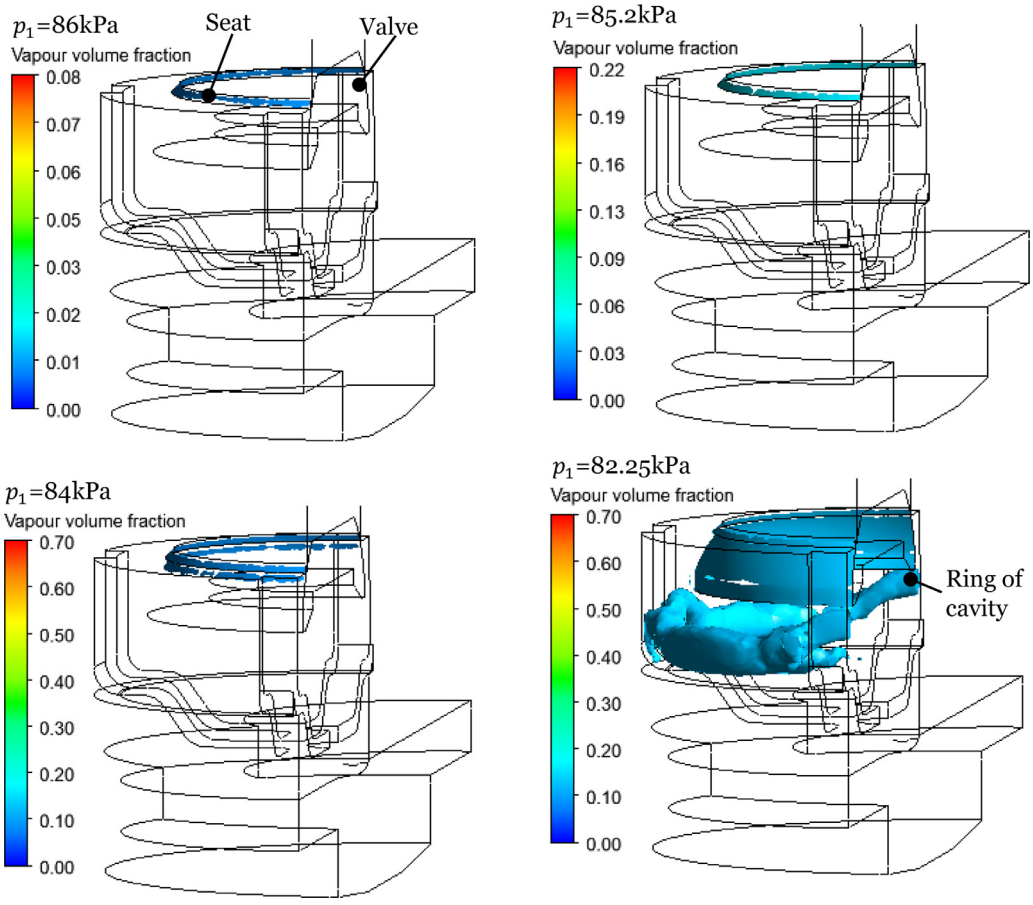

Fig. 22. Appearances of the cavities on the seat and valve body at p_1=86,85.2,84,82.25 kPa, and φ=106.2°.

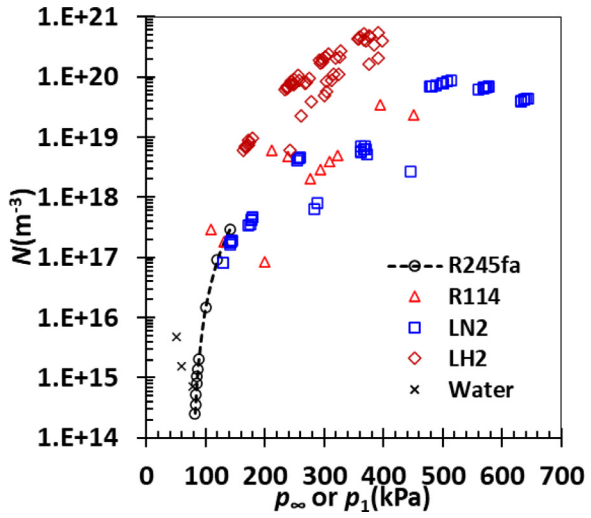

Fig. 23. Vapour bubble number density N profiles against far field pressure p_∞ or inlet pressure p_1 in CFD simulations of cavitating flows for R245fa in suction stroke of the diaphragm pump, cavitating flows of R114 in the venturi, LN2 and LH2 over the tapered hydrofoil and water around the NACA 0115 hydrofoil in cavitation tunnels.

6. Conclusion

A new cavitation model with thermodynamic effect was derived in detail. The model includes two key elements: vapour bubble growth rate and vapour bubble number density. Surface tension-controlled regime was considered in the determination of vapour bubble number density, i.e., cavitation nuclei number density based on a known air or non-condensable gas concentration in ppm in a liquid. Inertia-controlled, intermediate and heat transfer-controlled regimes were taken into account in vapour bubble growth rate. The cavitation model was embedded in ANSYS CFX as user defined model. The model was validated by using cavitating flows of organic fluid R114 (11 cases) in a venturi, liquid nitrogen (54 cases) and liquid hydrogen (55 cases) over a tapered hydrofoil and warm water (3 cases) around a hydrofoil NACA 0015 in cavitation tunnels in terms of cavity length observed. The model was employed in simulations of unsteady cavitating flows of organic fluid R245fa in a diaphragm pump based on the two model constants calibrated with organic fluid R114. It was conformed that: (1) the cavitation model here is feasible to the cavitation in liquid nitrogen and hydrogen with the strongest thermodynamic effect, organic fluids R114 and R245fa with moderate thermodynamic effect, and warm water with slight thermodynamic effect, respectively; (2) the thermodynamic effect was underestimated with the model by 43% for R114, 18.6% for liquid nitrogen and 32.6% for liquid hydrogen based on temperature depression or by 18% for R114, 2.5% for liquid nitrogen, 0.5% for liquid hydrogen based on minimal cavitation number; (3) two model constants F_{vap} and F_{con} can be correlated to Reynolds number; (4) the correlations of temperature depression and minimal cavitation number to bulk

liquid temperature, Reynolds number and Jakob number are inconsistent across R114, liquid nitrogen and liquid hydrogen; (5) the predicted temperature or pressure profiles on hydrofoil surface are in reasonable good agreement for liquid nitrogen and warm water, but poor for liquid hydrogen; (6) the cavitation model can capture an expected curve of mean pump flow rate against net positive suction head available, i.e. the flow rate declines with decreasing net positive suction head available, in turn, the net positive suction head can be determined with that curve.

Frankly, the present cavitation model requires refinements in the future, for example, two model constants F_{vap} and F_{con} are optimized by using advanced optimization methods in terms of temperature, pressure profiles and cavity length, and the model is validated with unsteady cavitating flows, how the time profile in the model influences the prediction behaviour of the model and so forth.

Declaration of Competing Interest

The authors declare that they have no known competing financial interests or personal relationships that could have appeared to influence the work reported in this paper.

CRediT authorship contribution statement

Wenguang Li: Conceptualization, Investigation, Methodology, Formal analysis, Visualization, Writing – original draft. **Zhibin Yu:** Funding acquisition, Project administration, Writing – review & editing. **Sambhaji Kadam:** Methodology, Writing – review & editing.

Data availability

Data will be made available on request.

Acknowledgement

This research benefited from the financial support provided by EPSRC (EP/T022701/1, EP/V042033/1, EP/P028829/1, EP/N020472/1, EP/N005228/1, EP/V030515/1) in the UK.

Appendix A Governing equations of flow and source terms

A1 Homogeneous multiphase flow model

In ANSYS CFX, cavitating flow is treated as an incompressible homogeneous multiphase flow of a mixture of continuous liquid and its continuous vapour described in the Eulerian-Eulerian coordinate system. In the homogeneous multiphase flow, all fluids share the common flow field including velocity, pressure, temperature and turbulence. The continuity equation, Reynolds-averaged Navier-Stokes equation and energy equation are given by [27]:

$$\frac{\partial(\alpha\rho_v)}{\partial t}+\nabla\cdot(\alpha\rho_v\boldsymbol{u})=m_{vap} \tag{A1}$$

$$\frac{\partial[(1-\alpha)\rho_l]}{\partial t}+\nabla\cdot[(1-\alpha)\rho_l\boldsymbol{u}]=m_{con} \tag{A2}$$

$$\frac{\partial(\rho\boldsymbol{u})}{\partial t}+\nabla\cdot\left(\rho\boldsymbol{u}\boldsymbol{u}^T\right)=\nabla p+\nabla\cdot\boldsymbol{\tau} \tag{A3}$$

$$\frac{\partial(\rho\hbar)}{\partial t}-\frac{\partial p}{\partial t}+\nabla\cdot(\rho\hbar\boldsymbol{u})=\nabla\cdot\left(\lambda\nabla T+\frac{\mu_t}{Pr_t}\nabla\hbar\right) \tag{A4}$$

where α is vapour volume fraction, ρ_v and ρ_l are vapour and liquid density; ρ is mixture density, $\rho=\alpha\rho_v+(1-\alpha)\rho_l$, m_{vap} and m_{con} are mass transfer rate per unit volume for vapour growth and condensation; $\boldsymbol{u}$ is velocity vector of the mixture, $\boldsymbol{u}^T$ is the transpose of $\boldsymbol{u}$, p is static pressure of the mixture, τ is stress tensor of the mixture, $\tau=(\mu+\mu_t)(\nabla\boldsymbol{u}+\nabla\boldsymbol{u}^T)-\frac{2}{3}(\mu+\mu_t)\nabla\cdot\boldsymbol{u}$, $\nabla\boldsymbol{u}^T$ is the transpose of $\nabla\boldsymbol{u}$, μ is dynamic viscosity of the mixture, $\mu=\alpha\mu_v+(1-\alpha)\mu_l$, μ_v and μ_l are dynamic viscosity of vapour and liquid; μ_t is eddy viscosity of turbulence, $\hbar$ is enthalpy of the mixture, λ is thermal conductivity of the mixture, $\lambda=\alpha\lambda_v+(1-\alpha)\lambda_l$, λ_v and λ_l are thermal conductivity of vapour and liquid; T is temperature of the mixture, Pr_t is turbulent Prandtl number, Pr_t=0.9.

The Wilcox k-ω turbulence model is usually applied to determine μ_t of cavitating flow with mild flow separation from a wall. The model consists of k-equation and ω-equation, as presented by [27]:

$$\frac{\partial(\rho k)}{\partial t}+\nabla\cdot(\rho k\boldsymbol{u})=\nabla\cdot\left[\left(\mu+\frac{\mu_t}{\sigma_1}\right)\nabla k\right]+P_k-\beta_1\rho k\omega \tag{A5}$$

$$\frac{\partial(\rho\omega)}{\partial t}+\nabla\cdot(\rho\omega\boldsymbol{u})=\nabla\cdot\left[\left(\mu+\frac{\mu_t}{\sigma_2}\right)\nabla\omega\right]+\beta_2\frac{\omega}{k}P_k-\beta_3\rho\omega^2 \tag{A6}$$

where k is turbulent kinetic of the mixture, ω is specific rate of k dissipation, $\mu_t=\rho k/\omega$, P_k is production rate of turbulence, $P_k=\tau\cdot\nabla u$, the model constants are $\sigma_1=\sigma_2=2$, β_1=0.09, β_2=5/9 and β_3=0.075.

A2 Source terms

The source terms m_{vap} and m_{con} in Eqs. (A1) and (A2) are expected to determine analytically by using a cavitation model in CFD simulations of cavitating flows. Classification of existing cavitation models for CFD simulations is detailed in Appendix B. Essentially, deterministic cavitation models are much more dominant than stochastic models. In deterministic cavitation models, the homogeneous multiphase mixture cavitation models are much more dominant than the interface tracking cavitation models and multiscale cavitation models. The Rayleigh-Plesset equation-based cavitation models significantly outweigh the equation-of-state, arbitrary mass transfer rate, evaporation and condensation, and nucleation cavitation models. The Schnerr-Sauer model and ZGB model are more commonly adopted in CFD simulations of cavitating flow.

The vapour bubbles are considered as individual spherical bubbles with radius R and bubble number density N in a unit volume, the vapour volume fraction α and its change rate with time $d\alpha/dt$ are expressed in terms of R and radius change rate dR/dt:

$$\begin{cases}\alpha=\frac{\frac{4}{3}\pi R^3N}{1+\frac{4}{3}\pi R^3N}\\ \frac{d\alpha}{dt}=\frac{3(1-\alpha)\alpha}{R}\frac{dR}{dt}\end{cases} \tag{A7}$$

The continuity equation of the vapour and liquid mixture can be obtained by adding Eqs. (A1) and (A2) together, and takes the following form:

$$\frac{\partial\rho}{\partial t}+\nabla\cdot(\rho\boldsymbol{u})=m_{vap}+m_{con}=0 \tag{A8}$$

where m_{con}=-m_{vap} should yield. The continuity equation in non-conservative form will be employed to formulate m_{vap} and m_{con}. Since the identity $\nabla\cdot(\rho\boldsymbol{u})=\boldsymbol{u}\cdot\nabla\rho+\rho\nabla\cdot\boldsymbol{u}$ and $\frac{\partial\rho}{\partial t}+\boldsymbol{u}\cdot\nabla\rho=\frac{d\rho}{dt}$ are held, the continuity equation in nonconservative form of Eq. (A8) is written as:

$$\frac{d\rho}{dt}+\rho\nabla\cdot\boldsymbol{u}=0 \tag{A9}$$

Based on Eq. (A9), obviously, the identity $\frac{d\rho}{dt}$=-$\rho\nabla\cdot u$ should yield, thus the velocity divergence is calculated by:

$$\nabla\cdot u=-\frac{1}{\rho}\frac{d\rho}{dt}=-\frac{1}{\rho}\frac{d[\alpha\rho_v+(1-\alpha)\rho_l]}{dt}=-\frac{(\rho_v-\rho_l)}{\rho}\frac{d\alpha}{dt} \tag{A10}$$

The vapour volume fraction transport equation is written as:

$$\frac{\partial \alpha}{\partial t}+\nabla\cdot(\alpha \boldsymbol{u})=\frac{d\alpha}{dt}+\alpha\nabla\cdot\boldsymbol{u}=\frac{d\alpha}{dt}-\alpha\frac{(\rho_v-\rho_l)}{\rho}\frac{d\alpha}{dt}=\frac{\rho_l}{\rho}\frac{d\alpha}{dt} \tag{A11}$$

Comparing Eqs. (A11) with (A1), the source terms in both the equations should satisfy the following relation:

$$\frac{1}{\rho_v}m_{vap}=\frac{\rho_l}{\rho}\frac{d\alpha}{dt} \tag{A12}$$

Thus, the source term for vapour bubble production should be written as:

$$m_{vap}=\frac{\rho_v\rho_l}{\rho}\frac{d\alpha}{dt} \tag{A13}$$

Similarly, the liquid volume fraction transport equation should read as:

$$\frac{\partial(1-\alpha)}{\partial t}+\nabla\cdot[(1-\alpha)\boldsymbol{u}]=\frac{d(1-\alpha)}{dt}+(1-\alpha)$$
$$\nabla\cdot\boldsymbol{u}=\frac{d(1-\alpha)}{dt}-(1-\alpha)\frac{(\rho_v-\rho_l)}{\rho}\frac{d\alpha}{dt}=-\frac{\rho_v}{\rho}\frac{d\alpha}{dt} \tag{A14}$$

Comparing Eqs. (A14) with (A2), the source terms in them should be linked by the relation:

$$\frac{1}{\rho_l}m_{con}=-\frac{\rho_v}{\rho}\frac{d\alpha}{dt} \tag{A15}$$

Naturally, the source term for vapour bubble destruction should be in the following form:

$$m_{con}=-\frac{\rho_l\rho_v}{\rho}\frac{d\alpha}{dt} \tag{A16}$$

Replacing $d\alpha/dt$ in Eqs. (A13) and (A16) with dR/dt in Eq. (A7), the source terms m_{vap} and m_{con} are expressed as:

$$\begin{cases} m_{vap}=\frac{3(1-\alpha)\alpha}{R}\frac{\rho_l\rho_v}{\rho}\frac{dR}{dt} \\ m_{con}=-\frac{3(1-\alpha)\alpha}{R}\frac{\rho_l-\rho_v}{\rho}\frac{dR}{dt} \end{cases} \tag{A17}$$

Based on Eq. (A7), the vapour bubble radius R can be expressed in terms of the vapour volume fraction α in Eq. (A17), namely:

$$R=\left[\frac{3\alpha}{4\pi N(1-\alpha)}\right]^{1/3} \tag{A18}$$

Replacing R with Eq. (A18), then, the source terms m_{vap} and m_{con} in Eq. (A17) are rewritten as:

$$\begin{cases} m_{vap}=(4\pi N)^{1/3}(3\alpha)^{2/3}(1-\alpha)^{4/3}\frac{\rho_l\rho_v}{\rho}\frac{dR}{dt} \\ m_{con}=-(4\pi N)^{1/3}(3\alpha)^{2/3}(1-\alpha)^{4/3}\frac{\rho_l\rho_v}{\rho}\frac{dR}{dt} \end{cases} \tag{A19}$$

Appendix B Classification of cavitation model and implantation of thermodynamic effect

Cavitation models used in CFD simulations are divided into deterministic models and stochastic models mathematically. The deterministic models include: (1) interface tracking models, (2) homogeneous two-phase mixture models, and (3) multiscale models based on their features in physics. The homogeneous two-phase mixture models have equation-of-state, arbitrary mass transfer rate, evaporation and condensation, Rayleigh-Plesset equation-based, and nucleation models. In the multiscale models, there are one-way and two-way coupling models. The detailed classification of cavitation models is illustrated in Table B1. The homogeneous two-phase mixture models compromise well between accuracy and computing time, thus have found the most extensive applications in CFD simulations. The multiscale cavitation models have increasingly been employed to predict the hydrodynamic behaviour of individual vapour bubbles and cavitation damage.

There are six methods for implementing thermodynamic effect in existing cavitation models. The first method is expressing the thermophysical properties such as liquid saturated pressure, liquid and vapour specific heats etc. as a function of liquid temperature, and the energy equation is employed for the liquid and vapour temperature. The second method is determining the local vapour pressure by the saturated pressure at far field temperature and pressure depression Δp. The B-factor is associated with vapour volume fraction and temperature depression ΔT separately. If the vapour volume fraction is known based on CFD simulations, then the B-factor can be determined, and ΔT is followed, finally, Δp will be decided with the known ΔT and $dp(T_\infty)/dT$. Obviously, the energy equation is not needed. The third method is determining vapour bubble radius in the cavitation model with the vapour bubble radius growth rate in [36]. In the fourth method, the vapour bubble growth rate calculated from inertia-controlled growth rate and the rate calculated from the heat diffusion-controlled growth rate given by [36] are summed to obtain a total growth rate. The thermophysical properties are expressed by liquid temperature explicitly. In the fifth method, the Bosnjakovic evaporation model [33] is combined with the Rayleigh-Plesset equation to lead to an updated Rayleigh-Plesset equation. Then, the vapour bubble growth rate is solved from the updated equation. The sixth method is related to multiple cavitation regime models. The vapour bubble growth rate is initially determined with the inertia-controlled growth rate, and with superheat-controlled growth rate in [36], the thermophysical properties are as a function of liquid temperature. The unique characteristics of those methods are demonstrated in Table B2. Note that Tables B1 and B2 have been appeared in [201]. However, they were updated with fresh references and some refinements, and it is worth being present once again.

Appendix C Thermophysical and transport properties of R114, LN2, LH2 and water

In the present cavitation model, the thermophysical and transport properties such as liquid and vapour densities ρ_l, ρ_v, specific heat capacities c_{pl}, c_{pv}, dynamic viscosities μ_l, μ_v, thermal conductivities λ_l, λ_v, saturated vapour pressure p_v and saturated vapour temperature T_v, latent heat $\mathscr{L}$, thermal diffusivity $\mathscr{D}$, and maximal liquid-vapour-density-ratio $(\rho_l/\rho_v)_{max}$ and surface tension γ are required. These properties in a range of temperature were extracted by using the software REFPROP and best fitted by employing mathematical expressions.

For R114, the following expressions in terms of far field liquid temperature T_∞ or local temperature T in 240–350 K are obtained:

$$\begin{cases} \rho_l=-3.7033\times10^{-3}T_\infty^2-0.8136T_\infty+2026.7\left(\mathrm{kg\ m^{-3}}\right) \\ \rho_v=4.0382\times10^{-4}T_\infty^3-0.27656T_\infty^2+64.131T_\infty-5025.2\left(\mathrm{kg\ m^{-3}}\right) \\ c_{pl}=2.4752T+276.76\ \left(\mathrm{J\ kg^{-1}K^{-1}}\right) \\ c_{pv}=0.95911T+388.95\ \left(\mathrm{J\ kg^{-1}K^{-1}}\right) \\ \mu_l=\exp(1111.1130/T_\infty-11.6942)\ \mathrm{(Pa.s)} \\ \mu_v=1.3088\times10^{-6}T_\infty-1.1182\times10^{-5}\ \mathrm{(Pa.s)} \\ \lambda_l=-2.8722\times10^{-4}T_\infty+15.045\ \left(\mathrm{W\ m^{-1}K^{-1}}\right) \\ \lambda_v=2.4060\times10^{-3}T_\infty-3.1439\times10^{-2}\ \left(\mathrm{W\ m^{-1}K^{-1}}\right) \\ p_v=4.0382\times10^{-4}T^3-2.7656\times10^{-1}T^2+64.131T-5025.2\ \mathrm{(kPa)} \\ T_v=10^{1.4091\times10^{-4}\lg^4 p+6.4459\times10^{-4}\lg^3 p+4.8223\times10^{-3}\lg^2 p+5.4838\times10^{-2}\lg p+2.3230}\ \mathrm{(K)} \\ \mathscr{L}=-3.5618\times10^{-4}T_\infty^2+3.149\times10^{-2}T_\infty+160.95\ \left(\mathrm{kJ\ kg^{-1}}\right) \\ \mathscr{D}=4.538\times10^{-13}T_\infty^2-5.2223\times10^{-10}T_\infty+1.5728\times10^{-7}\ \left(\mathrm{m^2\ s^{-1}}\right) \\ (\rho_l/\rho_v)_{max}=1.2259\times10^{28}T_\infty^{-0.10559} \\ \gamma=-1.2243\times10^{-4}T_\infty+4.8512\times10^{-2}\ \left(\mathrm{N\ m^{-1}}\right) \end{cases} \tag{C1}$$

where the unit of pressure p in T_v expression is kPa.

Table B1
Classification of existing cavitation models for CFD simulations.

Category				Thermodynamic effect	Source
Deterministic	Interface tracking			No	[67–71]
				Yes	[72,73]
	Homogeneous two-phase mixture	Equation-of-state models	Liquid-vapour thermodynamic variable table	Yes	[74–76]
			First-order differential equation of density	Yes	[77,78]
			Barotropic law curve without vapour volume fraction transport equation	No	[79–81]
			Sinusoidal barotropic law without vapour volume fraction transport equation	No	[82–84]
			Sinusoidal barotropic law with vapour volume fraction transport equation	No	[85,86]
				Yes	[87–89]
			Stiffened gas law without vapour volume fraction transport equation	No	[82]
				Yes	[90]
			Stiffened gas law with vapour volume fraction transport equation	Yes	[87,85,88,91]
			Gibbs free energy for phase mixture	No	[92]
		Arbitrary mass transfer rate models		No	[93–96]
				Yes	[55–57,97–101]
		Vapour-liquid interface evaporation and condensation model		No	[102–107]
				Yes	[108–110]
		Rayleigh-Plesset equation-based mass transfer rate model	Schnerr-Sauer model	No	[22,111–114]
				Yes	[115–121]
			Full cavitation model	No	[59]
				Yes	[122–127]
			ZGB model	No	[128]
				Yes	[58,129–141]
			Bubble-droplet model	No	[142]
			Mixture-liquid-density-ratio blended model	No	[143]
			Compressible cavitation model	No	[144]
			Multi-regime cavitation model	Yes	[52–54]
			Unified model	No	[145]
			Cavitation models with liquid viscosity	No	[146–148]
			Rankine vortex cavitation model	No	[149]
			Cavitation models with bubble-bubble interaction	No	[150,151]
			Cavitation models with bubble breakup in cavity cloud	No	[152,153]
			Cavitation models with first principal stress	No	[154–156]
			Polydisperse cavitation model based on population balances	No	[157]
		Nucleation cavitation models	Nuclei number density distribution of power function	No	[158,159]
			Nuclei number density distribution of exponential function	No	[160]
			Vapour nucleation theory with Rayleigh-Plesset equation	No	[161–165]
			Vapour nucleation theory with empirical function of nuclei number density distribution	No	[166]
			Vapour nucleation theory with existing simplified cavitation models in CFD package	Yes	[167,168]
	Multiscale	One-way coupling	Model for cavitation inception	No	[169–176]
			Fully developed cavitation model in still liquid	No	[177–182]
			Fully developed cavitation model in flowing liquid	No	[183–185]
			Euler-Lagrange sheet and bubble cavitation model	No	[186]
		Two-way coupling	Euler-Lagrange fully developed cavitation model	No	[187–198]
Stochastic	Stochastic cavitation inception model			No	[199]
	Stochastic field model			No	[200]

Table B2
Implementing methods for thermodynamic effect in cavitation models.

Method	Implementation	Source
Temperature-dependant thermal properties	1 Vapour pressure, liquid and vapour specific heats etc. are temperature-dependant. 2 Energy equation is solved for liquid and vapour temperature.	[21,55,57,97–101,115,116,119,124–126,136–139]
B-factor	1 Vapour pressure of liquid is corrected by using pressure depression Δp calculated by B-factor. 2 Energy equation of fluid flow should not be solved.	[123,134,135,54]
Vapour bubble radius determination	1 Vapour bubble radius is calculated with heat diffusion-controlled growth rate given by Plesset & Zwick [36]. 2 Thermophysical properties of liquid and vapour are temperature-dependant. 3 Energy equation is solved.	[108]
Vapour bubble growth rate correction	1 Inertia-controlled vapour bubble growth rate and heat diffusion-controlled rate given by Plesset & Zwick [36] is summed. 2 Thermophysical properties of liquid and vapour are temperature-dependant. 3 Energy equation is solved.	[120,129,130,58,132,140,141]
Combination of Bosnjakovic evaporation model and Rayleigh-Plesset equation	1 Bosnjakovic evaporation model and Rayleigh-Plesset equation are combined to obtain an updated Rayleigh-Plesset equation. 2 Solve the updated equation for vapour bubble growth rate.	[118,133,202,122,203]
Multiply cavitation regime	1 Vapour bubble growth rate is calculated under inertia-controlled condition, then under superheat-controlled condition. 2 Bosnjakovic evaporation model and Rayleigh-Plesset equation are combined.	[52–54]

For LN2, the best fitting mathematical expressions of the thermophysical and transport properties as a function of the far field temperature T_∞ or local temperature T in 70–120 K are written as:

$$\begin{cases}
\rho_l = -1.2624 \times 10^{-3}T_\infty^3 + 0.30316T_\infty^2 - 28.891T_\infty + 1810.3 \ \left(\text{kg m}^{-3}\right)\\
\rho_v = 10^{6.3706\times10^{-6}T_\infty^3 - 2.0729\times10^{-3}T_\infty^2 + 25.368T_\infty - 9.5056} \ \left(\text{kg m}^{-3}\right)\\
c_{pl} = 3.523236 \times 10^{-6}T^6 - 1.920779 \times 10^{-3}T^5 + 0.4344835T^4 - 52.17592T^3 + 3507.465T^2 - 125126T + 1852413 \ \left(\text{J kg}^{-1}\text{K}^{-1}\right)\\
c_{pv} = 5.74663 \times 10^{-6}T^6 - 3.134132 \times 10^{-3}T^5 + 0.70906T^4 - 85.162T^3 + 5725.05T^2 - 204229T + 3021031 \ \left(\text{J kg}^{-1}\text{K}^{-1}\right)\\
\mu_l = \left(6.396519 \times 10^{-9}T_\infty^6 - 4.24631 \times 10^{-4}T_\infty^5 + 1.171508 \times 10^{-3}T_\infty^4 - 0.1727801T_\infty^3 + 14.44786T_\infty^2 - 655.083T_\infty + 12801.41\right) \times 10^{-6} \ \text{(Pa.s)}\\
\mu_v = \left(1.037865 \times 10^{-6}T_\infty^4 - 3.596452 \times 10^{-4}T_\infty^3 + 4.6926 \times 10^{-2}T_\infty^2 - 2.646382T_\infty + 58.65586\right) \times 10^{-6} \ \text{(Pa.s)}\\
\lambda_l = -1.97028 \times 10^{-3}T_\infty + 0.2971848 \ \left(\text{W m}^{-1}\text{K}^{-1}\right)\\
\lambda_v = \left(8.315193 \times 10^{-9}T_\infty^6 - 4.506732 \times 10^{-6}T_\infty^5 + 1.014478 \times 10^{-3}T_\infty^4 - 0.1213125T_\infty^3 + 8.12451T_\infty^2 - 288.7534T_\infty + 4257.756\right) \times 10^{-3} \ \left(\text{W m}^{-1}\text{K}^{-1}\right)\\
p_v = 1.2790 \times 10^{-2}T^3 - 2.4739T^2 + 165.19T - 3791.9 \ \text{(kPa)}\\
T_v = 10^{\frac{-42.932+\sqrt{42.932^2-4\times(-8.984)\times[-50.03-\lg(p)]}}{2\times(-8.984)}} \ \text{(K)}\\
\mathscr{L} = -6.3243 \times 10^{-4}T_\infty^3 + 0.14748T_\infty^2 - 12.804T_\infty + 599.46 \ \left(\text{kJ kg}^{-1}\right)\\
\mathscr{D} = -2.137456 \times 10^{-13}T_\infty^3 + 4.690405 \times 10^{-11}T_\infty^2 - 4.354752 \times 10^{-9}T_\infty + 2.429862 \times 10^{-7} \ \left(\text{m}^2\ \text{s}^{-1}\right)\\
(\rho_l/\rho_v)_{max} = 10^{-7.6101\times10^{-6}T_\infty^3 + 2.3732\times10^{-3}T_\infty^2 - 0.28045T_\infty + 13.259}\\
\gamma = 9.118553 \times 10^{-7}T_\infty^2 - 3.739584 \times 10^{-4}T_\infty + 3.233882 \times 10^{-2} \ \left(\text{N m}^{-1}\right)
\end{cases} \tag{C2}$$

where the unit of pressure p in T_v expression is MPa.

For LH2, the best fitting mathematical expressions of the thermophysical and transport properties as a function of the far field temperature T_∞ or local temperature T in the range of 14–31 K read as:

$$\begin{cases}
\rho_l = -1.638 \times 10^{-5}T_\infty^6 + 2.1842 \times 10^{-3}T_\infty^5 - 0.11976T_\infty^4 + 3.452T_\infty^3 - 55.158T_\infty^2 + 462.29T_\infty - 1507.2 \ \left(\text{kg m}^{-3}\right)\\
\rho_v = 3.8023 \times 10^{-6}T_\infty^6 - 4.7861 \times 10^{-4}T_\infty^5 + 2.5823 \times 10^{-2}T_\infty^4 - 0.7205T_\infty^3 + 11.178T_\infty^2 - 91.353T_\infty + 307.12 \left(\text{kg m}^{-3}\right)\\
c_{pl} = 2.2762 \times 10^{-2}T^6 - 2.8834T^5 + 150.75T^4 - 4158.4T^3 + 63797T^2 - 51560T + 1719600 \ \left(\text{J kg}^{-1}\text{K}^{-1}\right)\\
c_{pv} = 3.1631 \times 10^{-2}T^6 - 3.9965T^5 + 208.32T^4 - 5727.7T^3 + 87550T^2 - 705040T + 2346400 \ \left(\text{J kg}^{-1}\text{K}^{-1}\right)\\
\mu_l = \left(-6.1102 \times 10^{-7}T_\infty^6 + 5.952 \times 10^{-5}T_\infty^5 - 1.7103 \times 10^{-3}T_\infty^4 - 1.0856 \times 10^{-2}T_\infty^3 + 1.536T_\infty^2 - 30.681T_\infty + 222.06\right) \times 10^{-6} \ \text{(Pa.s)}\\
\mu_v = \left(1.5529 \times 10^{-6}T_\infty^6 - 2.067 \times 10^{-4}T_\infty^5 + 1.1302 \times 10^{-2}T_\infty^4 - 0.32462T_\infty^3 + 5.1614T_\infty^2 - 42.988T_\infty + 146.93\right) \times 10^{-6} \ \text{(Pa.s)}\\
\lambda_l = \left(-1.909 \times 10^{-5}T_\infty^6 + 2.5627 \times 10^{-3}T_\infty^5 - 0.14213T_\infty^4 + 4.1774T_\infty^3 - 69.075T_\infty^2 + 616.29T_\infty - 2250.2\right) \times 10^{-3} \ \left(\text{W m}^{-1}\text{K}^{-1}\right)\\
\lambda_v = \left(2.49 \times 10^{-5}T_\infty^6 - 3.3096 \times 10^{-3}T_\infty^5 + 0.18075T_\infty^4 - 5.1861T_\infty^3 + 82.38T_\infty^2 - 685.63T_\infty + 2342.1\right) \times 10^{-3} \ \left(\text{W m}^{-1}\text{K}^{-1}\right)\\
p_v = 10^{-4.3677\lg^2(p) + 17.553\lg(p) - 16.491} \ \text{(MPa)}\\
T_v = 10^{\frac{-17.553+\sqrt{17.553^2-4\times(-4.3677)\times[-16.491-\lg(p)]}}{2\times(-4.3677)}} \ \text{(K)}\\
\mathscr{L} = -2.1138 \times 10^{-4}T_\infty^6 + 2.8169 \times 10^{-2}T_\infty^5 - 1.5437T_\infty^4 + 44.467T_\infty^3 - 710.08T_\infty^2 + 5961.7T_\infty - 20108 \ \left(\text{kJ kg}^{-1}\right)\\
\mathscr{D} = -3.9997 \times 10^{-12}T_\infty^4 + 3.7021 \times 10^{-10}T_\infty^3 - 1.3135 \times 10^{-8}T_\infty^2 + 2.0495 \times 10^{-7}T_\infty - 1.0155 \times 10^{-6} \ \left(\text{m}^2\ \text{s}^{-1}\right)\\
(\rho_l/\rho_v)_{max} = 3.788615 \times 10^{-4}T_\infty^6 - 5.62955 \times 10^{-2}T_\infty^5 + 3.462179T_\infty^4 - 112.8781T_\infty^3 + 2060.031T_\infty^2 - 19991.21T_\infty + 80847.49\\
\gamma = 6.704 \times 10^{-7}T_\infty^2 - 1.8925 \times 10^{-4}T_\infty + 5.5173 \times 10^{-3} \ \left(\text{N m}^{-1}\right)
\end{cases} \tag{C3}$$

where the unit of pressure p in T_v expression is MPa.

For water, the best fitting mathematical expressions of the thermophysical and transport properties as a function of the far field temperature T_∞ or local temperature T in 280–380 K are given by:

$$\begin{cases}
\rho_l = -3.23286 \times 10^{-3}T_\infty^2 + 1.65639T_\infty + 790.251 \ \left(\text{kg m}^{-3}\right)\\
\rho_v = 4.63451 \times 10^{-9}T_\infty^4 - 5.16982 \times 10^{-6}T_\infty^3 + 2.18412 \times 10^{-3}T_\infty^2 - 0.41371T_\infty + 29.6134 \ \left(\text{kg m}^{-3}\right)\\
c_{pl} = -2.16986 \times 10^{-8}T^5 + 3.76071 \times 10^{-5}T^4 - 2.60199 \times 10^{-2}T^3 + 8.99207T^2 - 1552.97T + 111433 \ \left(\text{J kg}^{-1}\text{K}^{-1}\right)\\
c_{pv} = 1.30956 \times 10^{-4}T^3 - 0.11307T^2 + 33.6996T - 1555.08 \ \left(\text{J kg}^{-1}\text{K}^{-1}\right)\\
\mu_l = \left(-2.33586 \times 10^{-7}T_\infty^5 + 4.05574 \times 10^{-4}T_\infty^4 - 0.282008T_\infty^3 + 98.2216T_\infty^2 - 17151.6T_\infty + 1203080\right) \times 10^{-6} \ \text{(Pa.s)}\\
\mu_v = \left(2.40571 \times 10^{-5}T_\infty^2 + 1.75828 \times 10^{-2}T_\infty + 2.32433\right) \times 10^{-6} \ \text{(Pa.s)}\\
\lambda_l = 4.49099 \times 10^{-10}T_\infty^4 - 5.82915 \times 10^{-7}T_\infty^3 + 2.73053 \times 10^{-4}T_\infty^2 - 5.32853 \times 10^{-2}T_\infty + 4.12217 \ \left(\text{W m}^{-1}\text{K}^{-1}\right)\\
\lambda_v = 2.94106 \times 10^{-7}T_\infty^2 - 1.10151 \times 10^{-4}T_\infty + 2.5242 \times 10^{-2} \ \left(\text{W m}^{-1}\text{K}^{-1}\right)\\
p_v = 10^{-23.4418\lg^2(T) + 133.742\lg(T) - 189.906} \ \text{(MPa)}\\
T_v = 10^{\frac{-133.742+\sqrt{133.742^2-4\times(-23.4418)\times[-189.906-\lg(p)]}}{2\times(-23.4418)}} \ \text{(K)}\\
\mathscr{L} = -2.45319T_\infty + 3173.54 \ \left(\text{kJ kg}^{-1}\right)\\
\mathscr{D} = 2.0845 \times 10^{-12}T_\infty^2 + 1.69825 \times 10^{-9}T_\infty - 1.75403 \times 10^{-7} \ \left(\text{m}^2\text{s}^{-1}\right)\\
(\rho_l/\rho_v)_{max} = 1.03231 \times 10^{-6}T_\infty^6 - 2.1267 \times 10^{-3}T_\infty^5 + 1.82512T_\infty^4 - 835.293T_\infty^3 + 215053T_\infty^2 - 29537500T_\infty + 1691300000\\
\gamma = -2.60968 \times 10^{-7}T_\infty^2 + 1.06317 \times 10^{-6}T_\infty + 9.48496 \times 10^{-2} \ \left(\text{N m}^{-1}\right)
\end{cases} \tag{C4}$$

where the unit of pressure p in T_v expression is MPa.

References

[1] P. Colonna, E. Casati, C. Trapp, T. Mathijssen, J. Larjola, T. Turunen-Saaresti, A. Uusitalo, Organic Rankine cycle power systems: from the concept to current technology, applications, and an outlook to the future, ASME J. Eng. Gas Turbines Power 137 (10) (2015) 100801.

[2] B.S. Park, M. Usman, M. Imran, A. Pesyridis, Review of organic Rankine cycle experimental data trends, Energy Convers. Manag. 173 (2018) 679–691.

[3] M. Imran, M. Usman, B.S. Park, H.J. Kim, D.H. Lee, Multi-objective optimization of evaporator of organic Rankine cycle (ORC) for low temperature geothermal heat source, Appl. Therm. Eng. 80 (2015) 1–9.

[4] K. Rahbar, S. Mahmoud, R.K. Al-Dadah, N. Moazami, Modelling and optimization of organic Rankine cycle based on a small-scale radial inflow turbine, Energy Convers. Manag. 91 (2015) 186–198.

[5] E.S. Richardson, Thermodynamic performance of new thermofluidic feed pumps for organic Rankine cycle applications, Appl. Energy 161 (2016) 75–84.

[6] G. Shu, Z. Yu, P. Liu, Z. Xu, R. Sun, Potential of a thermofluidic feed pump on performance improvement of the dual-loop Rankine cycle using for engine waste heat recovery, Energy Convers. Manag. 171 (2018) 1150–1162.

[7] Y.X. Yang, H.G. Zhang, Y.H. Xu, F. Yang, Y. Wu, B. Lei, Matching and operating characteristics of working fluid pumps with organic Rankine cycle system, Appl. Therm. Eng. 142 (2018) 622–631.

[8] Y.X. Yang, H.G. Zhang, G.H. Tian, Y. Xu, C. Wang, J. Gao, Performance analysis of a multistage centrifugal pump used in an organic Rankine cycle (ORC) system under various condensation conditions, J. Therm. Sci. 28 (4) (2019) 621–634.

[9] X. Wang, Y.Q. Feng, T.C. Hung, Z.X. He, C.H. Lin, M. Sultan, Investigating the system behaviors of a 10 kW organic Rankine cycle (ORC) prototype using plunger pump and centrifugal pump, Energies 13 (5) (2020) 1141.

[10] T.Z. Kaczmarczyk, G. Żywica, E. Ihnatowicz, Experimental investigation on a rotodynamic pump operating in the cogeneration system with a low-boiling working medium, Trans. Inst. Fluid-Flow Mach. 134 (2016) 63–87.

[11] E. Bollina, Head-flow and npsh performance of an axial piston pump working with organic fluids at different temperatures, Int. J. Heat Fluid Flow 5 (2) (1984) 93–100.

[12] E.J. Bala, P.W. O'Callaghan, S.D. Probert, Influence of organic working fluids on the performance of a positive-displacement pump with sliding vanes, Appl. Energy 20 (1985) 153–159.

[13] G. Bianchi, F. Fatigati, S. Murgia, R. Cipollone, G. Contaldi, Modeling and experimental activities on a small-scale sliding vane pump for ORC-based waste heat recovery applications, Energy Procedia 101 (2016) 1240–1247.

[14] J.C. Chang, T.C. Hung, Y.L. He, W.P. Zhang, Experimental study on low-temperature organic Rankine cycle utilizing scroll type expander, Appl. Energy 155 (2015) 150–159.

[15] X.F. Yang, J.L. Xu, Z. Miao, J. Zou, C. Yu, Operation of an organic Rankine cycle dependent on pumping flow rates and expander torques, Energy 90 (2015) 864–878.

[16] A. Landelle, N. Tauveron, R. Revellin, P. Haberschill, S. Colasson, V. Roussel, Performance investigation of reciprocating pump running with organic fluid for organic Rankine cycle, Appl. Therm. Eng. 113 (2017) 962–969.

[17] G. Carrato, P. Pallis, A.D. Leontaritis, S. Karellas, P. Vourliotis, S. Rech, A. Lazzaretto, Experimental performance evaluation of a multi-diaphragm pump of a micro-ORC system, Energy Procedia 129 (2017) 1018–1025.

[18] F. D'Amico, P. Pallis, A.D. Leontaritis, S. Karellas, N.M. Kakalisc, S. Rech, A. Lazzaretto, Semi-empirical model of a multi-diaphragm pump in an Organic Rankine Cycle (ORC) experimental unit, Energy 143 (2018) 1056–1071.

[19] W. Li, A. Mckeown, Z. Yu, Correction of cavitation with thermodynamic effect for a diaphragm pump in organic Rankine cycle systems, Energy Rep. 6 (2020) 2956–2972.

[20] N. Casari, E. Fadiga, M. Pinelli and, et al., Pressure pulsation and cavitation phenomena in a micro-ORC system, Energies 12 (2019) 2186.

[21] W. Li, Z. Yu, Cavitating flows of organic fluid with thermodynamic effect in a diaphragm pump for organic Rankine cycle systems, Energy 237 (2021) 121495.

[22] G.H. Schnerr, J. Sauer, Physical and numerical modelling of unsteady cavitation dynamics, in: Proceedings of the 4th International Conference on Multiphase Flow, New Orleans, USA, 2001.

[23] B.B. Mikic, W.M. Rohsenow, P. Griffth, On bubble growth rates, Int. J. Heat Mass Transf. 13 (1970) 657–666.

[24] T.F. Gelder, R.S. Ruggeri and R.D. Moore, "Cavitation similarity considerations based on measured pressure and temperature depressions in cavitated regions of Freon 114," NASA-TN D-3509, Washington DC, USA, 1966.

[25] J. Hord, "Cavitation in liquid cryogens II-Hydrofoil," NASA CR-2156, Washington DC, USA, 1973.

[26] A. Cervone, C. Bramanti, E. Rapposelli, L. d'Agostino, Thermal cavitation experiments on a NACA 0015 hydrofoil, ASME J. Fluids Eng. 128 (2006) 326–331.

[27] AnonymousANSYS CFX-Solver Theory Guide, ANSYS, Inc., Canonsburg, USA, 2011.

[28] K.A. Morch, Cavitation nuclei: experiments and theory, J. Hydrodyn. Ser. B (Engl. Ed.) 21 (2) (2009) 176–189.

[29] R. Sato, K. Kakutani, Measurement of cavitation inception, JSME Int. J. Ser. B 37 (2) (1994) 306–312.

[30] M.T. Khoo, J.A. Venning, B.W. Pearce, K. Takahashi, T. Mori, P. A. Brandner, Natural nuclei population dynamics in cavitation tunnels, Exp. Fluids 61 (2020) 34, doi:10.1007/s00348-019-2843-x.

[31] X. Yao, Z. Li, L. Sun, H. Lu, A study on bubble nuclei population dynamics under reduced pressure, Phys. Fluids 32 (2020) 112019, doi:10.1063/5.0026362.

[32] C.E. Brennen, Cavitation and Bubble Dynamics, Oxford University Press, Oxford, 1995.

[33] N. Zuber, The dynamics of vapor bubbles in nonuniform temperature fields, Int. J. Heat Mass Transf. 2 (1–2) (1961) 83–98.

[34] T.G. Theofanous, P.D. Patel, Universal relations for bubble growth, Int. J. Heat Mass Transf. 19 (4) (1976) 425–429.

[35] H.K. Forster, N. Zuber, Growth of a vapour bubble in a superheated liquid, J. Appl. Phys. 25 (4) (1954) 474–478.

[36] M.S. Plesset, S.A. Zwick, The growth of vapor bubbles in superheated liquids, J. Appl. Phys. 25 (4) (1954) 493–500.

[37] H.K. Forster, N. Zuber, Dynamics of vapor bubbles and boiling heat transfer, AIChE J. 1 (4) (1955) 531–535.

[38] L.E. Scriven, On the dynamics of phase growth, Chem. Eng. Sci. 10 (1–2) (1959) 1–13.

[39] S.A. Mohammadein, S.A. Gouda, Temperature distribution in a mixture surrounding a growing vapour bubble, Heat Mass Transf. 42 (2006) 359–363.

[40] S.J. Board, R.B. Duffey, Spherical vapour bubble growth in superheated liquids, Chem. Eng. Sci. 26 (3) (1971) 263–274.

[41] M.D. Donne, M.P. Ferranti, The growth of vapor bubbles in superheated sodium, Int. J. Heat Mass Transf. 18 (1975) 477–493.

[42] A. Prosperetti, M.S. Plesset, Vapour-bubble growth in a superheated liquid, J. Fluid Mech. 85 (1978) 349–368.

[43] H.S. Lee, H. Merte, Spherical vapor bubble growth in uniformly superheated liquids, Int. J. Heat Mass Transf. 39 (12) (1996) 2427–2447.

[44] A.J. Robinson, R.L. Judd, The dynamics of spherical bubble growth, Int. J. Heat Mass Transf. 47 (2004) 5101–5113.

[45] Q. Wang, J. Gu, Z. Li, W. Yao, Dynamic modeling of bubble growth in vapor-liquid phase change covering a wide range of superheats and pressures, Chem. Eng. Sci. 172 (2017) 169–181.

[46] S. Zanje, K. Iyer, J.S. Murallidharan, H. Punekar, V.K. Gupta, Development of generalized bubble growth model for cavitation and flash boiling, Phys. Fluids 33 (2021) 073311, doi:10.1063/5.0055727.

[47] A.D. Okhotsimskii, The thermal regime of vapour bubble collapse at different Jacob numbers, Int. J. Heat Mass Transf. 31 (8) (1988) 1569–1576.

[48] R. Bardia, M.F. Trujillo, An improved categorization of vapor bubble collapse: explaining the coupled nature of hydrodynamic and thermal mechanisms, Int. J. Heat Mass Transf. 145 (2019) 118754.

[49] Q. Wang, W. Yao, X. Quan, P. Cheng, Validation of a dynamic model for vapor bubble growth and collapse under microgravity conditions, Int. Commun. Heat Mass Transf. 95 (2018) 63–73.

[50] A. Prosperetti, Vapor bubbles, Annu. Rev. Fluid Mech. 49 (2017) 221–248.

[51] M.S. Plesset, S.A. Zwick, A nonsteady heat diffusion problem with spherical symmetry, J. Appl. Phys. 23 (1) (1952) 95–98.

[52] J. Sauer, G. Winkler, G.H. Schnerr, Cavitation and condensation-common aspects of physical modeling and numerical approach, Chem. Eng. Technol. 23 (8) (2000) 663–666.

[53] D. Colombet, E. Goncalvès Da Silva, R. Fortes-Patella, On numerical simulation of cavitating flows under thermal regime, Int. J. Heat Mass Transf. 105 (2017) 411–428.

[54] H. Kim, C. Kim, A physics-based cavitation model ranging from inertial to thermal regimes, Int. J. Heat Mass Transf. 181 (2021) 121991.

[55] A. Hosangadi, V. Ahuja, Numerical study of cavitation cryogenic fluids, ASME J. Fluids Eng. 127 (2) (2005) 267–281.

[56] T. Goel, S. Thakur, R.T. Haftka, W. Shyy, J. Zhao, Surrogate model-based strategy for cryogenic cavitation model validation and sensitivity evaluation, Siddharth Int. J. Numer. Methods Fluids 58 (2008) 969–1007.

[57] C.C. Tseng, W. Shyy, Modeling for isothermal and cryogenic cavitation, Int. J. Heat Mass Transf. 53 (2010) 513–525.

[58] B. Huang, Q. Wu, G.Y. Wang, Numerical investigation of cavitating flow in liquid hydrogen, Int. J. Hydrog. Energy 39 (2014) 1698–1709.

[59] A.K. Singhal, M.M. Athavale, H. Li, Y. Jiang, Mathematical basis and validation of the full cavitation model, ASME J. Fluids Eng. 124 (3) (2002) 617–624.

[60] M. Dular, O. Coutier-Delgosha, Thermodynamic effects during growth and collapse of a single cavitation bubble, J. Fluid Mech. 736 (2013) 44–66.

[61] H. Nazari-Mahroo, K. Pasandideh, H.A. Navid, R. Sadighi-Bonabi, How important is the liquid bulk viscosity effect on the dynamics of a single cavitation bubble? Ultrason. Sonochem. 49 (2018) 47–52.

[62] Y. Liao, D. Lucas, Computational modelling of flash boiling flows: a literature survey, Int. J. Heat Mass Transf. 111 (2017) 240–265.

[63] M. Morgut, E. Nobile, I. Bilus, Comparison of mass transfer models for the numerical prediction of sheet cavitation around a hydrofoil, Int. J. Multiph. Flow 37 (2011) 620–626.

[64] W. Jin, X. Xu, Y. Tang, H. Zhou, H. Zhou, X. Ren, Coefficient adaptation method for the Zwart model, J. Appl. Fluid Mech. 11 (6) (2018) 1665–1678.

[65] H. Zhou, M. Xiang, P.N. Okolo, Z. Wu, G.J. Bennett, W. Zhang, An efficient calibration approach for cavitation model constants based on OpenFOAM platform, J. Mar. Sci. Technol. 24 (2019) 1043–1056.

[66] A. Sikirica, Z. Carija, I. Lucin, L. Grbčić, L. Kranjčević, Cavitation model calibration using machine learning assisted workflow, Mathematics 8 (12) (2020) 2107, doi:10.3390/math8122107.

[67] C. Brennen, A numerical solution of axisymmetric cavity flows, J. Fluid Mech. 37 (4) (1969) 671–688.
[68] H. Lemonnier, A. Rowe, Another approach in modelling cavitating flows, J. Fluid Mech. 195 (1988) 557–580.
[69] C. Pellone, A. Rowe, Effect of separation on partial cavitation, ASME J. Fluid Eng. 110 (2) (1988) 182–189.
[70] M. Deshpande, J. Feng, C.L. Merkle, Cavity flow predictions based on the Euler equations, ASME J. Fluids Eng. 116 (1) (1994) 36–44.
[71] L. Liu, J. Li, Z. Feng, A numerical method for simulation of attached cavitation flows, Int. J. Numer. Methods Fluids 52 (2006) 639–658.
[72] M. Deshpande, J. Feng, C.L. Merkle, Numerical modelling of the thermodynamic effects of cavitation, ASME J. Fluids Eng. 119 (2) (1997) 420–426.
[73] T. Tokumasu, Y. Sekino, K. Kamijo, The numerical analysis of the effect of flow properties on the thermodynamic effect of cavitation, Trans. Jpn. Soc. Aeronaut. Space Sci. 156 (47) (2004) 146–152.
[74] P. Cooper, Analysis of single- and two-phase flows in turbopump inducers, ASME J. Eng. Power 89 (4) (1967) 577–586.
[75] Y. Ventikos, G. Tzabiras, A numerical method for the simulation of steady and unsteady cavitating flows, Comput. Fluids 29 (2000) 63–88.
[76] G.H. Schnerr, I.H. Sezal, S.J. Schmidt, Numerical investigation of three-dimensional cloud cavitation with special emphasis on collapse induced shock dynamics, Phys. Fluids 20 (2008) 040703.
[77] Y. Chen, S.D. Heister, Two-phase modelling of cavitating flows, Comput. Fluids 24 (7) (1995) 799–809.
[78] K. Okita, T. Kajishima, Numerical simulation of unsteady cavitating flows around a hydrofoil, Trans. JSME Ser. B 68 (667) (2002) 637–644.
[79] Y. Delannoy, J.L. Kueny, Two phase flow approach in unsteady cavitation modelling, Cavitation and Multiphase Flow Forum, 1990 New York: ASME.
[80] O. Coutier-Delgosha, J.L. Reboud, Y. Delannoy, Numerical simulation of the unsteady behaviour of cavitating flows, Int. J. Numer. Methods Fluids 42 (2003) 527–554.
[81] J.L. Reboud, O. Coutier-Delgosha, B. Pouffary, R. Fortes- Patella, Numerical simulation of unsteady cavitating flows: some applications and open problems, in: Proceedings of the 5th International Symposium on Cavitation(CAV2003), Osaka, Japan, 2003.
[82] E. Goncalves, R.F. Patella, Numerical simulation of cavitating flows with homogeneous models, Comput. Fluids 38 (2009) 1682–1696.
[83] E. Goncalves, R.F. Patella, J. Rolland, B. Pouffary, G. Challier, Thermodynamic effect on a cavitating inducer in liquid hydrogen, ASME J. Fluids Eng. 132 (11) (2010) 111305.
[84] J. Decaix, E. Goncalves, Investigation of three-dimensional effects on a cavitating Venturi flow, Int. J. Heat Fluid Flow 44 (2013) 576–595.
[85] E. Goncalves, Numerical study of expansion tube problems: toward the simulation of cavitation, Comput. Fluids 72 (2013) 1–19.
[86] E. Goncalves, B. Charriere, Modelling for isothermal cavitation with a four-equation model, Int. J. Multiph. Flow 59 (2014) 54–72.
[87] E. Goncalves, R.F. Patella, Constraints on equation of state for cavitating flows with thermodynamic effects, Appl. Math. Comput. 217 (2011) 5095–5102.
[88] E. Goncalves, Modeling for non isothermal cavitation using 4-equation models, Int. J. Heat Mass Transf. 76 (2014) 247–262.
[89] E. Goncalves, D. Zeidan, Numerical study of turbulent cavitating flows in thermal regime, Int. J. Numer. Methods Heat Fluid Flow 27 (7) (2017) 1487–1508.
[90] E. Goncalves, R.F. Patella, Numerical study of cavitating flows with thermodynamic effect, Comput. Fluids 39 (2010) 99–113.
[91] B. Charriere, J. Decaix, E. Goncalves, A comparative study of cavitation models in a Venturi flow, Eur. J. Mech. B Fluids 49 (2015) 287–297.
[92] C. Vortmann, G.H. Schnerr, S. Seeleck, Thermodynamic modelling and simulation of cavitating nozzle flow, Int. J. Heat Fluid Flow 24 (2003) 774–783.
[93] C.L. Merkle, J. Feng, P.E. Buelow, Computational modeling of the dynamics of sheet cavitation, in: Proceedings of the 3rd International Symposium on Cavitation, Grenoble, France, 1998.
[94] R.F. Kunz, D.A. Boger, D.R. Stinebring, T.S. Chyczewski, J.W. Lindau, H.J. Gibeling, S. Venkateswaran, T.R. Govindan, A preconditioned Navier-Stokes method for two-phase flows with application to cavitation prediction, Comput. Fluids 29 (8) (2000) 849–875.
[95] I. Senocak, W. Shyy, Interfacial dynamics-based modelling of turbulent cavitating flows, Part I: model development and steady-state computations, Int. J. Numer. Methods Fluids 44 (9) (2004) 976–995.
[96] T. Usui, Y. Iga, Prediction method of cavitation inside torque converter using gaseous cavitation model, Trans. Soc. Automot. Eng. Jpn. 52 (5) (2021) 961–965.
[97] A. Hosangadi, V. Ahuja, R. Ungewitter, Analysis of thermal effects in cavitating liquid hydrogen inducers, J. Propuls. Power 23 (6) (2007) 1225–1234.
[98] S. Shi, G. Wang, Numerical calculation of thermal effect on cavitation in cryogenic fluids, Chin. J. Mech. Eng. 25 (6) (2012) 1176–1183.
[99] T. Chen, B. Huang, G. Wang, K. Wang, Effects of fluid thermophysical properties on cavitating flows, J. Mech. Sci. Technol. 29 (10) (2015) 4239–4246.
[100] T. Chen, G. Wang, B. Huang, K. Wang, Numerical study of thermodynamic effects on liquid nitrogen cavitating flows, Cryogenics 70 (2015) 21–27.
[101] T.Z. Sun, Y.J. Wei, C. Wang, Computational analyses of cavitating flows in cryogenic liquid hydrogen, J. Harbin Inst. Technol. 23 (5) (2016) 1–7 (New Series).
[102] Y. Saito, R. Takami, I. Nakamori, T. Ikohagi, Numerical analysis of unsteady behavior of cloud cavitation around a NACA0015 foil, Comput. Mech. 40 (2007) 85–96.
[103] N. Ochiai, Y. Iga, M. Nohmi, T. Ikohagi, Numerical prediction of cavitation erosion intensity in cavitating flows around a Clark Y 11.7% hydrofoil, J. Fluid Sci. Technol. 5 (3) (2010) 416–431.
[104] A. Gnanaskandan, K. Mahesh, A numerical method to simulate turbulent cavitating flows, Int. J. Multiph. Flow 70 (2015) 23–34.
[105] A.D. Le, J. Okajima, Y. Iga, Numerical simulation study of cavitation in liquefied hydrogen, Cryogenics 101 (2019) 29–35.
[106] S. Yang, C. Habchi, Real-fluid phase transition in cavitation modeling considering dissolved non-condensable gas, Phys. Fluids 32 (2020) 032102.
[107] S. Liu, S. Li, L. Zhang, Y. Wu, A mixture model with modified mass transfer expression for cavitating turbulent flow simulation, Eng. Comput. 25 (4) (2008) 290–304.
[108] T. Chen, B. Huang, G. Wang, X. Zhao, Numerical study of cavitating flows in a wide range of water temperatures with special emphasis on two typical cavitation dynamics, Int. J. Heat Mass Transf. 101 (2016) 886–900.
[109] A. Yu, Q. Tang, D. Zhou, J. Liu, Entropy production analysis in two-phase cavitation flows with thermodynamic cavitation model, Appl. Therm. Eng. 171 (2020) 115099.
[110] A. Yu, Q. Tang, D. Zhou, Entropy production analysis in thermodynamic cavitating flow with the consideration of local compressibility, Int. J. Heat Mass Transf. 153 (2020) 119604.
[111] W. Yuan, J. Sauer, G.H. Schnerr, Modeling and computation of unsteady cavitation flows in injection nozzles, Mech. Ind. 2 (5) (2001) 383–394.
[112] H. Kanfoud, H. Lamloumi, R. Zgolli, A new model to simulate a cavitating flow, in: Proceedings of the International Renewable Energy Congress, Sousse, Tunisia, 2010.
[113] F. Hong, J. Yuan, B. Zhou, Application of a new cavitation model for computations of unsteady turbulent cavitating flows around a hydrofoil, J. Mech. Sci. Technol. 31 (1) (2017) 249–260.
[114] F. Hong, W. Yu, F. Zhang, Numerical investigation of turbulent cavitating flow in an axial flow pump using a new transport-based model, J. Mech. Sci. Technol. 34 (2) (2020) 745–756.
[115] J. Zhu, Y. Chen, D. Zhao, X. Zhang, Extension of the Schnerr-Sauer model for cryogenic cavitation, Eur. J. Mech. B Fluids 52 (2015) 1–10.
[116] J. Zhu, D. Zhao, L. Xu, X. Zhang, Interactions of vortices, thermal effects and cavitation in liquid hydrogen cavitating flows, Int. J. Hydrog. Energy 41 (2016) 614–631.
[117] X. Long, Q. Liu, B. Ji, Y. Lu, Numerical investigation of two typical cavitation shedding dynamics flow in liquid hydrogen with thermodynamic effects, Int. J. Heat Mass Transf. 109 (2017) 879–893.
[118] M.G. De Giorgi, A. Ficarella, D. Fontanarosa, Implementation and validation of an extended Schnerr-Sauer cavitation model for non-isothermal flows in OpenFOAM, Energy Procedia 126 (201709) (2017) 58–65.
[119] J. Zhu, S. Wang, L. Qiu, X. Zhi, X. Zhang, Frequency characteristics of liquid hydrogen cavitating flow over a NACA0015 hydrofoil, Cryogenics 90 (2018) 7–19.
[120] Y. Liu, X. Li, W. Wang, L. Li, Y. Huo, Numerical investigation on the evolution of forces and energy features in thermo-sensitive cavitating flow, Eur. J. Mech. B Fluids 84 (2020) 233–249.
[121] M.P. Kinzel, J.W. Lindau, R.F. Kinz, An assessment of computational fluid dynamics cavitation models using bubble growth theory and bubble transport modelling, ASME J. Fluids Eng. 141 (4) (2019) 041301.
[122] M.G. De Giorgi, D. Bello, A. Ficarella, Analysis of thermal effects in a cavitating orifice using Rayleigh equation and experiments, ASME J. Eng. Gas Turbines Power 132 (9) (2010) 092901.
[123] S. Tsuda, N. Tani, N. Yamanishi, Development and validation of a reduced critical radius model for cryogenic cavitation, ASME J. Fluids Eng. 134 (5) (2012) 051301.
[124] X.B. Zhang, Z. Wu, S.J. Xiang, L.M. Qiu, Modeling cavitating flow of cryogenic fluids with thermodynamic phase-change theory, Chin. Sci. Bull. 58 (4–5) (2013) 567–574.
[125] W.G. Zhao, L.X. Zhang, X.M. Shao, Numerical simulation of cavitation flow under high pressure and temperature, J. Hydrodyn. Ser. B (Engl. Ed.) 23 (3) (2011) 289–294.
[126] X.B. Zhang, L.M. Qiu, H. Qi, X.J. Zhang, Z.H. Gan, Modeling liquid hydrogen cavitating flow with the full cavitation model, Int. J. Hydrog. Energy 33 (2008) 7197–7206.
[127] M.G. De Giorgi, A. Ficarella, F. Chiara, D. Laforgia, Experimental and numerical investigations of cavitating flows, in: Proceedings of the 35th AIAA Fluid Dynamics Conference and Exhibit, Toronto, Canada, 2005.
[128] P.J. Zwart, A.G. Gerber, T. Belamri, A two-phase flow model for predicting cavitation dynamics, in: Proceedings of the 5th International Conference on Multiphase Flow, Yokohama, Japan, 2004.
[129] Y. Zhang, X.W. Luo, B. Ji, S.H. Liu, Y.L. Wu, H.Y. Xu, A thermodynamic cavitation model for cavitating flow simulation in a wide range of water temperature, Chin. Phys. Lett. 27 (1) (2010) 016401.
[130] X.L. Tang, L.Y. Bian, F.J. Wang, X.Q. Li, M. Hao, Numerical investigation on cavitating flows with thermodynamic effects in a diffuser-type centrifugal pump, J. Mech. Sci. Technol. 27 (6) (2013) 1655–1664.
[131] T.Z. Sun, X.F. Ma, Y.J. Wei, C. Wang, Computational modeling of cavitating flows in liquid nitrogen by an extended transport-based cavitation model, Sci. China Technol. Sci. 59 (2) (2015) 337–346.
[132] Y. Liu, X. Li, Z. Lin, L. Li, Z. Zhu, Numerical analysis of thermo-sensitive cavitating flows with special emphasises on flow separation and enstrophy conversion, Int. Commun. Heat Mass Transf. 125 (2021) 105336.

[133] S. Zhang, X. Li, Z. Zhu, Numerical simulation of cryogenic cavitating flow by an extended transport-based cavitation model with thermal effect, Cryogenics 92 (2018) 98–104.
[134] W. Li, Y. Yang, W. Shi, X. Zhao, W. Li, The correction and evaluation of cavitation model considering the thermodynamic effect, Math. Probl. Eng. 2018 (2018) VolsVolume, doi:10.1155/2018/7217513.
[135] C. Shao, Z. Zhang, J. Zhou, Study of the flow in a cryogenic pump under different cavitation inducements by considering the thermodynamic effect, Int. J. Numer. Methods Heat Fluid Flow 30 (9) (2020) 4307–4329.
[136] R. Xue, Y. Ruan, X. Liu, F. Cao, Y. Hou, The influence of cavitation on the flow characteristics of liquid nitrogen through spray nozzle: a CFD study, Cryogenics 86 (2017) 42–56.
[137] C. Wang, Y. Zhang, H. Hou, J. Zhnag, C. Xu, Entropy production diagnostic analysis of energy consumption for cavitation flow in a two-stage LNG cryogenic submerged pump, Int. J. Heat Mass Transf. 129 (2019) 342–356.
[138] P. Song, J. Sun, Cryogenic cavitation mitigation in a liquid turbine expander of an air-separation unit through collaborative fine-tuned optimization of impeller and fairing cone geometries, Energies 13 (1) (2020) 50, doi:10.3390/en13010050.
[139] B. Xu, J. Feng, F. Wan, D. Zhang, X. Shen, W. Zhang, Numerical investigation of modified cavitation model with thermodynamic effect in water and liquid nitrogen, Cryogenics 106 (2020) 103049.
[140] X. Li, T. Shen, P. Li, X. Guo, Z. Zhu, Extended compressible thermal cavitation model for the numerical simulation of cryogenic cavitating flow, Int. J. Hydrog. Energy 45 (2020) 10104–10118.
[141] T. Sun, Y. Wei, L. Zou, Y. Jiang, C. Xu, Z. Zong, Numerical investigation on the unsteady cavitation shedding dynamics over a hydrofoil in thermo-sensitive fluid, Int. J. Multiph. Flow 111 (2019) 82–100.
[142] Y. Yamamoto, S. Watanabe, S.I. Tsuda, A simple cavitation model for unsteady simulation and its application to cavitating flow in two-dimensional convergent divergent nozzle, in: Proceedings of the International Symposium of Cavitation and Multiphase Flow (ISCM2014), Beijing, China, 2014.
[143] B. Huang, G.Y. Wang, A modified density based cavitation model for time dependent turbulent cavitating flow computations, Chin. Sci. Bull. 56 (19) (2011) 1985–1992.
[144] G. Peng, K. Okada, C. Yang, Y. Oguma, S. Shimizu, Numerical simulation of unsteady cavitation in a high-speed water jet, Int. J. Fluid Mach. Syst. 9 (1) (2016) 66–74.
[145] M.P. Kinzel, J.W. Lindau, R.F. Kunz, A unified homogenous multiphase CFD model for cavitation, in: Proceedings of the ASME Fluids Engineering Division Summer Meeting, Waikoloa, Hawaii, USA, 2017.
[146] A. Yu, X.W. Luo, B. Ji, R.F. Huang, V. Hidalgo, H.K. Song, Cavitation simulation with consideration of the viscous effect at large liquid temperature variation, Chin. Phys. Lett. 31 (8) (2014) 086401.
[147] S.Y. Konstantinov, D.V. Tselischev, V.A. Tselischev, Numerical cavitation model for simulation of mass flow stabilization effect in ANSYS CFX, Mod. Appl. Sci. 9 (4) (2015) 21–31.
[148] K. Pang, Y. Li, W. Yang, A calculation model considering thermodynamic and viscosity effects, Eng. Comput. 35 (11) (2018) 2308–2326.
[149] Y. Zhao, G. Wang, B. Huang, A cavitation model for computations of unsteady cavitating flows, Acta Mech. Sin. 32 (2) (2016) 273–283.
[150] Y. Ye, G. Li, Modeling of hydrodynamic cavitating flows considering the bubble-bubble interaction, Int. J. Multiph. Flows 84 (2016) 155–164.
[151] Y. Ye, X. Zhu, F. Lai, G. Li, Application of the semi-analysis cavitation model to flows in a centrifugal pump, Int. Commun. Heat Mass Transf. 86 (2017) 92–100.
[152] T. Du, Y. Wang, L. Liao, C. Huang, A numerical model for the evolution of internal structure of cavitation cloud, Phys. Fluids 28 (2016) 077103.
[153] T. Du, Y. Wang, C. Huang, L. Liao, A numerical model for cloud cavitation based on bubble cluster, Theor. Appl. Mech. Lett. 7 (2017) 231–234.
[154] D.D. Jospeh, Cavitation in a flowing liquid, Phys. Rev. E 51 (3) (1995) R1649–R1650.
[155] A. Asnaghi, A. Feymark, R.E. Bensow, Improvement of cavitation mass transfer modelling based on local flow properties, Int. J. Multiph. Flow 93 (2017) 142–157.
[156] F. Hong, Z. Gao, L. Liu, J. Yuan, Numerical investigation of the turbulent cavitating flow over submerged bodies, Int. J. Fluid Mach. Syst. 11 (1) (2018) 85–96.
[157] J. Li, P.M. Carrica, A population balance cavitation model, Int. J. Multiph. Flow 138 (2021) 103617.
[158] S. Kumar, C.E. Brennen, Some nonlinear interactive effects in bubbly clouds, J. Fluid Mech. 253 (1993) 565–591.
[159] Y.C. Wang, Effects of nuclei size distribution on the dynamics of a spherical clod of cavitation bubbles, ASME J. Fluids Eng. 121 (4) (1999) 881–886.
[160] Z. Liu, C.E. Brennen, Cavitation nuclei Population and event rates, ASME J. Fluids Eng. 120 (4) (1998) 728–737.
[161] F. Takemura, Y. Matsumoto, Influence of internal phenomena on gas bubble motion, JSME Int. J. Ser. B 37 (4) (1994) 736–745.
[162] Y. Ito, H. Wakamatsu, T. Nagasaki, Numerical simulation of sub-cooled cavitating flow by using bubble size distribution, J. Therm. Sci. 12 (4) (2003) 350–356.
[163] Y. Ito, Numerical model and validation for cryogenic high-speed cavitating flow based on bubble size distribution model in consideration of rigorous heat transfer around bubble oscillation, J. Jpn. Soc. Aeronaut. Space Sci. 56 (657) (2008) 456–463.
[164] Y. Ito, X. Zheng, T. Nagasaki, One-way coupling numerical simulation of cryogenic cavitation around an inducer, Int. J. Fluid Mach. Syst. 12 (3) (2019) 235–243.
[165] C.F. Delale, K. Okita, Y. Matsumoto, Steady-state cavitating nozzle flows with nucleation, ASME J. Fluids Eng. 127 (4) (2005) 770–777.
[166] D. Li, S. Liu, Y. Wei, T. Ren, Y. Tang, A turbulent two-phase model for predicting cavitating flow based on homogenous nucleation theory, Int. Commun. Heat Mass Transf. 97 (2018) 17–29.
[167] M.G. De Giorgi, D. Fontanarosa, A. Ficarella, Characterization of unsteady cavitating flow regimes around a hydrofoil, based on an extended Schnerr–Sauer model coupled with a nucleation model, Int. J. Multiph. Flow 115 (2019) 158–180.
[168] M.G. De Giorgi, A. Ficarella, D. Fontanarosa, Numerical Investigation of non-isothermal cavitating flows on hydrofoils by means of an extended Schnerr-Sauer model coupled with a nucleation model, ASME J. Eng. Gas Turbines Power 142 (4) (2020) 041003.
[169] Y. Kodama, N. Take, S. Tamiya, H. Kato, The effect of nuclei on the inception of bubble and sheet cavitation on axisymmetric bodies, ASME J. Fluids Eng. 103 (4) (1981) 557–563.
[170] R.S. Meyer, M.L. Billet, J.W. Holl, Freestream nuclei and traveling bubble-cavitation, ASME J. Fluids Eng. 114 (4) (1992) 672–679.
[171] C.T. Hsiao, G.L. Chahine, H.L. Liu, Scaling effect on prediction of cavitation inception in a line vortex flow, ASME J. Fluids Eng. 125 (1) (2003) 53–60.
[172] G.F. Oweis, I.E. van der Hout, C. Iyer, G. Tryggvason, S.L. Ceccioa, Capture and inception of bubbles near line vortices, Phys. Fluids 17 (2005) 022105.
[173] C.T. Hsiao, L.L. Pauley, Study of tip vortex cavitation inception using Navier-Stokes computation and bubble dynamics model, ASME J. Fluids Eng. 121 (1) (1999) 198–204.
[174] K.J. Farrell, Eulerian/Lagrangian analysis for the prediction of cavitation inception, ASME J. Fluids Eng. 125 (1) (2003) 46–52.
[175] C.T. Hsiao, G.L. Chahine, Prediction of tip vortex cavitation inception using coupled spherical and nonspherical bubble models and Navier–Stokes computations, J. Mar. Sci. Technol. 8 (2004) 99–108.
[176] C.T. Hsiao, G.L. Chahine, Scaling of tip vortex cavitation inception noise with a bubble dynamics model accounting for nuclei size distribution, ASME J. Fluids Eng. 127 (1) (2005) 55–65.
[177] K. Okuda, T. Ikohagi, Numerical simulation of collapsing behavior od bubble clouds, JSME Trans. Ser. B 62 (603) (1996) 38–43.
[178] Y. Matsumoto, S. Yoshizawa, Behaviour of a bubble cluster in an ultrasound field, Int. J. Numer. Methods Fluids 47 (2005) 591–601.
[179] N. Ochiai, J. Ishimoto, Numerical investigation of multi-bubble behavior and induced pressure in a megasonic field, J. Fluid Mech. 818 (2017) 562–594.
[180] N. Ochiai, J. Ishimoto, Numerical analysis of the effect of bubble distribution on multiple-bubble behavior, Ultrason. Sonochem. 61 (2020) 104818.
[181] E. Johnsen, T. Colonius, Shock-induced collapse of a gas bubble in shockwave lithotripsy, J. Acoust. Soc. Am. 124 (4) (2008) 2011–2020.
[182] E. Johnsen, T. Colonius, Numerical simulations of non-spherical bubble collapse, J. Fluid Mech. 629 (2009) 231–262.
[183] N. Ochiai, Y. Iga, M. Nohmi, T. Ikohagi, Study of quantitative numerical prediction of cavitation erosion in cavitating flow, ASME J. Fluids Eng. 135 (1) (2013) 011303.
[184] D. Fuster, A review of models for bubble clusters in cavitating flow, Flow Turbul. Combust. 102 (2019) 497–536.
[185] M. Khojasteh-Manesh, M. Mahdi, Evaluation of cavitation erosion intensity in a microscale nozzle using Eulerian–Lagrangian bubble dynamic simulation, ASME J. Fluids Eng. 141 (6) (2019) 061303.
[186] L. Li, Z. Wang, X. Li, Z. Zhu, Multiscale modeling of tip-leakage cavitating flows by a combined volume of fluid and discrete bubble model, Phys. Fluids 33 (2021) 062104.
[187] A. Kubota, H. Kato, H. Yamaguchi, A new modelling of cavitating flows: a numerical study of unsteady cavitation on a hydrofoil section, J. Fluid Mech. 240 (1992) 59–96.
[188] J. Ishimoto, K. Kamijo, Numerical simulation of cavitating flow of liquid helium in Venturi channel, Cryogenics 43 (2003) 9–17.
[189] E. Giannadakis, M. Gavaises, C. Arcoumanis, Modelling of cavitation in diesel injector nozzles, J. Fluid Mech. 616 (2008) 153–193.
[190] M. Abdel-Maksoud, D. Hanel, U. Lantermann, Modeling and computation of cavitation in vortical flow, Int. J. Heat Fluid Flow 31 (2010) 1065–1074.
[191] J. Ma, C.T. Hsiao, G.L. Chahine, Euler-Lagrange simulations of bubble cloud dynamics near a wall, ASME J. Fluids Eng. 137 (4) (2015) 041301.
[192] C.T. Hsiao, J. Ma, G.L. Chahine, Multiscale two-phase flow modelling of sheet and cloud cavitation, Int. J. Multiph. Flow 90 (2017) 102–117.
[193] G. Hammerl, W.A. Wall, A four-way coupled Euler–Lagrange approach using a ariational multiscale method for simulating cavitation, in: Proceedings of the 9th International Symposium on Cavitation (CAV2015), Lausanne, Switzerland, 2015.
[194] J. Ma, C.T. Hsiao, G.L. Chahine, A physics based multiscale modelling of cavitating flows, Comput. Fluids 145 (2017) 68–84.
[195] A. Peters, O. El Moctar, Numerical assessment of cavitation-induced erosion using multi-scale Euler-Lagrange method, J. Fluids Mech. 894 (2020) A19.
[196] E. Ghahramani, H. Ström, R.E. Bensow, Numerical simulation and analysis of multi-scale cavitating flows, J. Fluid Mech. 922 (2021) A22.
[197] Z. Wang, H. Cheng, B. Ji, Euler–Lagrange study of cavitating turbulent flow around a hydrofoil, Phys. Fluids 33 (2021) 112108.

[198] H. Cheng, X. Long, B. Ji, X. Pengc, M. Farhat, A new Euler-Lagrangian cavitation model for tip-vortex cavitation with the effect of non-condensable gas, Int. J. Multiph. Flow 134 (2021) 103441.
[199] L. Wilczynski, Stochastic modeling of cavitation phenonomena in turbulent flow, in: Advances in Fluid Mechanics III, WIT Press, Southampton, UK, 2000, pp. 503–512.
[200] J. Dumond, F. Magagnato, A. Class, Stochastic-field cavitation model, Phys. Fluids 25 (2013) 073302.
[201] W. Li, Z. Yu, Cavitation models with thermodynamic effect for organic fluid cavitating flows in organic Rankine cycle systems: a review, Therm. Sci. Eng. Prog. 26 (2021) 101079.
[202] J. Franc, C. Pellone, Analysis of thermal effects in a cavitating inducer using Rayleigh equation, ASME J. Fluids Eng. 129 (8) (2007) 974–983.
[203] M.G. Rodio, M.G. De Giorgi, A. Ficarella, Influence of convective heat transfer modeling on the estimation of thermal effects in cryogenic cavitating flows, Int. J. Heat Mass Transf. 55 (2012) 6538–6554.